Pacific Gas and Electric Company

Lawrence F. Womack
Vice President
Nuclear Services

Diablo Canyon Power Plant
P.O. Box 56
Avila Beach, CA 93424

805.545.4600
Fax: 805.545.4234

May 23, 2002

PG&E Letter DIL-02-006

U.S. Nuclear Regulatory Commission
ATTN: Document Control Desk
Washington, DC 20555-0001

Docket No. 72-26
Diablo Canyon Independent Spent Fuel Storage Installation
Submittal of Diablo Canyon Independent Spent Fuel Storage Installation Safety Analysis Report Reference Documents

Dear Commissioners and Staff:

On December 21, 2001, Pacific Gas and Electric Company (PG&E) submitted an application to the Nuclear Regulatory Commission, in PG&E Letter DIL-01-002, requesting a site-specific license for an Independent Spent Fuel Storage Installation (ISFSI) at the Diablo Canyon Power Plant. The application included a Safety Analysis Report (SAR), Environmental Report, and other required documents in accordance with 10 CFR 72.

As requested by Mr. S. Baggett, four documents referenced in the Diablo Canyon ISFSI SAR are enclosed for use by the NRC staff in their review of the application.

If you have any questions regarding this matter, please contact Mr. Terence Grebel at (805) 595-6382.

Sincerely,

Lawrence F. Womack
Enclosure

GWH2
cc: Diablo Distribution
Ellis W. Merschoff
David L. Proulx
Girija S. Shukla
cc/enc: James R. Hall
David A. Repka
John Stamatakos

NMSS01 Public

LIST OF ATTACHED DIABLO CANYON ISFSI SAR REFERENCE DOCUMENTS

1. Harding, Miller, Lawson & Associates, Soil Investigation Landslide, Diablo Canyon Site, San Luis Obispo County, California, July 29, 1970.

2. Rocscience, Inc., SWEDGE Probabilistic Analysis of the Geometry and Stability of Surface Wedges, Version 3.06, 1999 (Users Guide).

3. S. A. Ashford and N. Sitar, Seismic Response of Steep Natural Slopes, Report No. UCB/EERC-94/05, College of Engineering, University of California, Berkeley, May 1994.

4. Design of Structures for Missile Impact, BC-TOP-9A, Bechtel Power Corporation Topical Report, Revision 2, September 1974.

SOIL INVESTIGATION
LANDSLIDE, DIABLO CANYON SITE
SAN LUIS OBISPO COUNTY, CALIFORNIA

Project Number 569,010.04

Prepared for

Pacific Gas & Electric Company
245 Market Street
San Francisco, California

by

Stephen R. Korbay,
Geologist - 853

Henry T. Taylor,
Civil Engineer - 8787

Harding, Miller, Lawson & Associates
155 Montgomery Street
San Francisco, California 94104

July 29, 1970

TABLE OF CONTENTS

LIST OF ILLUSTRATIONS

I INTRODUCTION

This report presents the results of our soil investigation of the recent landslide in the coastal bluff at the Diablo Canyon site, San Luis Obispo County, California.

We understand that the landslide occurred during the early part of this year in the cove located adjacent to the Pacific Ocean and west of the existing plant access road near the warehouse and batch plant. We also understand that this area is not presently part of the nuclear plant construction; however, it may be the location for future cooling water discharge conduits.

The purpose of our work was to investigate the probable cause, extent, and condition of the recent slide in order to provide you with conclusions and recommendations for stabilization of the landslide area.

II FIELD EXPLORATION AND LABORATORY TESTS

We performed a field investigation of the landslide and surrounding area by conducting a geologic reconnaissance and by drilling four test borings. The general site conditions and boring locations are shown on the accompanying Site Plan, Plate 1, Section IX. The borings were drilled with a 24-inch diameter bucket auger drill rig to depths ranging from 13 to 46 feet. Each boring was logged by our geologist who also obtained representative samples of the soil and rock penetrated. These samples were tested in our laboratory to determine moisture content, dry density, and shear strength. The results of these tests are shown on the boring logs, Plates 6 through 9 in the Appendix.

III SITE CONDITIONS

The landslide is approximately 200 feet wide and occupies the full height of the bluff face above a cove that is contiguous to the Ocean. The existing slope in places is as steep as 1-1/3 horizontal to 1 vertical. The top of slope is approximately 105 feet above Sea Level. The top of the slide is approximately 15 feet laterally from the toe of the existing fill for the plant access road.

The slide surface contains numerous tension cracks and scarps especially along the upper limits. Some of the slide debris has moved to the base of the slope along the beach where wave action continuously removes loose material. A 15-foot deep and 25-foot wide erosion gully is present in the center of the slide. The gully is a result of outlet flow from an existing 4-1/2 foot diameter culvert pipe located at the top of slope. The culvert inlet is located across the plant access road near the warehouse. The flow has since been diverted around the slide area and is presently contained in a temporary drainage ditch leading to the cliff edge to the south.

Numerous shallow mud flows are present on the slope outside the present slide limits. Evidence of soil creep, the gradual movement of soil on slopes due to shrinkage and expansion resulting from moisture changes, is also present on the slope. Seepage and springs exist in the area, especially along the toe of slope. Existing erosion gullies expose the deeply weathered bedrock.

IV SOIL AND ROCK CONDITIONS

According to boring data and surface exposures, the landslide and adjacent slope is underlain by soils consisting of silt, clay, and sand; the soils overlie volcanic bedrock. The rock consists of altered tuff, generally sheared and deeply weathered, with occasional tuffaceous siltstone and shale interbeds.

The east and west cliff faces of the cove contain hard vitric tuff and shale bedrock, producing steep rock slopes which are relatively resistant to erosion.

Seepage was observed in Borings 1 and 2; however, only two feet of water accumulated in Boring 1 after two days. Both Borings 1 and 2 have been converted to observation wells by installing 12-inch diameter PMP casing and backfilling the sides with drain rock. Since borings were not drilled within the slide mass due to inaccessibility, the location of the slip plane can only be inferred. Surface conditions indicate slide debris extending to the beach at the base of the slope, suggesting the presence of a rotational-type slide. Subsurface conditions are illustrated on the accompanying Cross Sections, Plate 2.

V GEOLOGY

The bedrock in the slide area is assigned to the Obispo tuff member of the Monterey Formation of Miocene Age. The Obispo tuff stratigraphically underlies the sedimentary rocks of the Monterey formation found to the north. The contact between these two units is located north of the slide.

The altered tuff underlying the north slope of the cove and beach is apparently in fault or intrusive contact with the stronger vitric tuff forming the adjacent steep cliffs. The altered tuff is highly sheared adjacent to the vitric tuff, indicating intense fracturing due to past movement along the contact. Evidence of slickensides, fault gouge, and breccia is present along the contact at the base of the west cliff face.

The sand and gravel overlying the bedrock represents marine terrace deposits on an ancient wave cut bench formed during the Pleistocene. The thickness of overburden at this location suggests the presence of an ancient ravine area, probably extending farther upslope. The ravine probably formed as a result of the deep erosion of the relatively weak tuff. The ancient ravine area later became filled and covered with younger alluvium and is presently not distinguishable on the surface. The upper portions of the soil overburden are part of the large alluvial fan forming most of the gentle slopes in the area to the north.

VI DISCUSSION

The landslide above the cove represents an accelerated form of the natural process of bluff regression; it occurred at this location for the following reasons:

1. The thick alluvial soil is unstable on the steep existing slope, especially when it overlies weak material such as the tuff rock-type present.

2. The terrace deposit of sand and gravel overlying the bedrock probably carries water acquired from surface infiltration of the upper alluvial fan, especially during heavy rainfall.

3. Erosion and removal of the slope toe by wave action continuously produces the existing steep slope, preventing natural stabilization by normal slope flattening due to continued slide activity.

4. The concentrated flow of water from the existing culvert hastened the sliding process.

VII CONCLUSIONS

On the basis of our investigation, we conclude that the landslide can be stabilized. Corrective measures should be taken since it is probable that the slide area will enlarge with time unless the stability is improved. The completeness of the corrective measures (and therefore the cost) can vary through wide limits depending upon the importance of minimizing future movements. We do not believe the slide represents a threat to the safety of persons or existing or proposed structures. The access road could become undermined with time but it appears relatively simple to relocate it farther uphill should this occur.

Three alternate schemes of correction are presented in subsequent parts of this report. Scheme 1 is the minimum we believe should be done if the enlargement of the slide area is to be retarded. Future movement could occur but the chance of it happening and the magnitude if it happens should be greatly reduced. Scheme 3 should prevent future sliding. While no slide correction is foolproof, experience has been excellent with slide areas retained by the extensive method shown. Scheme 2 is an intermediate method in terms of cost and expected performance.

VIII RECOMMENDATIONS

A. Scheme No. 1

Objective: To perform a limited amount of slope reconstruction and drainage installation necessary to reduce but not completely eliminate continued slide movement.

Corrective measures should include

1. Resurface the existing slope of the landslide and surrounding area by removing steep scarps, loose surface material, and filling erosion gullies and tension cracks with compacted soil.

2. Remove excess water in the existing observation wells by pumping during periods of rainfall or when required.

3. In lieu of No. 2, provide gravity drainage of the wells by installing perforated tar-coated pipe in hydrauger borings drilled from the base of the slope up to the bottom of each well.

4. Provide slope protection at the landslide toe in the form of a 30-foot wide and 15-foot high berm of riprap to reduce continued erosion by wave action. Riprap should consist of 1/2-ton class material placed by clam-type equipment.

5. Concrete line the existing drainage ditch located along the south top of slope to prevent any further infiltration of surface water from the culvert.

Illustration of the above scheme is presented on Plate 3 in Section IX.

B. Scheme No. 2

Objective: Stabilization of the landslide by buttressing and surfacing the slope with riprap.

Corrective measures should include

1. If sufficient riprap is available, provide a slope buttress and surface cover as shown on Plate 4, Section IX. Approximately 16,000 to 18,000 cubic yards of light class material will be required and should be placed by Method B as specified in the State of California Standard Specifications. The buttress portion (behind the 1:1 slope) should consist of 1/2-ton class material placed by clam-type equipment.

2. Prior to the placement of riprap, dress and smooth the existing slope by grading loose slide debris and soil.

3. The drainage ditch located on the top of slope should be concrete-lined as previously recommended under Scheme No. 1.

C. Scheme No. 3

Objective: To perform the most thorough slope reconstruction necessary for stabilization of the landslide area.

Corrective measures should include

1. Excavate the unstable slide debris (approximately 30,000 cubic yards) and stockpile in an area south of the existing leach field to allow for drying.

2. Excavate keyways into firm soil or bedrock below the slide plane, as shown on Plate 5, Section IX.

3. Install subdrainage in the base of the excavation and along keyways where required. Approximately 600 feet of six-inch diameter perforated metal pipe will be required with 180 feet of six-inch diameter CMP. Approximately 500 cubic yards of crushed drain rock also will be required. Provide subdrain cleanout risers.

4. Reconstruct the slope with compacted fill using the stockpiled material after moisture conditioning as required. Compact the fill to at least 90 percent of the maximum dry density determined by the ASTM D1557-66T(C) compaction test method. Fill placement should be in lifts no greater than eight inches loose thickness and compacted with sheepsfoot rollers.

5. Provide riprap slope protection at the toe to reduce the amount of erosion due to wave action. Approximately 1500 cubic yards will be required. Riprap should consist of material as specified in Scheme No. 2, paragraph 1.

6. Provide an 8- to 10-foot wide bench approximately halfway up the slope to allow for collection and diversion of surface water.

7. Upon completion of the compacted fill, the slope surface should be planted with deep-rooted vegetation to retard erosion and sloughing.

8. The drainage ditch located on the top of slope should be concrete-lined as previously recommended under Scheme No. 1.

IX ILLUSTRATIONS

RF 2

SEPTIC TANKS

LEACH FIELD

100

TEST BORING 4

3

SHALLOW MUD FLOWS

SHALLOW MUD FLOWS

SPRINGS & SEEPAGE

80

10 9 50 40 30 20 10

Pacific Ocean

SECTION LINES A B

SWITCHYARD ACCESS ROAD

WAREHOUSE

A'

PLANT ACCESS ROAD

EDGE OF ROAD

EDGE OF BERM

FILL SLOPE

CULVERT

B'

2

DRAINAGE PRIOR TO EXCAVATION OF DRAINAGE DITCH

LANDSLIDE

GULLY

EROSION

AREA

60 50 40 30 20 10

1

TOP OF EXISTING FILL

TOP OF DITCH
TOE OF FILL

DRAINAGE DITCH

FILL SLOPE

TOP OF DITCH
TOE OF FILL

140

120

100

130

TOE OF FILL

TO CLIFF EDGE.

NORTH

SCALE: 1" = 50'
CONTOUR INTERVAL = 10'

HARDING, MILLER, LAWSON & ASSOCIATES
Consulting Engineers

Job No: 569,010.04 Appr: SRK Date 5'14'70

SITE PLAN
Landslide
PG&E - Diablo Canyon

PLATE 1

PRINTED ON DATAPRINT NO 101-10

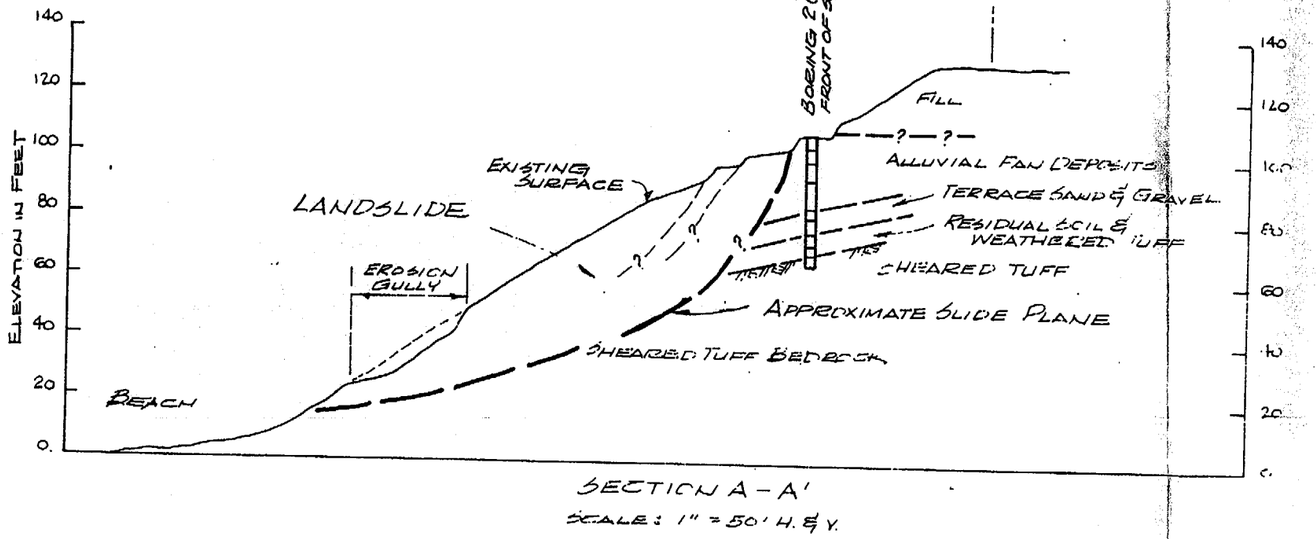

SECTION A-A'

SCALE: 1" = 50' H. & V.

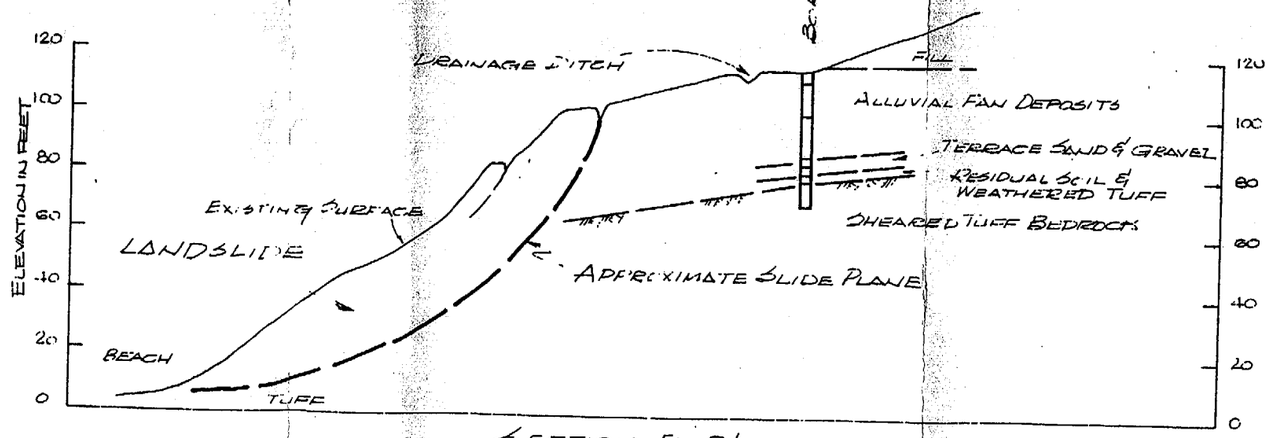

SECTION B-B'

SCALE: 1" = 50' H. & V.

HARDING, MILLER, LAWSON & ASSOCIATES
Consulting Engineers

Job No. 569,010.04 Appr: JRK Date 5/14/70

CROSS SECTIONS
Landslide
Pleasant Hill - Diablo Canyon

PLATE 2

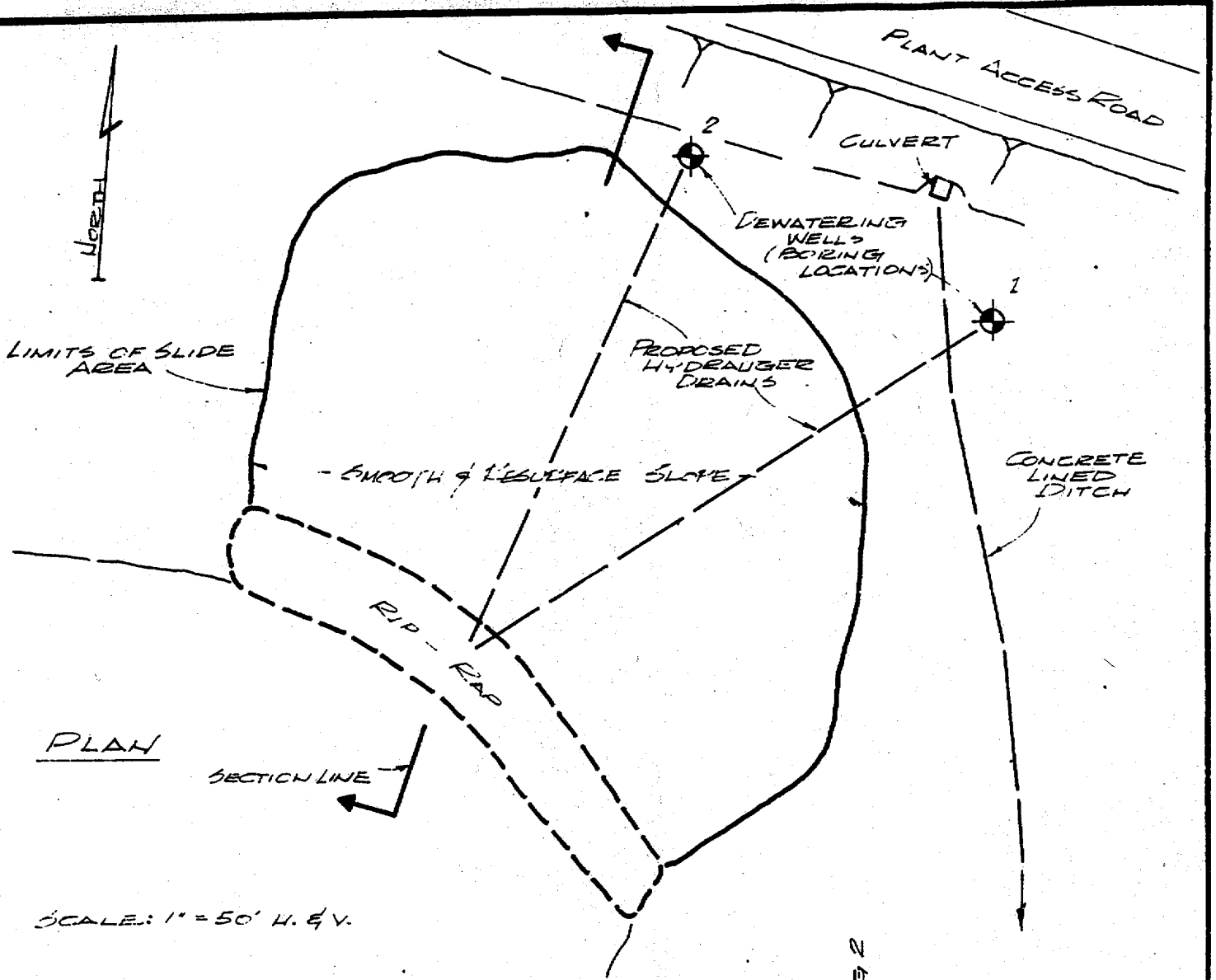

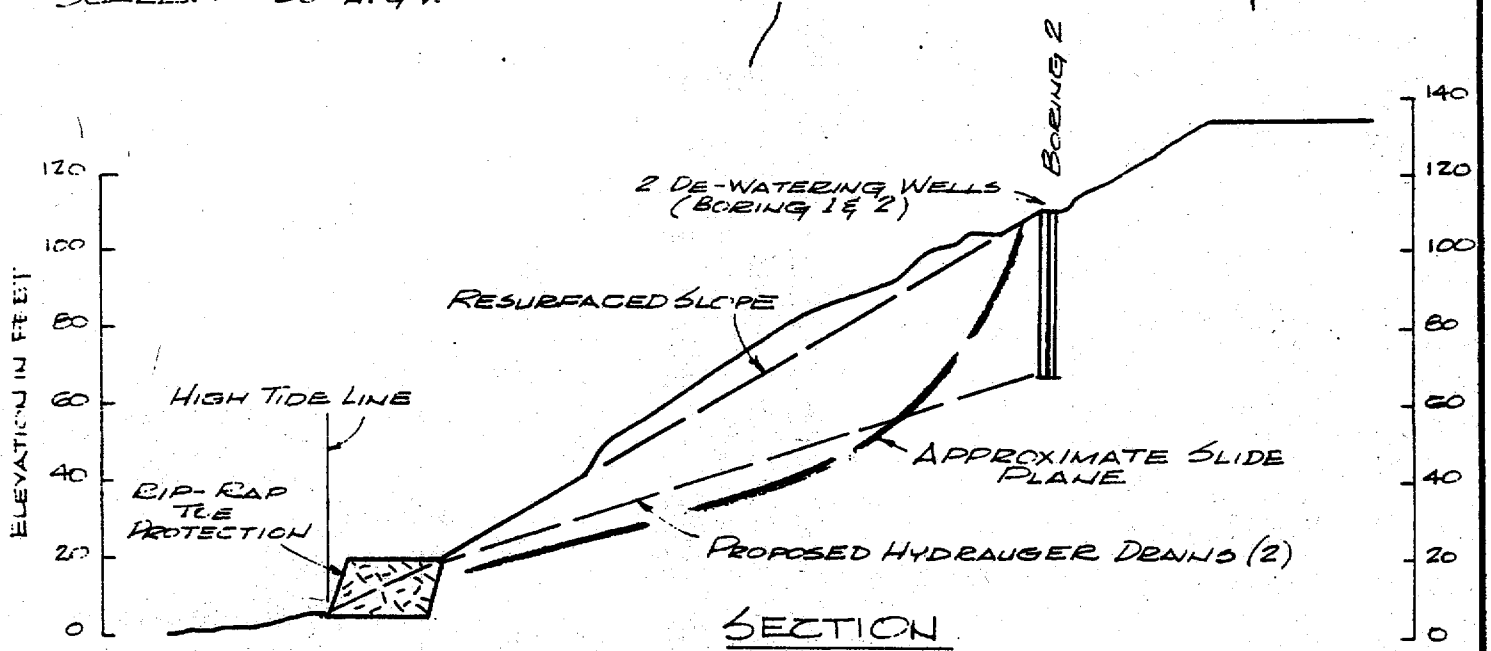

HARDING, MILLER, LAWSON & ASSOCIATES *Consulting Engineers*	SCHEME 1 Slope Stabilization Landslide PG&E - Diablo Canyon	**PLATE 3**
Job No: 369.010.04 Appr: SRL Date 5/14/75		

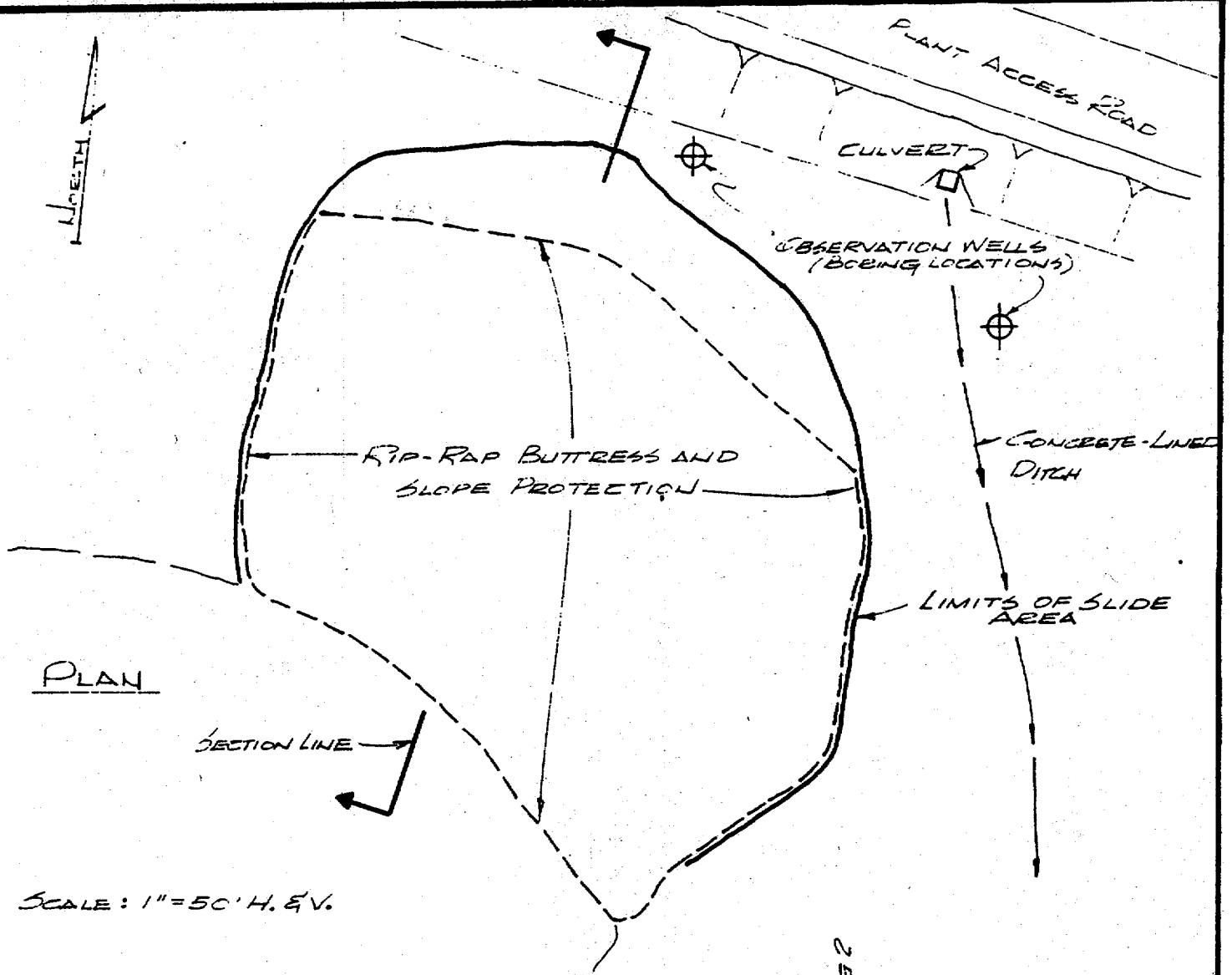

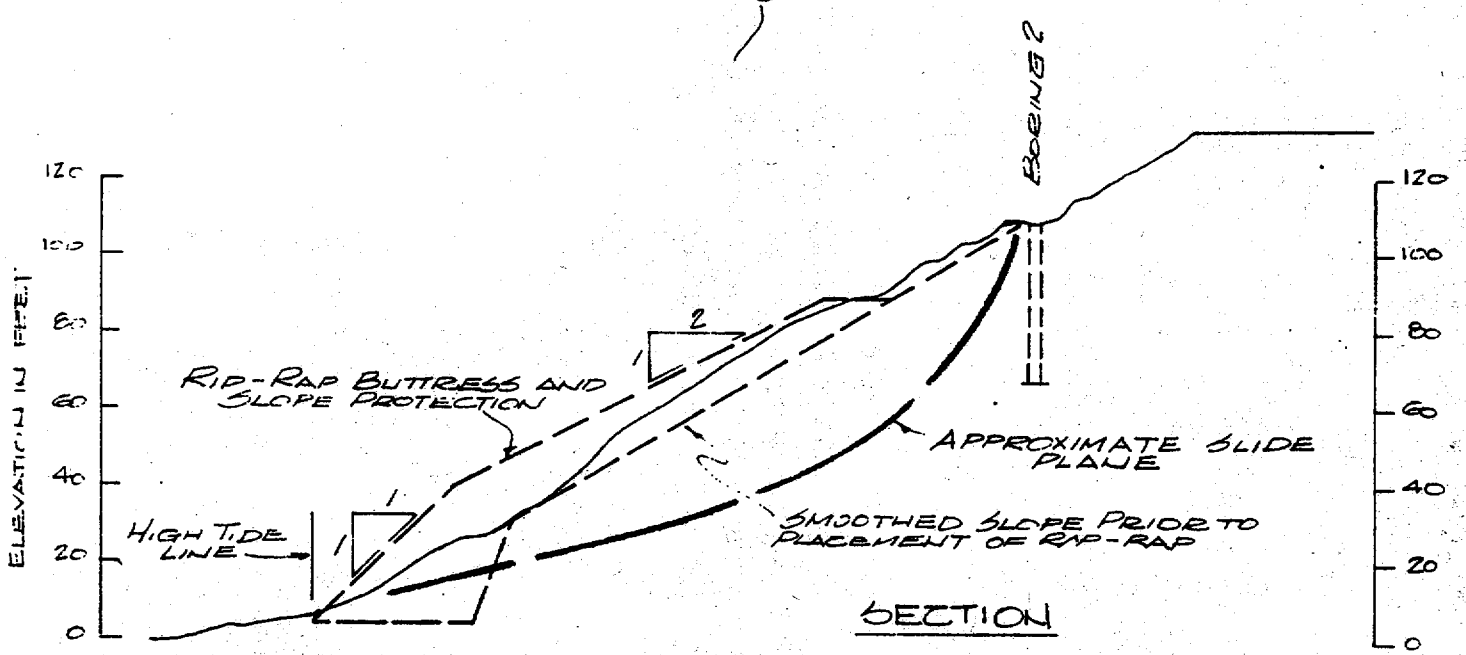

HARDING, MILLER, LAWSON & ASSOCIATES *Consulting Engineers*	SCHEME 2 Slope Stabilization Landslide P.G.&E. - Diablo Canyon	**PLATE 4**
Job No: [illegible] 010 04 Appr: SPK Date [illegible] 14 70		

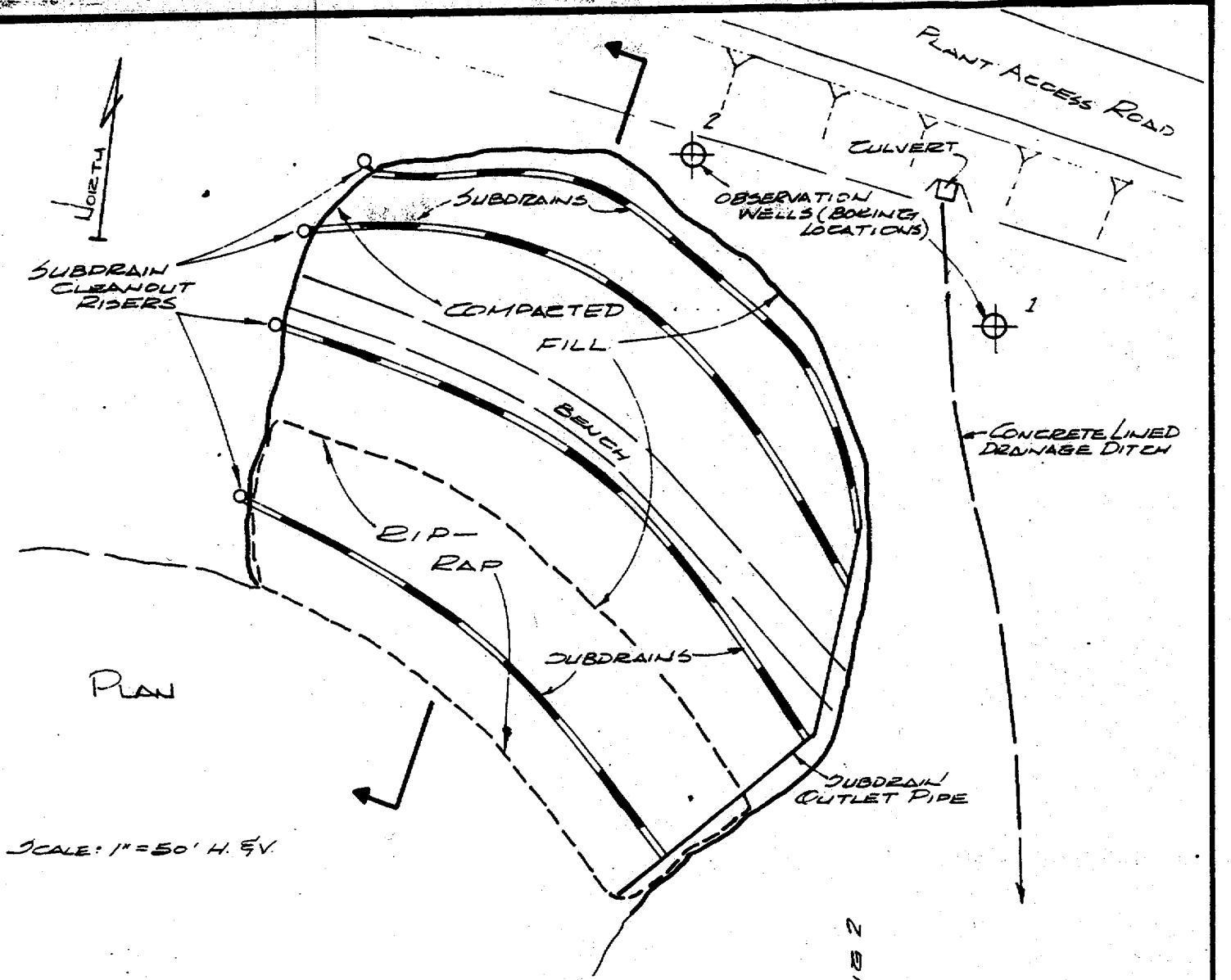

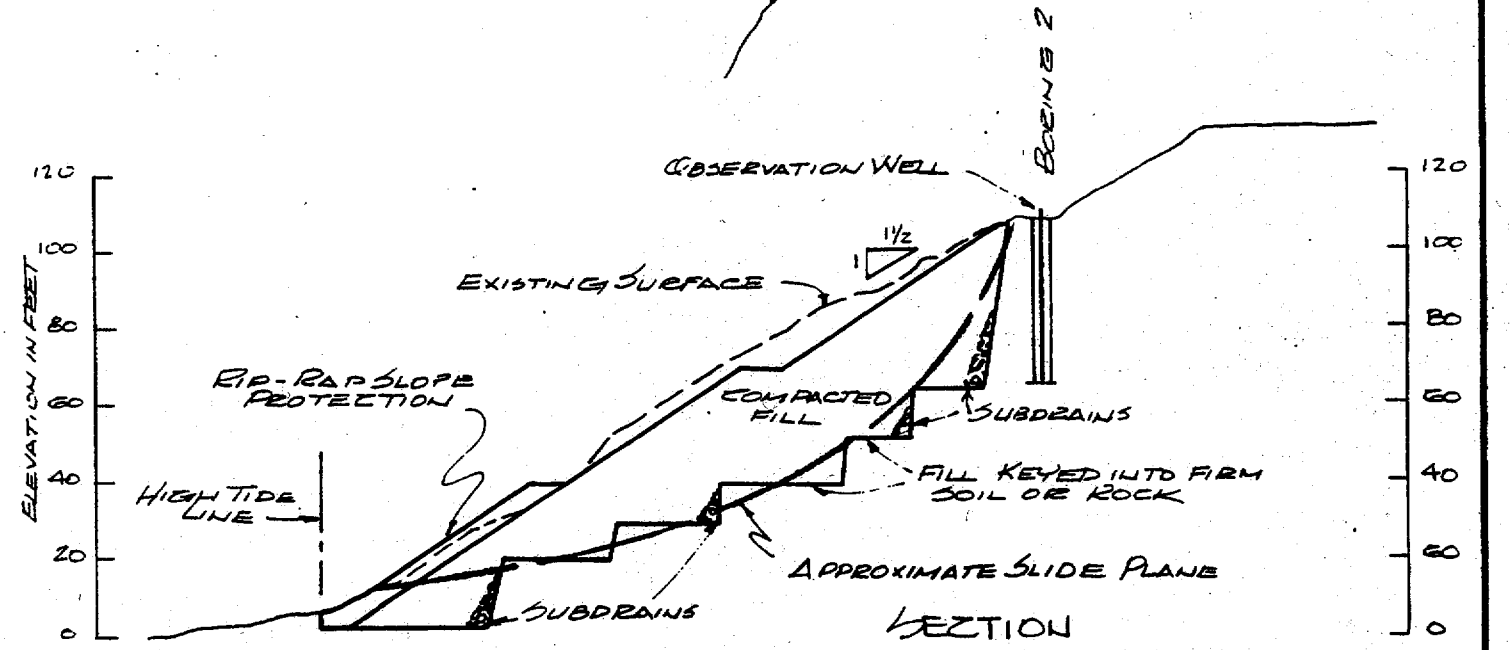

HARDING, MILLER, LAWSON & ASSOCIATES *Consulting Engineers*	SCHEME 3 Slope Stabilization Landslide PG&E - Diablo Canyon	**PLATE 5**
Job No: 569,010.04 Appr: SPK /la Date 5/15/70		

LOG OF BORING 1

Equipment 24" Diameter Bucket Auger

Elevation 111.8 Date 2/17/70

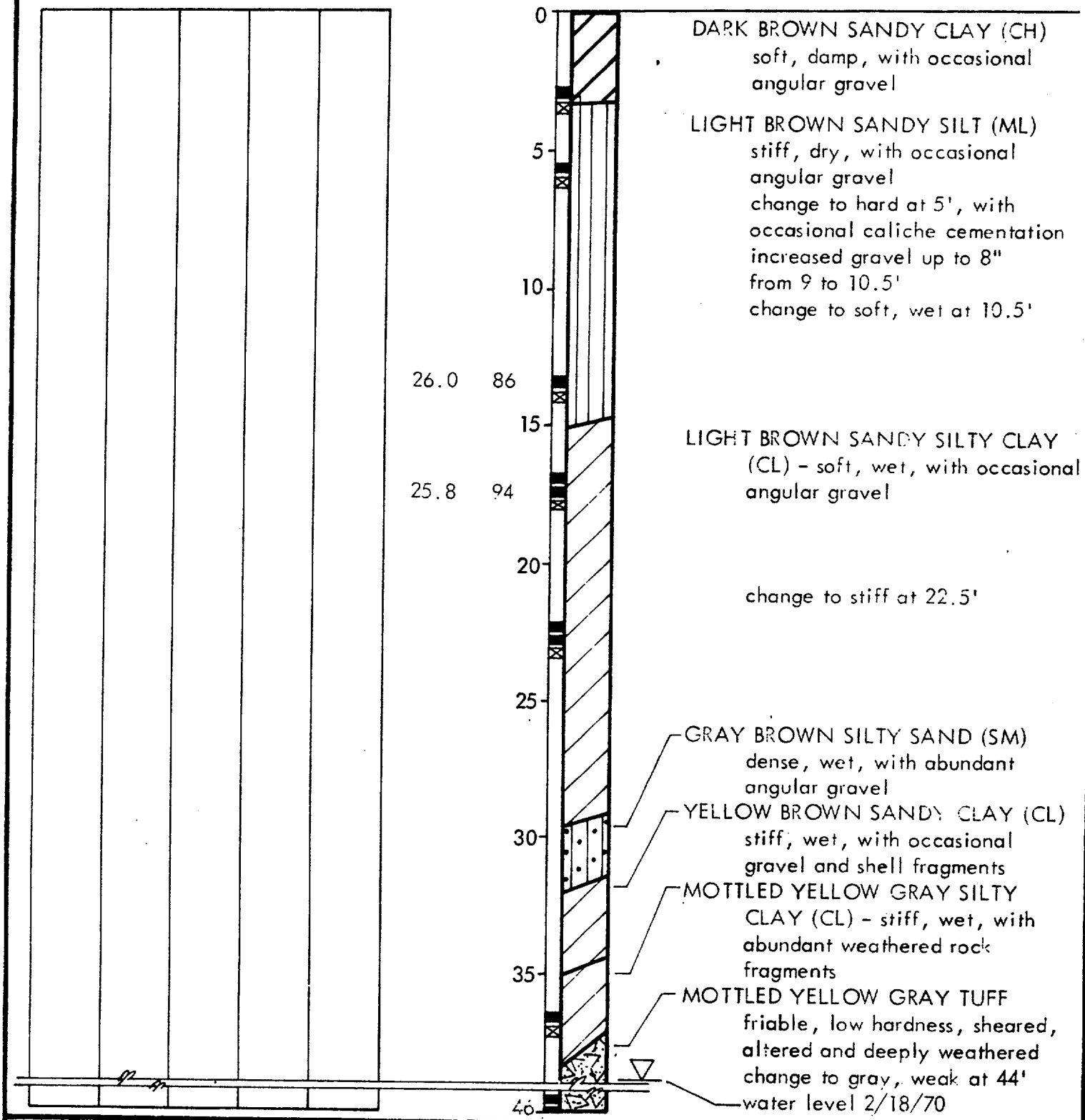

HARDING, MILLER, LAWSON & ASSOCIATES

Consulting Engineers

Job No: 569,010.04 Appr: SRK/iw Date 3/18/70

LOG OF BORING 1

Landslide

PG&E - Diablo Canyon

PLATE 6

LOG OF BORING 2

Equipment 24" Diameter Bucket Auger

Elevation 1110.8 Date 2/17/70

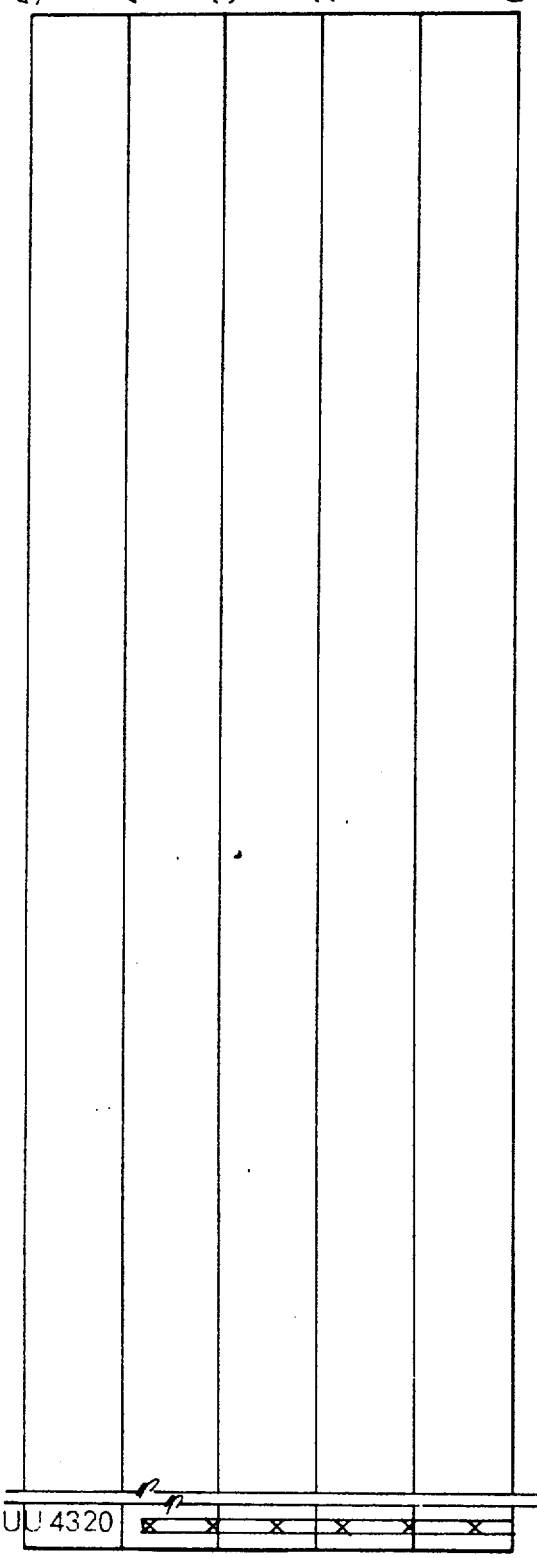

Sample	Depth (ft)	Dry Density (pcf)	Moisture Content (%)	
	0			DARK BROWN SANDY CLAY (CH) soft, damp, with occasional angular gravel
	5			LIGHT BROWN SANDY SILT (ML) stiff, damp, with abundant angular gravel with occasional gravel up to 6" at 5'
	10	93	25.4	LIGHT BROWN SANDY CLAY (CL) soft, wet, with occasional gravel change to firm at 9.5' change to soft at 11'
	15	87	27.9	LIGHT BROWN SANDY CLAYEY SILT (ML) - soft to medium stiff, wet, with occasional angular gravel
	20			LIGHT BROWN SILTY CLAY (CL) stiff, moist, with slight porosity
	25			LIGHT BROWN SILTY SAND (SM) dense, wet
				BROWN GRAVELLY SAND (SP) medium dense, moist, with silt binder
	30			MOTTLED GRAY BROWN CLAYEY SILT (ML) - soft, moist, with occasional angular gravel
	35			MOTTLED ORANGE GRAY GRAVELLY CLAY (CL) - firm, moist, with abundant rock fragments
				MOTTLED ORANGE GRAY TUFF soft to friable, low hardness, sheared, altered and moderately weathered
UU 4320	41	87	33.0	water level 2/19/70 at 40.5'

HARDING, MILLER, LAWSON & ASSOCIATES

Consulting Engineers

Job No: 569,010.04 Appr: SRK/jw Date 3/18/70

LOG OF BORING 2

Landslide

PG&E - Diablo Canyon

PLATE 7

LOG OF BORING 3

Equipment 24" Diameter Bucket Auger

Elevation 100.8 Date 2/18/70

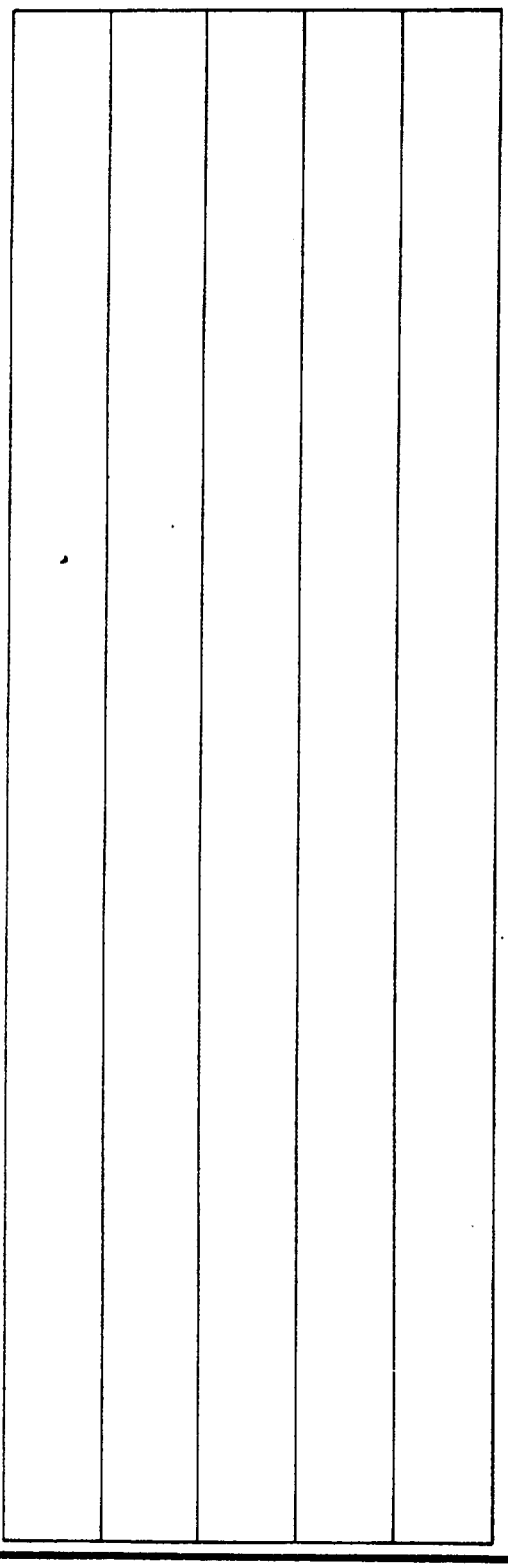

DARK BROWN SANDY CLAY (CH)
soft, damp, with occasional angular gravel

LIGHT BROWN SANDY SILT (ML)
firm, damp, with occasional angular gravel
up to 4" gravel at 7'
grading clayey at 8', with caliche cementation

slightly porous and moist at 14'

BROWN SILTY SAND (SM)
medium dense, moist, with occasional gravel

ORANGE BROWN SANDY CLAY (CL)
stiff, damp, with abundant rock fragments

ORANGE BROWN TUFFACEOUS SILTSTONE - weak, moderately hard, closely fractured, moderately weathered

(no free water observed)

HARDING, MILLER, LAWSON & ASSOCIATES
Consulting Engineers

Job No: 569,010.04 Appr: SRK/jw Date 3/18/70

LOG OF BORING 3
Landslide
PG&E - Diablo Canyon

PLATE **8**

LOG OF BORING 4

Equipment 24" Diameter Bucket Auger

Elevation 90.4 Date 2 19 70

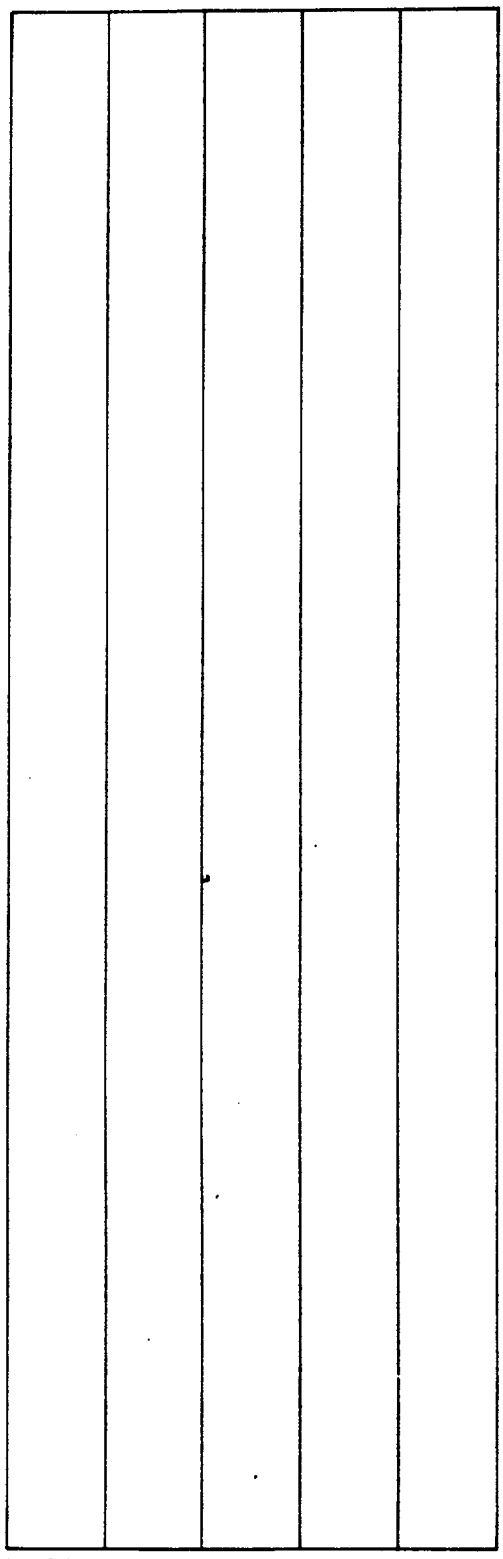

Moisture Content (%)	Dry Density (pcf)	Depth (ft)	Sample	
		0		BLACK SANDY CLAY (CH) soft, moist, with occasional angular gravel
24.8	77			
		5		MOTTLED YELLOW BROWN SILTY CLAY (CH) - soft, wet, with occasional rock fragments change to stiff at 8'
		10		BROWN GRAVELLY SANDY CLAY (CL) - firm, moist, with abundant rock fragments
		15		BLACK SHALE moderately strong, hard, closely fractured, slightly weathered change to strong, very hard at 15' auger refusal at 16'
		20		(no free water observed)
		25		
		30		
		35		
		40		

HARDING, MILLER, LAWSON & ASSOCIATES

Consulting Engineers

Job No: 569,010.04 Appr: SRH/jw Date 3/18/70

LOG OF BORING 4

Landslide

PG&E - Diablo Canyon

PLATE 9

Rr 3

MAJOR DIVISIONS				TYPICAL NAMES
COARSE GRAINED SOILS (MORE THAN HALF IS LARGER THAN #200 SIEVE)	GRAVELS (MORE THAN HALF COARSE FRACTION IS LARGER THAN NO. 4 SIEVE SIZE)	CLEAN GRAVELS WITH LITTLE OR NO FINES	GW	WELL GRADED GRAVELS, GRAVEL - SAND MIXTURES
			GP	POORLY GRADED GRAVELS, GRAVEL - SAND MIXTURES
		GRAVELS WITH OVER 12% FINES	GM	SILTY GRAVELS, POORLY GRADED GRAVEL - SAND - SILT MIXTURES
			GC	CLAYEY GRAVELS, POORLY GRADED GRAVEL - SAND - CLAY MIXTURES
	SANDS (MORE THAN HALF COARSE FRACTION IS SMALLER THAN NO. 4 SIEVE SIZE)	CLEAN SANDS WITH LITTLE OR NO FINES	SW	WELL GRADED SANDS, GRAVELLY SANDS
			SP	POORLY GRADED SANDS, GRAVELLY SANDS
		SANDS WITH OVER 12% FINES	SM	SILTY SANDS, POORLY GRADED SAND - SILT MIXTURES
			SC	CLAYEY SANDS, POORLY GRADED SAND - CLAY MIXTURES
FINE GRAINED SOILS (MORE THAN HALF IS SMALLER THAN #200 SIEVE)	SILTS AND CLAYS (LIQUID LIMIT LESS THAN 50)		ML	INORGANIC SILTS AND VERY FINE SANDS, ROCK FLOUR, SILTY OR CLAYEY FINE SANDS, OR CLAYEY SILTS WITH SLIGHT PLASTICITY
			CL	INORGANIC CLAYS OF LOW TO MEDIUM PLASTICITY, GRAVELLY CLAYS, SANDY CLAYS, SILTY CLAYS, LEAN CLAYS
			OL	ORGANIC CLAYS AND ORGANIC SILTY CLAYS OF LOW PLASTICITY
	SILTS AND CLAYS (LIQUID LIMIT GREATER THAN 50)		MH	INORGANIC SILTS, MICACEOUS OR DIATOMACIOUS FINE SANDY OR SILTY SOILS, ELASTIC SILTS
			CH	INORGANIC CLAYS OF HIGH PLASTICITY, FAT CLAYS
			OH	ORGANIC CLAYS OF MEDIUM TO HIGH PLASTICITY, ORGANIC SILTS
HIGHLY ORGANIC SOILS			Pt	PEAT AND OTHER HIGHLY ORGANIC SOILS

UNIFIED SOIL CLASSIFICATION SYSTEM

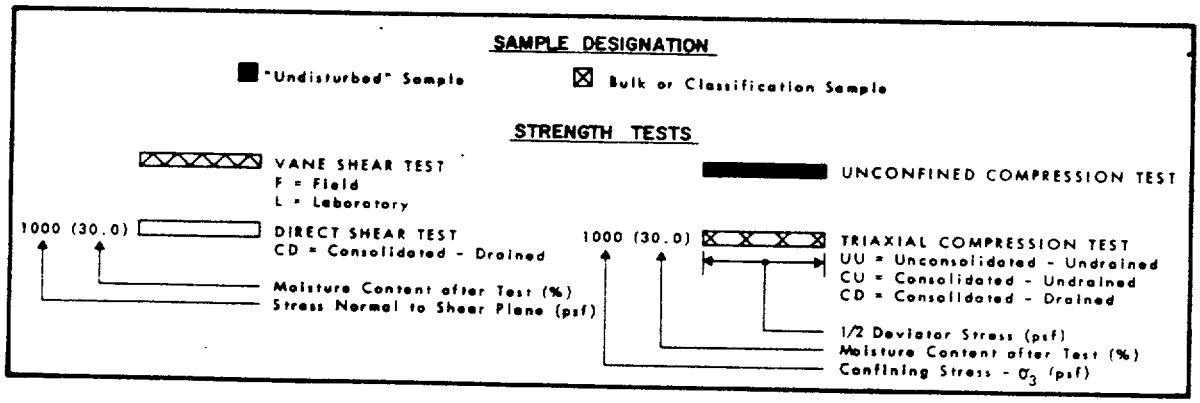

KEY TO TEST DATA

HARDING, MILLER, LAWSON & ASSOCIATES
Consulting Engineers

Job No: [illegible] Appr: SRK Date 5/14/7[illegible]

SOIL CLASSIFICATION CHART AND KEY TO TEST DATA

P G&E - Diablo Canyon

PLATE 10

DISTRIBUTION

3 copies: Pacific Gas and Electric Company
245 Market Street
San Francisco, California 94106

Attention: Mr. Richard Bettinger,
Supervising Civil Engineer

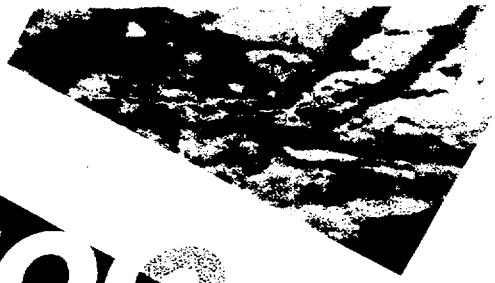

rocscience

Geomechanics Software & Research

User's Guide

Swedge

Probabilistic analysis of the geometry and stability of surface wedges

Designed for Windows 95/98/NT©

Swedge

Probabilistic analysis of the geometry and stability of surface wedges

User's Guide

Table of Contents

Quick Tour of Swedge 21

Probabilistic Analysis 39

Adding Support 57

Getting Started

SWEDGE is designed to work on Windows 95, 98 and Windows NT 4.0 operating systems.

To install SWEDGE on your computer:

1. Insert the CD-ROM.
2. Setup should begin automatically displaying the main Rocscience Installation window.
3. If not, select Add / Remove Programs from the Control Panel and click on the Install button. Follow the directions until the main Rocscience Installation window is displayed.
4. Click on the SWEDGE button.
5. Click on the INSTALL FULL VERSION button.
6. Follow the installation instructions. During installation you will be asked to enter your seventeen character alphanumeric serial number. Enter the serial number located on the outside of the CD case to install the program. Proceed until the installation is complete and you are back to the Rocscience Installation window.
7. Click on the RETURN button.
8. If you have NOT previously installed the hardlock driver software for any other Rocscience program proceed with step 9. Otherwise go to step 13.
9. Click on the HARDLOCK button.
10. Click on the INSTALL DRIVER FOR 95,98,NT button.

11. Proceed until the hardlock driver installation is complete and you are back to the Rocscience Installation window.

12. Click on the RETURN button.

13. Click on the EXIT button.

14. To run SWEDGE, you will also need the hardlock supplied with the program. The hardlock must be attached to the parallel port on your computer during execution of the program. Attach the SWEDGE hardlock to the parallel port of your computer.

15. The installation process creates a ROCSCIENCE menu in your START...PROGRAMS menu. In the ROCSCIENCE menu there will be an SWEDGE menu containing the SWEDGE application. Run the SWEDGE application.

16. If you are a first time user, read the Introduction and Tutorial chapters of this manual, to get acquainted with the features of SWEDGE.

Hints about this Manual

This manual is intended as a hands-on, getting started user's guide. For more information on any SWEDGE options which are not discussed in these pages, consult the SWEDGE Help system. In the tutorial chapters, instructions such as:

Select: Analysis → Input Data

are used to navigate the menu selections.

When a toolbar button is displayed in the margin, as shown above, this indicates that the option is available in the SWEDGE toolbar. *This is always the recommended and quickest way to use the option.*

Introduction

SWEDGE is a quick, interactive and simple to use analysis tool for evaluating the stability of surface wedges in rock slopes, defined by two intersecting discontinuity planes, the slope surface and an optional tension crack. Wedge stability can be assessed using either:

- DETERMINISTIC (safety factor), or
- PROBABILISTIC (probability of failure)

analysis methods. For a DETERMINISTIC analysis SWEDGE computes the factor of safety for a wedge of known orientation. For a PROBABILISTIC analysis, statistical input data can be entered to account for uncertainty in joint orientation and strength values. This results in a safety factor distribution, from which a probability of failure is calculated.

Other modeling features include:

- water pressure,
- external / seismic forces,
- rock bolt reinforcement.

In all cases, the assumed failure mode of the wedge is translational slip — rotational slip and toppling are not taken into account. The stability method used in SWEDGE can be found in "Rock Slope Engineering" (Rev. 3rd edition, E. Hoek & J.W. Bray, pp 341-351).

Swedge Input

SWEDGE computes the factor of safety for *translational slip of a tetrahedral wedge formed in a rock slope by*:

- two intersecting discontinuities (joint sets),
- the slope face,
- the upper ground surface, and
- a tension crack (optional).

Typical problem geometry is illustrated below (Ref. 1).

LEGEND

1 , 2 = Failure planes (2 intersecting joint sets)
3 = Upper ground surface
4 = Slope face
5 = Tension crack
H1 = Slope height referred to plane 1
L = Distance of tension crack from crest, measured along the trace of plane 1.

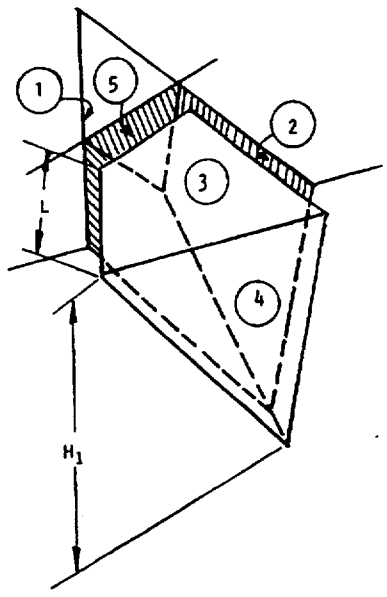

Figure 1-1: Typical wedge geometry for SWEDGE analysis (Ref.1)

When a pair of discontinuities are selected at random from a set of field data, it is not known whether:

- the planes could form a wedge (the line of intersection may plunge too steeply to daylight in the slope face or it may be too flat to intersect the upper ground surface).
- one of the planes overlies the other (this affects the calculation of the normal reactions on the plane).
- one of the planes lies to the right or the left of the other plane when viewed from the bottom of the slope.

In order to resolve these uncertainties, the solution has been derived in such a way that:

- Either of the planes may be labeled 1 (or 2).
- Allowance has been made for one of the planes overlying the other (this is illustrated in Figure 1-2)
- The crest can overhang the base of the slope.
- Contact may be lost on either plane (this is dependent on wedge geometry, and also on the magnitude of the water pressures acting on the planes).

A check on whether the two planes do form a wedge is included in the solution at an early stage. In addition, SWEDGE also examines how the tension crack intersects the other planes, accepting only those cases where the tension crack truncates the wedge in a kinematically admissible manner.

The SWEDGE stability analysis has been derived from a solution presented in Ref. 1. For a complete and detailed description of this analysis, consult this reference.

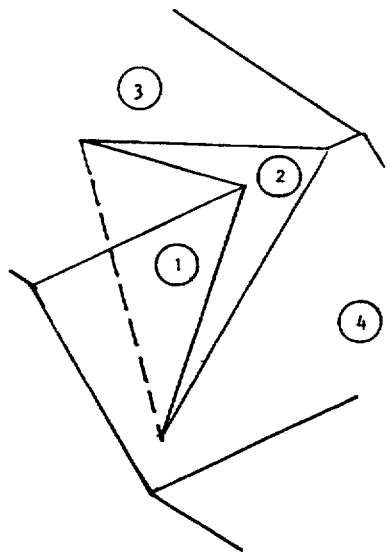

Figure 1-2: Situation where wedge is formed, and one plane overlies the other.

Joint Sets

Either joint set can be defined as Joint Set 1 or Joint Set 2 in the Input Data dialog.

However, remember that the Slope Height and the Trace Length of the Tension Crack *are measured with respect to Joint Set 1 – see Figure 1-1.*

Upper Slope and Face Slope

Note that there is no restriction on the inclination of the crest of the slope (the line of intersection of the upper and face slope planes), therefore the Dip Directions of the Upper Slope and Face Slope do not necessarily have to be the same.

The Upper Slope and Face Slope correspond to planes 3 and 4 in Figure 1-1.

Overhanging Slope

If the crest overhangs the base of the slope, select the Overhanging checkbox in the Input Data dialog, and enter appropriate Dip and Dip Directions of the Upper and Face Slope planes.

Tension Crack

The Trace Length of the Tension Crack is the distance of the tension crack from the crest, *measured along the trace of plane 1. See Figure 1-1. Length L is the trace length.*

SWEDGE examines how the tension crack intersects the other planes, and only accepts those cases where the tension crack truncates the wedge in the manner shown in Figure 1-1. If the tension crack plane does not form an acceptable wedge with the other planes, a warning message will be displayed when you select the Apply button to compute.

A Tension Crack is optional in SWEDGE, and can be excluded from a model by de-selecting the Tension Crack checkbox in the Input Data dialog.

Slope Height

The Slope Height is the vertical distance H1 in Figure 1-1, *referred to plane 1.*

External Force

A single external force (eg. a blast acceleration acting in a known direction) can be applied to the wedge, by selecting the External Force checkbox, and entering a direction and magnitude.

External force can also be applied through the use of rock bolts. See the Adding Support tutorial at the end of this manual for details.

Water Pressure

In the SWEDGE factor of safety calculation, *it is assumed that extreme conditions of very heavy rainfall occur, and that in consequence the fissures (failure planes) are completely full of water. Further, it is assumed that the pressure varies from zero at the free faces to a maximum value at some point on the line of intersection of the two failure planes.*

SWEDGE calculates ***average values*** of water pressure on each failure plane as follows (Ref. 1):

With NO Tension Crack

$$u_1 = u_2 = \gamma_w \cdot H_w / 6 \qquad \text{Eqn 1.1a}$$

where: u_1 and u_2 are the average values of water pressure on failure planes 1 and 2

γ_w = unit weight of water

H_w = total height of the wedge

With Tension Crack

$$u_1 = u_2 = u_5 = \gamma_w \cdot H_{5w} / 3 \qquad \text{Eqn. 1.1b}$$

where: u_1, u_2 and u_5 are the average values of water pressure on the failure planes 1 and 2, and the tension crack, respectively

γ_w = unit weight of water

H_{5w} = depth of bottom vertex of the tension crack below the upper ground surface

The above formulae are simple estimations which are useful in the absence of more precise information.

To vary water pressure in SWEDGE, alter the Unit Weight of water in the Input Data dialog.

Varying the Water Pressure

- To simulate a "dry" slope, the user can de-select the Water Pressure checkbox in the Input Data dialog, or enter a Unit Weight of zero.
- To simulate intermediate water pressures, the user can effectively vary the water pressure by varying the unit weight of water between zero and the actual unit weight. This allows the user to perform a sensitivity analysis on the effect of water pressure on the safety factor of the wedge.

Seismic Force

Seismic Force can be applied to the wedge, by selecting the Seismic checkbox in the Input Data dialog, and entering the following data:

Seismic Coefficient

A dimensionless number defining the seismic acceleration as a fraction of the acceleration due to gravity. Typically the Seismic Coefficient might be around 0.1 to 0.2. If α = Seismic Coefficient, g = acceleration due to gravity = 9.81 m/s^2, and m = mass of the wedge, then the Seismic Force applied to the wedge, $F = m \alpha g$.

Direction

- "Line of Intersection" will apply the Seismic Force in the direction (PLUNGE and TREND) of the Line of Intersection of Joint Sets 1 and 2.
- "Horiz. & Inters. Trend" will apply the Seismic Force horizontally, but with the same TREND as the Line of Intersection of Joint Sets 1 and 2.
- User Defined allows the user to define any direction for the Seismic Force.

Probabilistic Input

If the Analysis Type is Probabilistic, the user can define the following random variables in the Probabilistic Input Data dialog:

- Dip and Dip Direction of all planes (ie. Joint Sets 1 and 2, Upper and Face Slope, and Tension Crack).
- The strength (Cohesion and Friction Angle) of Joint Sets 1 and 2.

For each random variable, enter an appropriate:

- Mean
- Standard deviation (if applicable)
- Relative minimum and maximum values

NOTE that the minimum / maximum values are specified as RELATIVE numbers (ie. distance from the mean), rather than as absolute values. All references below to "minimum" and "maximum" values refer to the actual values (ie. **mean – rel. min** and **mean + rel. max**), and not to the relative values entered in the Input Data dialog.

Statistical Distributions

To define a random variable, first choose a Statistical Distribution (also known as "Probability Density Function" or "pdf"). The five available distributions are:

- Normal
- Uniform
- Triangular
- Beta
- Exponential (only available for cohesion and friction angle)

Normal

The NORMAL (or Gaussian) distribution is the most common type of probability distribution function, and is generally used for probabilistic studies in geotechnical engineering. Unless there is a good reason to use one of the other four PDFs available in SWEDGE, it is recommended that the user choose the NORMAL "pdf".

For a NORMAL distribution, about 68% of observations should fall within one standard deviation of the mean, and about 95% of observations should fall within two standard deviations of the mean.

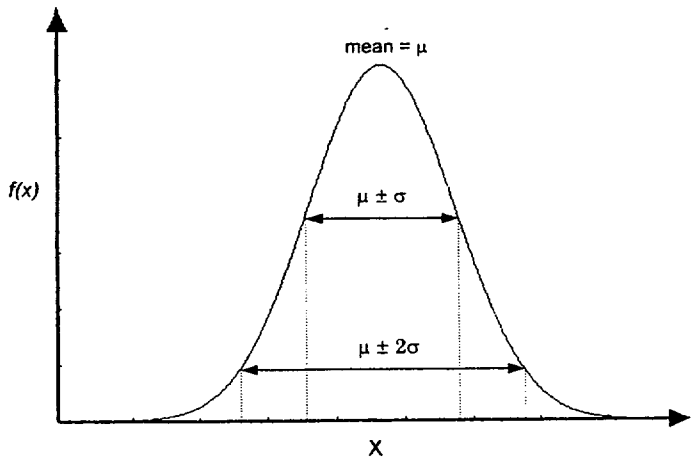

Figure 1-3: Normal probability density function, showing standard deviation ranges.

Truncated Normal Distribution

A truncated NORMAL distribution can be defined by setting the desired minimum and/or maximum values for the variable. For practical purposes, if the minimum and maximum values are at least 3 standard deviations away from the mean, you will obtain a complete normal distribution. If the minimum / maximum values are less than 3 standard deviations away from the mean, the distribution will be visibly truncated.

Uniform

A UNIFORM distribution can be used to simulate a random variation between two values, where all values in the range are equally probable.

A UNIFORM distribution is entirely specified by the minimum and maximum values. The mean value of a UNIFORM distribution is simply the average of the minimum and maximum values, and cannot be independently specified.

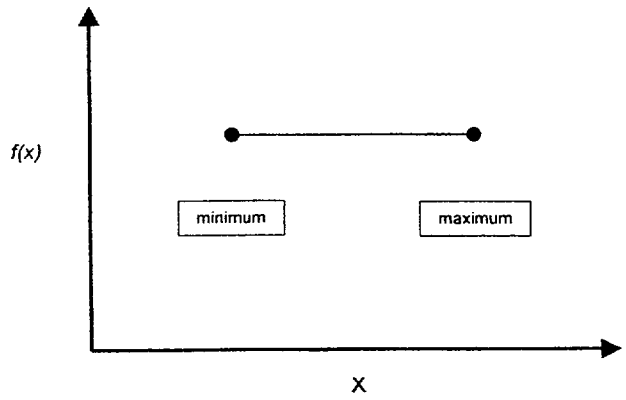

Figure 1-4: Uniform probability density function.

Triangular

You may wish to use a TRIANGULAR distribution in some cases, as a rough approximation to a random variable with an unknown distribution.

A TRIANGULAR distribution is specified by its minimum, maximum and mean values. It does not have to be symmetric, it can be skewed to the left or right by entering a mean value less than or greater than the average of the minimum and maximum values.

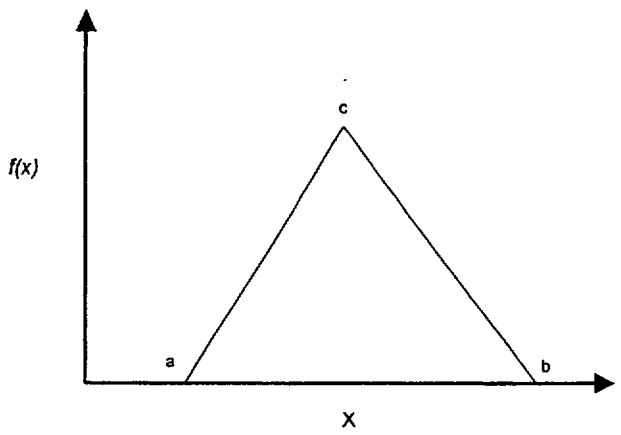

Figure 1-5: Triangular probability density function. Minimum = a, maximum = b, mode = c. For a symmetric distribution, mean = mode.

Note: for a non-symmetric TRIANGULAR distribution, the mean value is *not* equal to the mode. The mode is the value of the variable at the peak of the TRIANGULAR distribution. In general for a TRIANGULAR distribution, the mean is given by:

$$\text{mean} = \frac{\text{minimum} + \text{maximum} + \text{mode}}{3} \qquad \text{Eqn. 1.2}$$

1. If the distribution is symmetric, then the mean is equal to the mode.
2. For a left triangular distribution, the mode = minimum, and the mean = (2*minimum + maximum) / 3.
3. For a right triangular distribution, the mode = maximum, and the mean = (2*maximum + minimum) / 3.

Beta

The BETA distribution is a very versatile function which can be used to model several different shapes of probability density curves, as shown in the figure below.

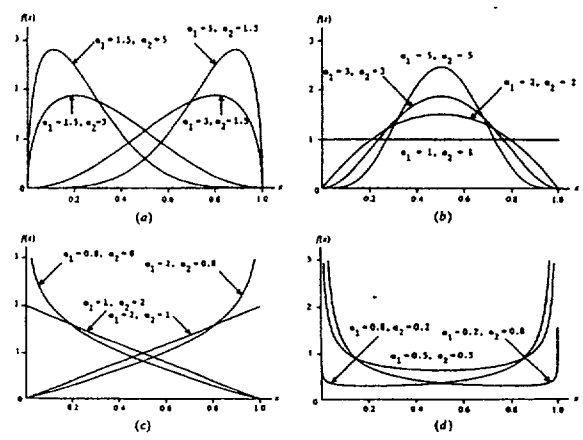

Figure 1-6: Beta (α1, α2) density functions (Ref. 3)

The form of the BETA distribution is determined by the shape parameters α1 and α2. Both α1 and α2 are always > 0. The relationship between the BETA distribution shape parameters and the SWEDGE input data is as follows:

$$\text{mean} = \frac{\alpha 1}{\alpha 1 + \alpha 2} \qquad \text{Eqn. 1.3}$$

$$\text{variance} = \frac{\alpha 1 \alpha 2}{(\alpha 1 + \alpha 2)^2 (\alpha 1 + \alpha 2 + 1)} \qquad \text{Eqn. 1.4}$$

The standard deviation is the *positive square root of the variance.*

Note that Equations 1.3 and 1.4 apply to a beta random variable on [0,1]. To rescale and relocate to obtain a beta random variable on [a,b] of the same shape, use the transformation a + (b–a)X.

Exponential

The EXPONENTIAL probability density function has also been made available in SWEDGE.

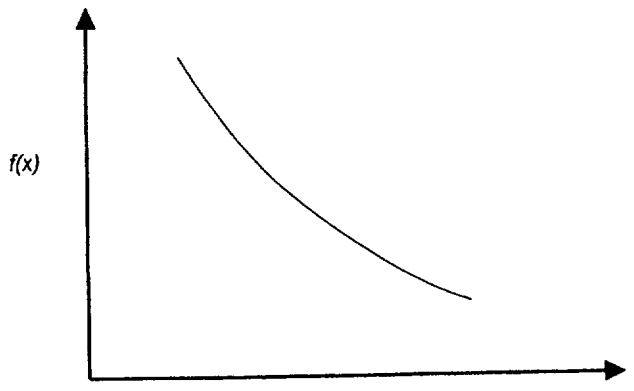

Figure 1-7: Exponential probability density function.

Note the following:

1. Since the range of values must always be positive for an EXPONENTIAL distribution, it has only been made available for the strength parameters (cohesion and friction angle), and not for the orientation parameters, since these may have negative ranges which would be invalid for an EXPONENTIAL distribution.

2. The mean is always equal to the standard deviation for an EXPONENTIAL distribution. This is a property of the EXPONENTIAL distribution, and cannot be altered by the user.

3. Like the NORMAL distribution, the EXPONENTIAL distribution can be truncated by entering the desired minimum and maximum values (the basic EXPONENTIAL distribution varies from zero to infinity).

The EXPONENTIAL distribution is sometimes used to define events, such as the occurrence of earthquakes or rockbursts, or quantities such as the length of joints in a rockmass. Of the currently defined statistical variables in SWEDGE, you may occasionally find it useful for modeling joint cohesion, for example.

Probability – Further Reading

An excellent introduction to probability theory in a geotechnical engineering context, can be found in Chapter 2 of Ref. 2.

More comprehensive and detailed information can be found in statistics textbooks. For example, Chapter 6 of Ref. 3 is an excellent guide to the selection of input probability distributions. Ref. 4 provides a summary of over 30 different probability density functions, in a quick-reference format.

Swedge Analysis

To run the SWEDGE analysis, simply select the Apply button in the Input Data dialog, after entering all your input data.

- If the Analysis Type = Deterministic, the Safety Factor will be immediately calculated and displayed in the lower right corner of the dialog, as well as in the toolbar.
- If the Analysis Type = Probabilistic, the Probability of Failure will be calculated and displayed in the toolbar.

A Probabilistic Analysis can be re-run at any time by selecting the Compute button in the toolbar.

Note that a Probabilistic Analysis can be re-run at any time, by selecting the Compute button in the toolbar. The Probability of Failure will not necessarily be the same, each time a Probabilistic Analysis is re-run.

Geometry Validation

SWEDGE always checks if the model geometry is valid, before proceeding to calculate a Safety Factor for a given wedge.

- If the Analysis Type = Deterministic, you will receive a warning message if there is a problem with your input data.
- If the Analysis Type = Probabilistic, validation is first performed on the mean Input Data. If the mean orientation data does not form a valid wedge, then the entire Probabilistic Analysis will be aborted, and you will receive a warning message. If the mean wedge is valid, but invalid wedges are generated during the statistical sampling, then these results are discarded, but the analysis is allowed to proceed. The Number of Valid Wedges for a Probabilistic Analysis can be found listed in the Analysis → Info Viewer option.

Sliding Planes

After a typical SWEDGE analysis, the analysis summary will indicate, for a given wedge:

Sliding along line of intersection (trend / plunge)

This indicates that the factor of safety accounts for sliding on ***both*** of the failure planes (joint sets). The **line of intersection** refers to the line of intersection of the two failure planes (Joint Set 1 and Joint Set 2).

Depending on wedge geometry and water pressure, sliding may take place along:

- ***Both failure planes***
- ***One failure plane***
- ***None (loss of contact)***

In some cases, depending on the geometry of the wedge and the magnitude of the water pressure, contact may be lost on **either** failure plane. In such cases, the analysis summary will show:

Sliding on Joint 1 or

Sliding on Joint 2

If the water pressure is too high, the wedge will 'float', and the analysis summary will indicate:

Contact Lost on Both Planes

Finally, if tension in the rock bolts is too high, the analysis summary may indicate:

Sliding UP Line of Intersection (trend / plunge)

indicating that the total rock bolt tension is high enough to potentially push the wedge 'up' the slope.

For a Deterministic Analysis, the sliding plane(s) will be indicated in the Input Data dialog, along with the Safety Factor. For a Probabilistic Analysis, this information is listed in the Info Viewer.

References

1. Hoek, E. and Bray, J.W. *Rock Slope Engineering*, Revised 3rd edition, The Institution of Mining and Metallurgy, London, 1981, pp 341 - 351.

2. Hoek, E., Kaiser, P.K. and Bawden, W.F. *Support of Underground Excavations in Hard Rock*, A.A.Balkema, Rotterdam, Brookfield, 1995.

3. Law, A.M. and Kelton, D.W. *Simulation Modeling and Analysis*, 2nd edition, McGraw-Hill, Inc., New York, 1991.

4. Evans, M., Hastings, N. and Peacock, B. *Statistical Distributions*, 2nd edition, John Wiley & Sons, Inc., New York, 1993.

Quick Tour of Swedge

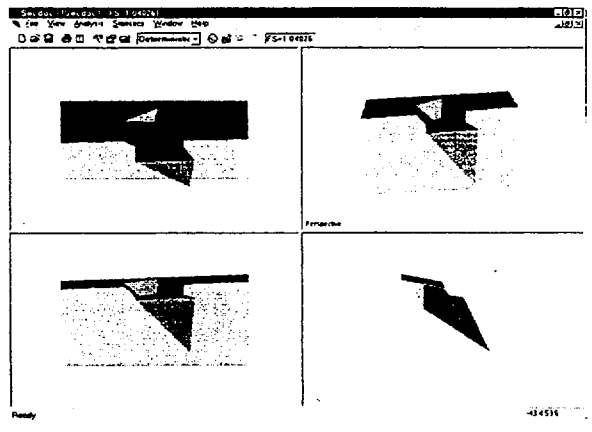

This "quick tour" will familiarize the user with some of the basic features of SWEDGE.

If you have not already done so, run SWEDGE by double-clicking on the SWEDGE icon in your installation folder. Or from the Start menu, select Programs → Rocscience → Swedge → Swedge.

If the SWEDGE application window is not already maximized, maximize it now, so that the full screen is available for viewing the model.

To begin creating a new model:

Select: File → New

A wedge model will immediately appear on your screen, as shown in the above figure. Whenever a new file is opened, the default input data will form a valid wedge.

The first thing you will notice is the four-view, split screen format of the display, which shows:

- TOP
- FRONT
- RIGHT and
- PERSPECTIVE

views of the model. The Top, Front and Right views are orthogonal with respect to each other (ie. viewing angles differ by 90 degrees).

Job Control

Job Control allows the user to enter a Job Title, and select a Unit System and Analysis Type.

Select: Analysis → Job Control

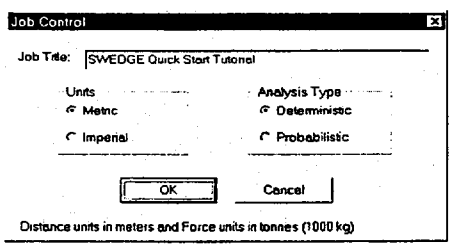

Enter "SWEDGE Quick Start Tutorial" as the Job Title. Leave Units = Metric and Analysis Type = Deterministic. Select OK.

- The Job Title will appear in the Info Viewer listing, discussed later in this tutorial.
- Units determines the length and force units used in the Input Data dialog (see the next section).
- Probabilistic SWEDGE analysis is covered in the next tutorial.

Input Data

Now let's see what input data was used to create this model.

Select: Analysis → Input Data

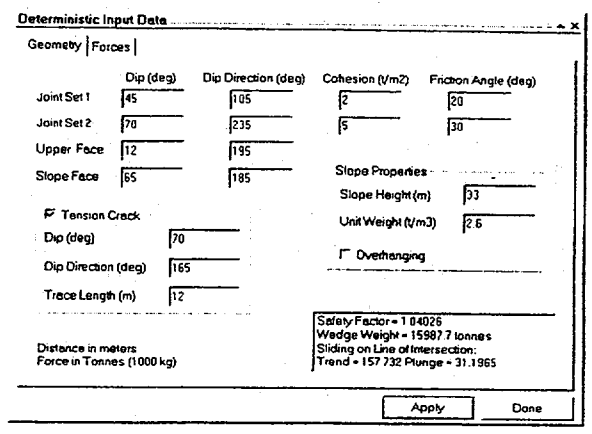

Figure 2-1: Input Data dialog (Deterministic).

The Geometry input data which you see in this dialog is the default input data, which forms a valid default wedge, each time a new file is started.

Quickly examine the input data in this dialog. See the introductory section of this manual for definitions of the SWEDGE input data. Do not change any values just yet, we will be coming back to this shortly.

Before you close the dialog, notice the Safety Factor, Wedge Weight etc information displayed in the lower right corner. The Safety Factor (FS = ...) is also displayed in the SWEDGE toolbar, at the top of the screen.

Now close the dialog by selecting the ✕ in the upper right corner.

Manipulating the View

The LEFT and RIGHT mouse buttons can be used to interactively manipulate the view as follows:

- The Perspective view of the model allows the model to be rotated for viewing at any angle with the LEFT mouse button.
- The wedge can be moved out of the slope with the RIGHT mouse button in any of the four views.

Rotating the Model

1. Press and HOLD the LEFT mouse button anywhere in the Perspective view. Notice that the cursor changes to a "circular arrow" symbol to indicate that you may rotate the model.
2. Now keep the LEFT mouse button pressed, and move the cursor around. The model is rotated according to the direction of movement of the cursor.
3. To exit the rotation mode, release the LEFT mouse button. Notice that the cursor reverts to the normal arrow cursor.
4. Repeat the above steps to rotate the model for viewing at any angle.

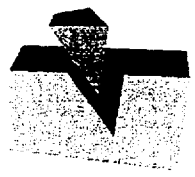

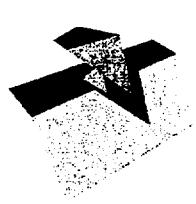

Moving the Wedge Out of the Slope

1. Press and HOLD the RIGHT mouse button anywhere in ANY of the four views. Notice that the cursor changes to an "up-down arrow" symbol.
2. Now, keep the RIGHT mouse button pressed, and move the cursor UP or DOWN. The wedge will slide UP or DOWN out of the slope. Note:
   - If your model does NOT have a Tension Crack, then the wedge will slide UP or DOWN along the Line of Intersection of Joint 1 and Joint 2.
   - If your model DOES have a Tension Crack, then the wedge will slide DOWN along the Line of Intersection of Joint 1 and Joint 2, and UP along the plane of the Tension Crack.
3. To exit this mode, release the RIGHT mouse button. Notice that the cursor reverts to the normal arrow cursor.

Resetting the Wedge

To reset the wedge in its normal position, click and RELEASE the RIGHT mouse button in any of the four views. The wedge will snap back to its normal position.

Rotating and Moving

The rotate and move options, described above, can be used in any order. That is, the model can be rotated after moving the wedge, and the wedge can be moved after rotating. This allows complete flexibility of viewing the slope and wedge from all possible angles.

Note that rotating the model only affects the Perspective view, while moving the wedge out of the slope affects all views (Top, Front, Right and Perspective).

Resizing the Views

You can change the relative size of the Top / Front / Right / Perspective views in a number of ways:

1. Double-clicking in any view will maximize that view. Double-clicking again in the maximized view, will restore the four view display.

Double-clicking in any view will maximize that view. Double-clicking again in the maximized view, will restore the four view display.

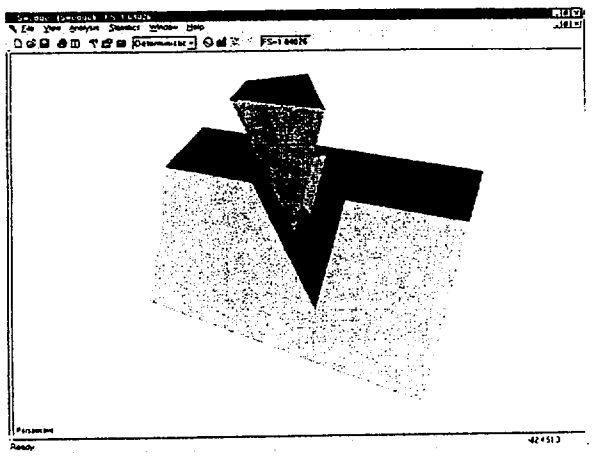

Figure 2-2: Maximized Perspective view.

2. Alternatively, hover the cursor over the vertical or horizontal dividers between the views, or over the intersection point of the four views. The cursor will change to a "parallel line" or "four arrow" symbol. Press and HOLD the LEFT mouse button, and drag to re-size the views.

3. Maximizing views can also be accomplished with the View → Layout options. To reset the four views to equal size, select View→ Layout → All Views.

Zooming

Zooming (from 50% to 800%) is available in the View → Zoom menu, to increase or decrease the displayed size of the model in all four views.

Individual views can be zoomed in or out using the Page Up / Page Down keys, or the + or – numeric keypad keys. You must first click in the view with the LEFT mouse button, to make it the active view.

Display Options

You may change the colours of the Slope, Wedge, Background and Bolts, and the Drawing Mode (Shaded or Wireframe) in the Display Options dialog.

Select: View → Display Options

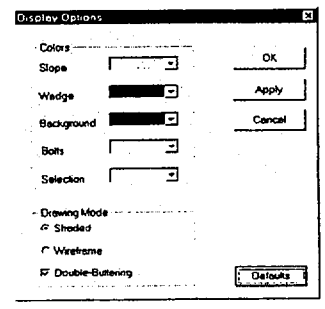

Select new slope, wedge and background colours, and hit the Apply button. Now change the Drawing Mode from Shaded to Wireframe, and hit Apply. Select the Defaults button to restore the defaults, and hit OK or Cancel to exit the dialog.

The "Selection" colour refers to the colour of selected bolts while using the Delete Bolt and Edit Bolt options. See the last tutorial in this manual for more information.

Note that the Cancel button in the Display Options dialog does NOT cancel any changes once they have been applied with the Apply button.

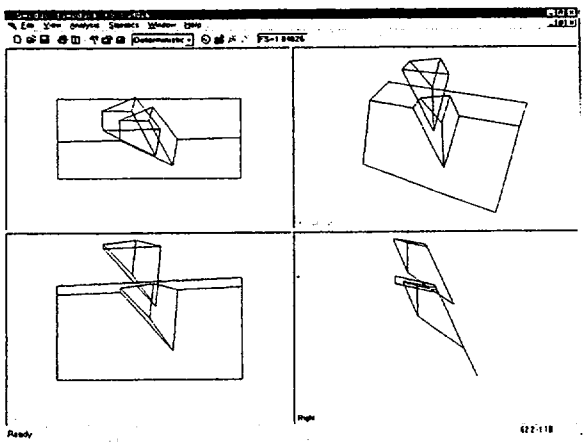

Figure 2-3: Wireframe Drawing Mode.

Changing the Input Data & Re-calculating the Safety Factor

Now let's experiment with changing the Input Data and re-calculating a new Safety Factor.

This is simply a matter of:

1. Entering the desired Input Data.
2. Selecting the Apply button.

For a Deterministic analysis, the Safety Factor is immediately calculated and displayed in the lower right corner of the dialog.

Select: Analysis → Input Data

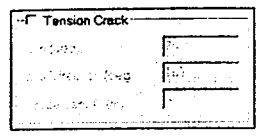

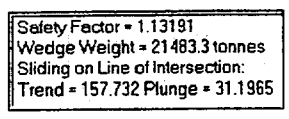

Let's first remove the Tension Crack, and observe the effect on Safety Factor and the wedge geometry.

Removing the Tension Crack

1. To remove the Tension Crack from the model, simply de-select the Tension Crack checkbox in the Input Data dialog.
2. Select the Apply button, and a new Safety Factor is immediately calculated. Removing the Tension Crack increased the Safety Factor from 1.04 to 1.13.
3. Select the Done button, to close the Input Data dialog, so that you can view the new wedge. It should appear as below.

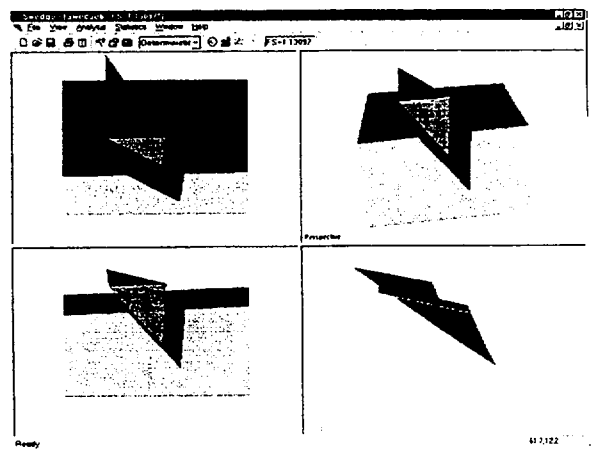

Figure 2-4: Wedge with tension crack removed.

Note that the Input Data dialog can also be minimized without closing it, by selecting the ▲ arrow in the upper right corner of the dialog.

Entering a New Wedge

Let's enter data for a completely different wedge.

Select: Analysis → Input Data

1. Enter the following data and select Apply.

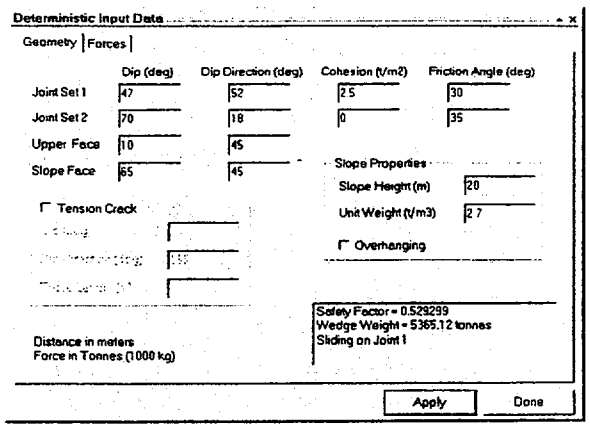

2. Select the Done button to close the dialog, or minimize it by clicking on the ▲ arrow, and you should see the following wedge, with a Safety Factor of 0.53.

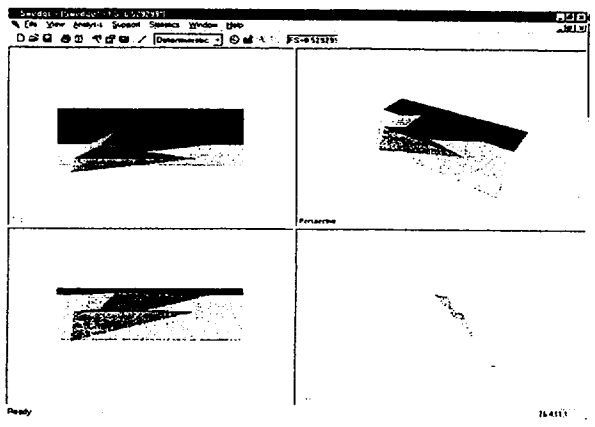

Figure 2-5: A new wedge.

Sliding Plane

Notice that in this case, the analysis summary in the Input Data dialog indicates the failure mechanism as "Sliding on Joint 1", rather than "Sliding along line of intersection". This is consistent with the model geometry, since Joint Set 2 dips at 70 degrees and has a cohesion of zero, and therefore has little influence on the wedge stability.

See the Introduction for more information on the sliding plane failure modes in SWEDGE.

Water Pressure

When Water Pressure is toggled on and the Unit Weight = 1 in the Input Data dialog, the factor of safety is calculated assuming extreme conditions of heavy rainfall. This means that maximum (average) values of water pressure are applied on the failure planes (and tension crack, if present). Parametric analysis of the effect of varying water pressure, can be achieved by varying the Unit Weight of water between 0 and 1.

For example:

1. Enter Unit Weight of water = 0.5. Select Apply.
2. The Safety Factor increases from 0.53 to 0.81.
3. Now toggle Water Pressure off (or enter Unit Weight = 0, this has the same effect). Select Apply.
4. The Safety Factor with no water pressure (ie. a completely dry slope) is 1.11. This is the maximum Safety Factor for this wedge, without installing rock bolt reinforcement.

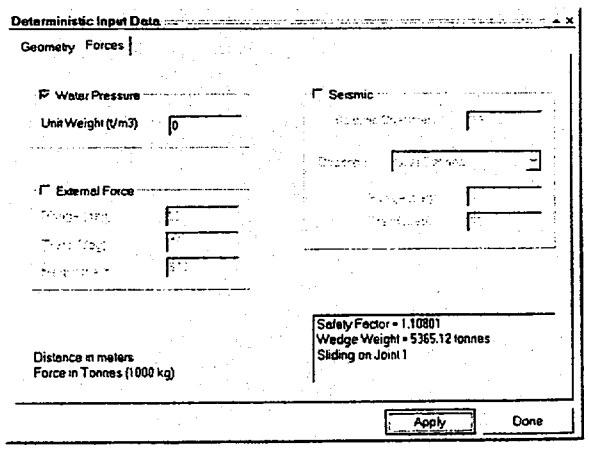

External Force

1. Toggle on the External Force checkbox.
2. Enter Plunge = 20, Trend = 45 and Magnitude = 500.
3. Select Apply.
4. The Safety Factor (with Water Pressure toggled off) drops to 0.97.

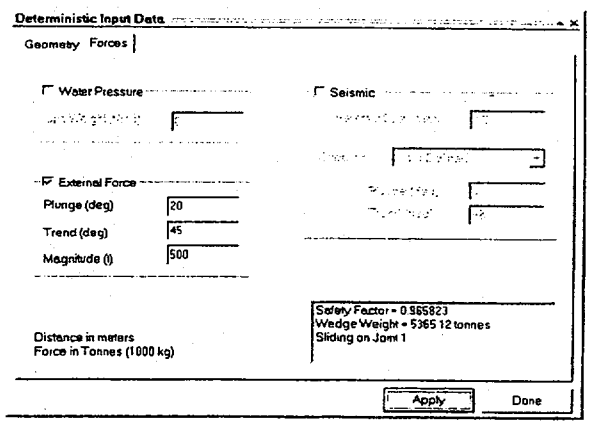

At this point we will note that rock bolts in SWEDGE are implemented in the analysis in exactly the same way as the External Force.

That is, rock bolts can be simulated by an equivalent External Force, or an External Force can be simulated by rock bolts. See the last tutorial in this manual, Adding Support, for more information.

Seismic Force

1. Toggle off the External Force checkbox, and toggle on the Seismic Force checkbox.

2. Enter a Seismic Coefficient of 0.2, and select the Direction as "User Defined", and enter Plunge = 0 and Trend = 52.

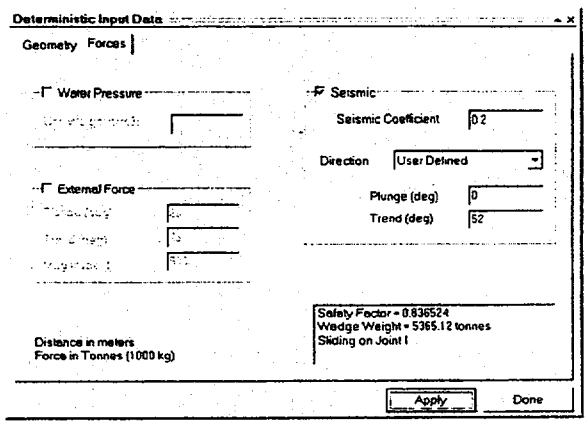

3. This will apply a force on the wedge F = 0.2 * g * m, where g = acceleration due to gravity and m = mass of the wedge. Note that the Trend is equal to the Dip Direction of Joint Set 1, which is the worst possible direction in this case, since the failure mode for this wedge already indicates Sliding on Joint 1.

4. Select Apply, and the Safety Factor now drops to 0.84.

More About the Input Data Dialog

You may not have noticed, but the Input Data dialog in SWEDGE works a little differently than a regular dialog:

1. It is known as a "roll-up" dialog, since it can be "rolled-up" (minimized) or "rolled-down" again, by selecting the ▲ or ▼ arrow in the upper right corner of the dialog.

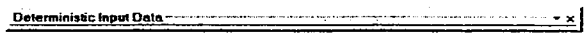

2. It can be left up on the screen while performing other tasks. When not needed, it can be "rolled-up" and dragged out of the way (for example, the top of the screen) with the LEFT mouse button.

3. If multiple files are open, the Input Data dialog will always display the data in the active file.

You may find these properties of the Input Data dialog useful, for example, when performing parametric analysis, or when working with multiple files.

Stereo Projection of Input Data Planes

To view a stereographic projection of your SWEDGE Input Data planes, select the Stereonet button in the toolbar. The great circles on the stereonet are identified by labels – 1, 2, TC, US, and FS – to indicate failure planes 1 and 2, the tension crack plane, and the upper and face slope planes.

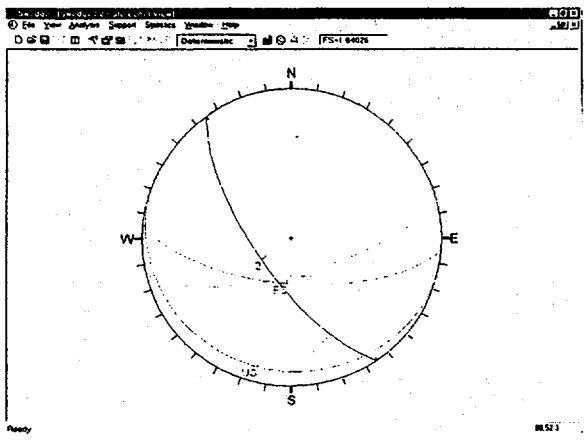

Figure 2-6: Stereonet projection of SWEDGE input data planes.

Importing Data from a DIPS File

The planes forming the wedge geometry can also be read into SWEDGE from a DIPS planes file (".dwp" filename extension), with the Import option in the File menu.

DIPS is a program for the graphical and statistical analysis of structural geology data using spherical projection techniques. Visit the Rocscience website at www.rocscience.com for more information.

Info Viewer

Before we conclude this "quick tour", let's examine the Info Viewer option.

Select: Analysis → Info Viewer

A convenient summary of model and analysis parameters is displayed in its own view. Scroll down to view all of the information. This can be printed if desired.

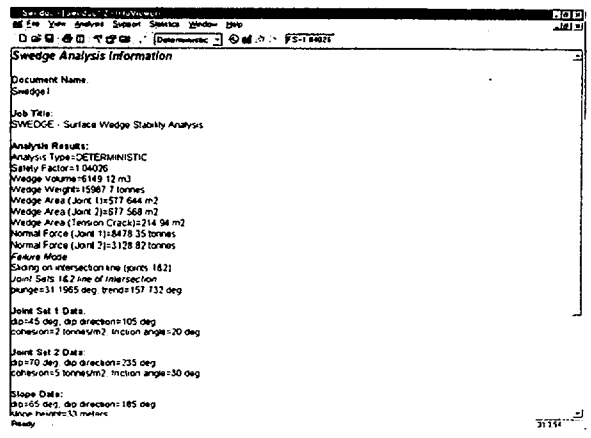

Figure 2-7: Info Viewer listing.

That concludes this "quick tour" of SWEDGE. To exit the program:

Select: File → Exit

Probabilistic Analysis

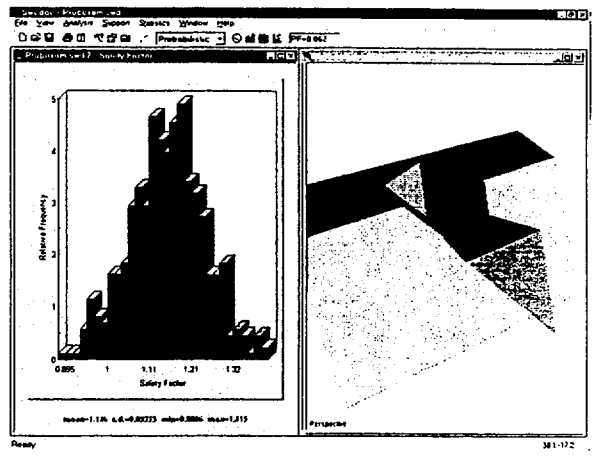

This tutorial will familiarize the user with the Probabilistic analysis features of SWEDGE.

If you have not already done so, run SWEDGE by double-clicking on the SWEDGE icon in your installation folder. Or from the Start menu, select Programs → Rocscience → Swedge → Swedge.

If the SWEDGE application window is not already maximized, maximize it now, so that the full screen is available for viewing the model.

To begin creating a new model:

Select: File → New

A default wedge model will immediately appear on your screen. Whenever a new file is opened, the default input data will form a valid wedge.

Job Control

Job Control allows the user to enter a Job Title, and select a Unit System and Analysis Type. Let's switch the Analysis Type to Probabilistic.

Select: Analysis → Job Control

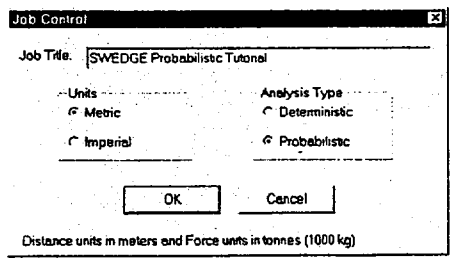

Enter "SWEDGE Probabilistic Tutorial" as the Job Title. Leave Units = Metric and change the Analysis Type to Probabilistic. Select OK.

Note:

Analysis Type can be selected from the drop-down list box in the toolbar.

- Analysis Type can also be changed at any time, using the drop-down list box in the middle of the SWEDGE toolbar. This is a convenient shortcut.

- The Job Title will appear in the Info Viewer listing, discussed later in this tutorial.

- Units determines the length and force units used in the Input Data dialog and the analysis.

Probabilistic Input Data

Now let's look at the input data.

Select: Analysis → Input Data

You should see the Probabilistic Input Data dialog shown below.

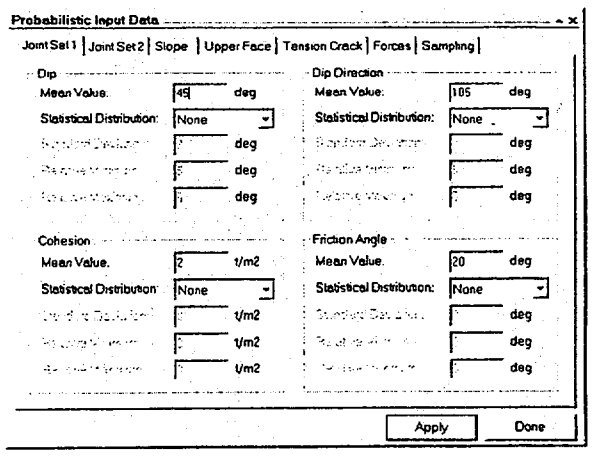

Defining Random Variables

To define a random variable in SWEDGE:

1. First select a Statistical Distribution for the variable. (In most cases a Normal distribution will be adequate.)

2. Enter Standard Deviation, Minimum and Maximum values. NOTE that the Minimum / Maximum values are specified as RELATIVE distances from the mean, rather than absolute values.

Minimum / Maximum values are specified as RELATIVE distances from the mean

3. Any variable for which the Statistical Distribution = "None" will be assumed to be "exactly" known, and will not be involved in the statistical sampling.

See the Introduction for information about the properties of the statistical distributions available in SWEDGE.

For this example, we will use the default Mean Input Data, and define Normal Statistical Distributions for the following variables:

- Joint Set 1 Dip and Dip Direction
- Joint Set 1 Cohesion and Friction Angle
- Joint Set 2 Dip and Dip Direction
- Joint Set 2 Cohesion and Friction Angle
- Tension Crack Dip and Dip Direction

Joint Set 1

Make sure the Joint Set 1 tab is selected in the Input Data dialog, and enter the following data:

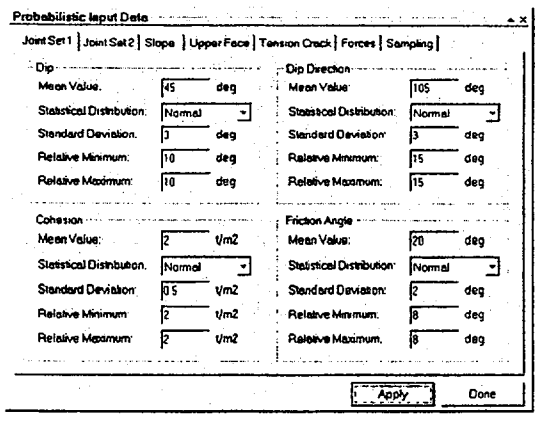

Joint Set 2

Select the Joint Set 2 tab and enter the following data:

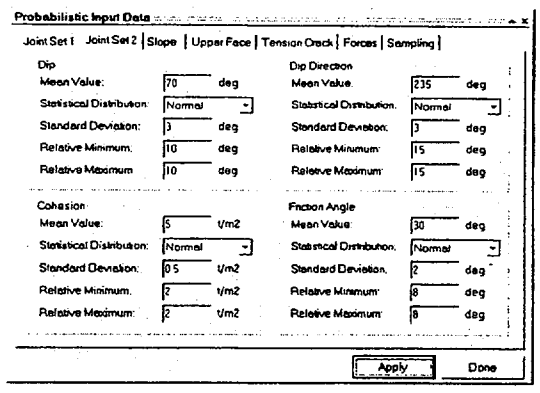

Tension Crack

Select the Tension Crack tab and enter the following data:

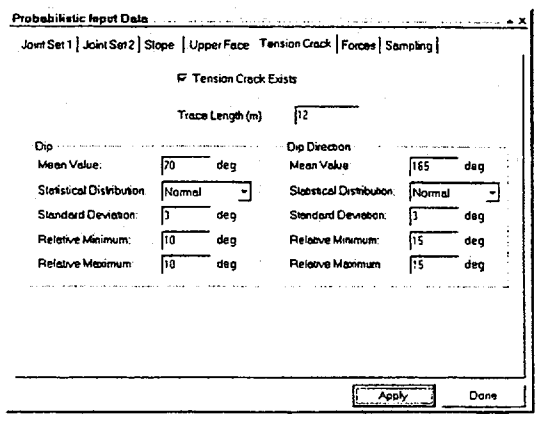

Slope

We will assume that the orientation of the slope planes is exactly known, so we will not enter statistical data for the upper slope or face slope orientations (ie. Statistical Distribution = None for these variables).

Forces

We will not be using the Forces options in this tutorial. See the Quick Start Tutorial for a discussion of Forces in SWEDGE.

Sampling

We will use the default Sampling Method and Number of Samples (ie. Monte Carlo method, 1000 samples).

Probabilistic Analysis

To carry out the SWEDGE Probabilistic Analysis:

- *Select the Apply button in the Input Data dialog.*

The analysis will be run using the parameters you have just entered. Calculation should only take a few seconds. The progress of the calculation is indicated in the status bar.

Close the dialog by selecting the Done button.

Results

Probability of Failure

The primary result of interest from a Probabilistic Analysis is the Probability of Failure. This is displayed in the toolbar at the top of the screen.

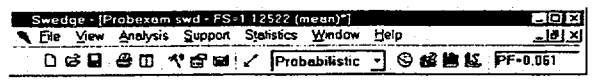

For this example, if you entered the Input Data correctly, you should obtain a Probability of Failure of around 6%. (eg. PF = 0.061 means 6.1% Probability of Failure).

However, remember that the sampling of the Input Data is based on the generation of random numbers by the Monte Carlo analysis. *Therefore the Probability of Failure will not necessarily be the same each time you compute with the same data.*

See the section on Re-running the Analysis later in this tutorial, for a demonstration.

Wedge Display

The wedge initially displayed after a Probabilistic Analysis, is based on the mean input values. Therefore, the wedge will appear exactly the same as one based on Deterministic Input Data with the same orientation as the mean Probabilistic Input Data.

However, other wedges generated from the Probabilistic Analysis can be displayed as described below.

Histograms

To plot histograms of results after a Probabilistic Analysis:

Select: Statistics → Plot Histogram

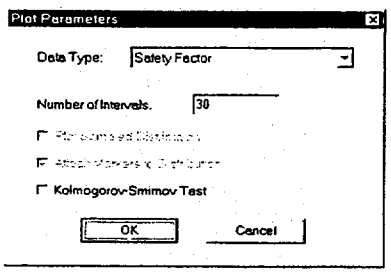

Select OK to plot a histogram of Safety Factor.

The histogram represents the distribution of Safety Factor, for all valid wedges generated by the Monte Carlo sampling of the Input Data. The red bars at the left of the distribution represent wedges with Safety Factor less than 1.0.

*The **mean** Safety Factor is not necessarily the same as the Deterministic Safety Factor based on the mean Input Data values.*

Mean Safety Factor

Notice the mean, standard deviation, min and max values displayed below the histogram.

Keep in mind that the **mean** Safety Factor from a Probabilistic Analysis is not necessarily the same as the Deterministic Safety Factor based on the mean Input Data values. In general, these two values will not be equal to each other.

Manipulating the Histogram View

1. If you right-click on a histogram and select 3D Histogram, you can apply a 3D effect.

2. If you click and HOLD the LEFT mouse button on the histogram and move the mouse, you can change the "viewing angle" of the 3-D histogram.

3. To restore the default viewing angle of a 3D Histogram, right-click and select Reset View.

Viewing Other Wedges

Let's now tile the Histogram and Wedge views, so that both are visible.

Select: Window → Tile Vertically

A useful property of the Histogram view is the following:

- If you double-click the LEFT mouse button anywhere on the histogram, the nearest corresponding wedge will be displayed in the Wedge view.

For example:

1. Double-click on the histogram at approximately Safety Factor = 1.

2. Notice that a different wedge is now displayed.

3. The actual Safety Factor of this wedge is displayed in the title bar of the Wedge view. It will probably not be exactly = 1, since it depends on exactly where you clicked, and the actual safety factor of the nearest wedge.

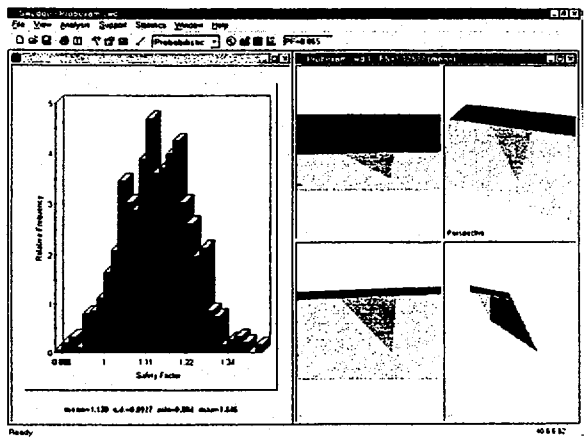

Figure 3-1: Safety Factor histogram and wedge view.

In any case, this feature is meant to give you a general idea of the shape and orientation of wedges corresponding to locations along the histogram. For example, you will probably want to double-click in the "red" Safety Factor region, to see the wedges with a Safety Factor < 1.

To reset the Wedge view so that the mean wedge is displayed:

Select: View → Reset Wedge

This will display the wedge corresponding to the mean Probabilistic Input Data.

Histograms of Other Data

In addition to Safety Factor, you may also plot histograms of:

- Wedge Weight
- Plunge or Trend of Line of Intersection of Joint Sets 1 and 2
- Any random variable (ie. any Input Data variable which was assigned a Statistical Distribution)

For example:

Select: Statistics → Plot Histogram

In the dialog, set the Data Type = Wedge Weight, and select OK.

A histogram of the Wedge Weight distribution will be generated.

Note that all of the features described above for the Safety Factor histogram, apply to any other Data Type. For example, if you double-click on the Wedge Weight histogram, the nearest corresponding wedge will be displayed in the Wedge View.

Let's generate one more histogram.

Select: Statistics → Plot Histogram

This time we will plot one of our Input Data random variables. Set the Data Type = Dip of Joint 1. Check the Plot Sampled Distribution checkbox. Select OK.

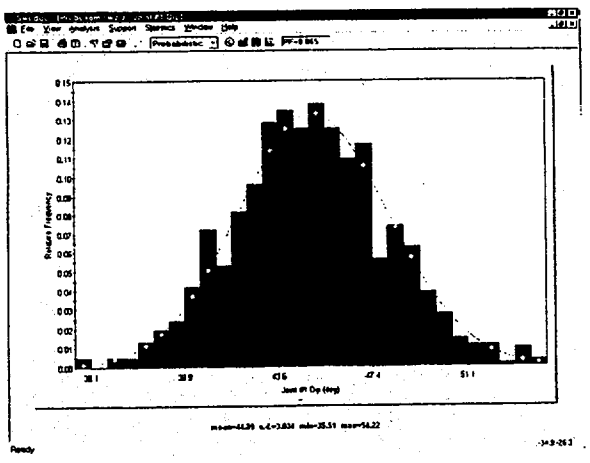

Figure 3-2: Joint 1 Dip Angle – Monte Carlo sampling of normal distribution.

The histogram shows how the Dip of Joint 1 Input Data variable was sampled by the Monte Carlo analysis. The curve superimposed over the histogram is the Normal distribution you defined when you entered the mean, standard deviation, min and max values for Dip of Joint 1 in the Input Data dialog.

Re-running the Analysis

The Probabilistic Analysis can be re-run at any time, by selecting the Compute button in the toolbar.

In general, the Probability of Failure will be different each time the analysis is re-run.

Let's demonstrate this, but first let's tile the views again. If you have not closed any views, you should still have on your screen:

- The Wedge View and
- The Safety Factor, Wedge Weight, and Joint 1 Dip Angle Histograms.

If you closed any of the histograms, re-generate them as described above. Now tile the four views.

Select: Window → Tile Vertically

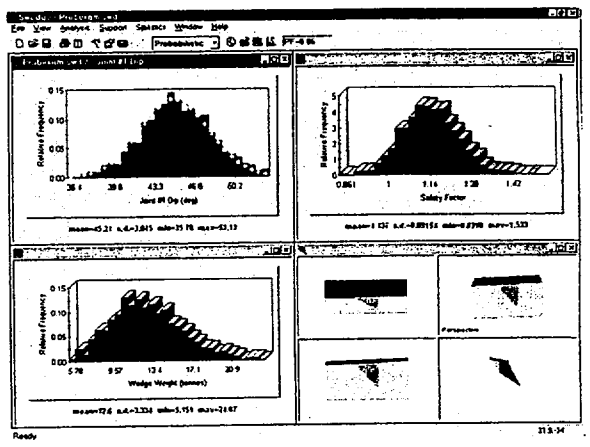

Figure 3-3: Tiled histogram and wedge views.

Now select the Compute button in the SWEDGE toolbar.

Select: Analysis → Compute

Notice that the Histograms and Probability of Failure are updated with the new analysis results.

Now continue to select Compute several times, and observe the variation in the Histograms and the Probability of Failure. This graphically demonstrates the SWEDGE Monte Carlo analysis.

Note that the Wedge view does not change when you re-compute, since the default wedge displayed is based on the mean Input Data, which is not affected by re-running the analysis.

For this example, if you re-run the analysis several times, you will find that the Probability of Failure will vary between about 4 and 8%.

Cumulative Distributions (S-curves)

In addition to the histograms, cumulative distributions (S-curves) of the statistical results can also be plotted.

Select: Statistics → Plot Cumulative

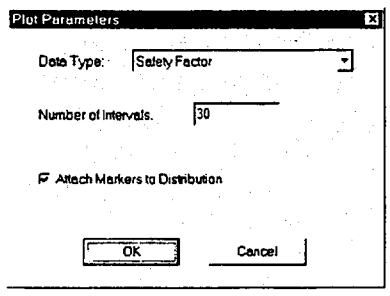

Select OK.

The cumulative Safety Factor distribution will be generated, as shown in Figure 3-4.

Notice the vertical dotted line visible on the plot. This is the Sampler, and allows you to obtain the coordinates of any point on the cumulative distribution curve.

- To use the sampler, just SINGLE click the LEFT mouse button anywhere on the plot, and the sampler will jump to that location, and display the results.

- Alternatively, press and HOLD the LEFT mouse button on the plot, and you will see the double-arrow icon. Move the mouse left or right, and the sampler will continuously display the values of points along the curve.

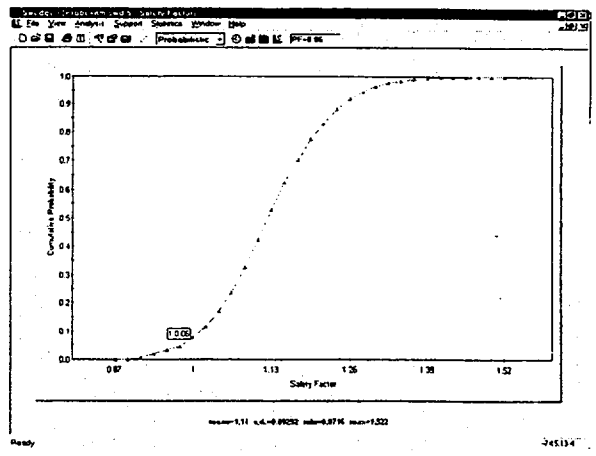

Figure 3-4: Cumulative safety factor distribution.

The display of the Sampler can be turned on or off in the right-click menu or the Statistics menu.

Now tile the views one more time, and re-compute the analysis.

Select: Window → Tile Vertically

Select: Analysis → Compute

Notice that the cumulative distribution gets updated along with the histograms, each time the analysis is re-run.

Info Viewer

Let's examine the Info Viewer listing for a Probabilistic Analysis.

Select: Analysis → Info Viewer

A convenient summary of model and analysis parameters is displayed in its own view. Scroll down to view all of the information. This can be printed if desired.

Notice the summary of Valid, Failed and Safe Wedges. Depending on your geometry input, it is possible for the Probabilistic Sampling of the Input Data to generate invalid wedge geometries. In general:

Number of Failed Wedges +
Number of Safe Wedges =
Number of Valid Wedges

Number of Samples –
Number of Valid Wedges =
Number of Invalid Wedges

As with the Histograms and S-curves, if you re-compute the analysis, the Info Viewer listing is automatically updated to reflect the latest results.

Current Wedge Data

Notice the Current Wedge Data listing in the Info Viewer. By default, the mean wedge data is displayed after a Probabilistic analysis.

Remember we pointed out earlier that if you double-click on a Histogram, the nearest wedge will be displayed in the Wedge View. The Current Wedge Data will also be updated, to reflect the data for the "picked" wedge. Let's demonstrate this.

1. Close (or minimize) all views you may have on the screen, EXCEPT the Info Viewer and the Safety Factor Histogram.

2. Select the Tile Vertically toolbar button.

3. If necessary, scroll down in the Info Viewer view, so that the Current Wedge Data is visible.

4. Double-click at different points on the Safety Factor histogram, and notice that the Current Wedge Data is updated to show the data for the "picked" wedge.

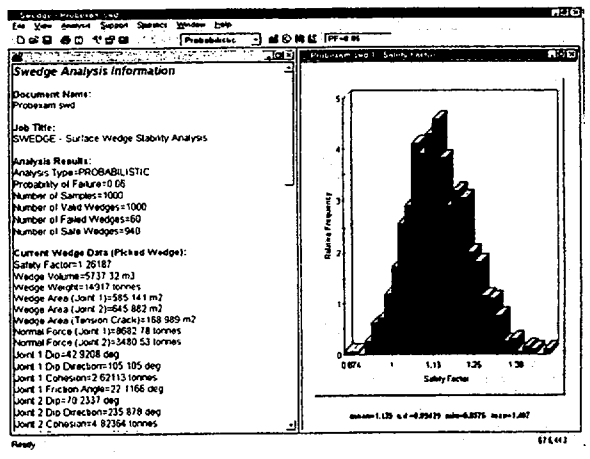

Figure 3-5: Current Wedge Data for Picked Wedge.

5. To reset the Current Wedge Data to the mean data:

Select: View → Reset Wedge

Sampling Method

As a final exercise, set the Sampling Method to Latin Hypercube, and re-run the analysis.

Select: Analysis → Input Data

In the Input Data dialog, select the Sampling tab, and set the Sampling Method to Latin Hypercube. Select the Apply button.

Examine the Probability of Failure, and the Safety Factor Histogram. The results should be very similar to the Monte Carlo analysis.

The difference is in the sampling of the Input Data random variables. For example, generate a Histogram of Joint Set 1 Dip Angle.

Select: Statistics → Plot Histogram

Set the Data Type = Dip of Joint 1. Select the Plot Sampled Distribution checkbox. Select OK.

Now compare the histogram with Figure 3-2. The Latin Hypercube sampling method results in a much smoother sampling of the Input Data distribution, compared to the Monte Carlo method.

Adding Support

Rock bolts are added to an SWEDGE model with the Add Bolt option. This allows the user to evaluate the number, location, length and capacity of bolts necessary to stabilize a wedge (ie. increase the Safety Factor to a required amount).

Let's start with a new (Deterministic) file for the purposes of the following demonstration.

Select: File → New

To add a rock bolt:

Select: Support → Add Bolt

1. Move the cursor into the Top or Front orthogonal views.
2. Notice that the cursor changes to an "arrow / rockbolt" icon.
3. As you move the cursor over the wedge, notice that the "rockbolt" and "arrow" now line up – this indicates that you may add the bolt to the wedge.
4. Click the LEFT mouse button at a point on the wedge where you want the bolt installed.
5. The bolt will be installed NORMAL to the face of the wedge on which you clicked (ie. normal to the Upper or Face slope), however you can modify the orientation using the Bolt Properties dialog which you will see in the middle of the screen.

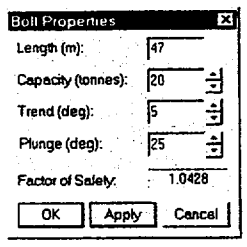

6. The Bolt Properties dialog works as follows:

   - If you modify the Capacity, Trend or Plunge with the "arrow" buttons at the right of the dialog, *the Safety Factor is immediately recalculated and displayed in the dialog as the values are being changed.* This allows the user to interactively modify the bolt properties, and immediately see the effect on the Safety Factor.

   - Alternatively, values can be typed in to the dialog. *In this case, the Safety Factor is NOT automatically re-calculated, the user must select the Apply button to apply typed in values.*

   - As the bolt Trend and Plunge are changed, you will see the orientation of the bolt updated on the screen.

   - Changing the Length of the bolt will be visible on the model, but has NO effect on the Safety Factor – see the next section for details.

7. When the bolt orientation, length and capacity are satisfactory, select OK, and the bolt will be added to the model.

8. If you are not happy with the location of the bolt, select Cancel, and the bolt will be deleted.

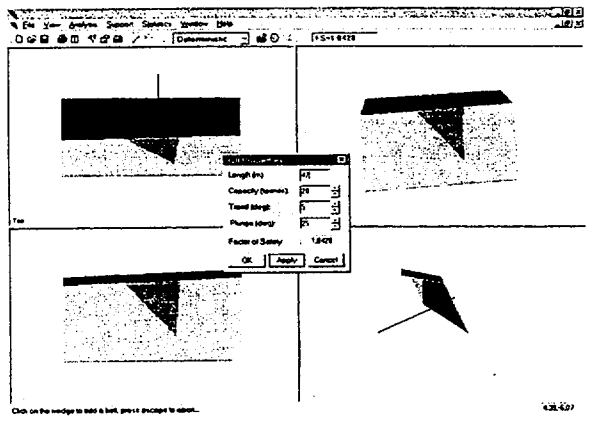

Figure 4-1: Adding a bolt.

Note:

- The Right orthogonal view can also be used for adding bolts, however this is not recommended, as correct placement may be difficult or impossible. (If the Dip Directions of the Upper and Face Slope are the same it will NOT be possible to add a bolt in the Right orthogonal view.)

- Bolts can NOT be added in the Perspective view.

How Bolts are Implemented in SWEDGE

Bolts are implemented in the SWEDGE stability analysis as follows:

Capacity and Orientation

1. Bolts affect the Safety Factor through their Capacity and Orientation (Trend / Plunge) only.

2. Bolt capacities and orientations are added vectorially, and are included in the Safety Factor calculation as a single, equivalent force passing through the centroid of the wedge.

3. Multiple bolts with the same orientation can therefore be simulated by a single bolt having the same total capacity.

Length and Location

1. Bolt Length and Location (on the face of the wedge) have NO effect on the Safety Factor.

2. The Length and Location of bolts allows the user to visualize the practical problems of installing the bolts.

3. Even bolts which do not pass through the wedge, will affect the Safety Factor (ie. SWEDGE does NOT check for valid bolt lengths). So do NOT assume that "short" bolts will be filtered out – they will have exactly the same effect as longer bolts with the same capacity and orientation.

Bolts vs. External Force

1. A bolt is therefore exactly equivalent to adding an External Force with the same magnitude and orientation. (See the Quick Start Tutorial for an example of adding an External Force).

2. It is left as an exercise for the user to verify that a bolt, and an equivalent External Force, result in the same Safety Factor.

Multiple Bolts

Any number of bolts can be added to a model, by repeating the steps outlined above.

However, remember that bolts in SWEDGE simply behave as force vectors passing through the centroid of the wedge. The applied force is equal to the bolt capacity.

Therefore, in terms of the effect on the Safety Factor, multiple bolts can be simulated by:

- a fewer number of bolts, or even a single bolt, with equivalent capacity and direction,

- or an equivalent External Force.

Installation of multiple bolts is useful for visualizing the practical problems of bolt installation, and the necessary bolt lengths and spacing. Or for back-calculating the Safety Factor of an existing wedge support system.

Deleting Bolts

To delete bolts:

Select: Support → Delete Bolt

Bolts can be deleted in the Top, Front or Right views as follows (bolts cannot be deleted in the Perspective view):

1. Move the cursor in the Top, Front or Right views.
2. The cursor will change to a small "box".
3. Hover the cursor over a bolt that you wish to delete.
4. The bolt will change colour, to indicate that it is "selected".
5. When the correct bolt is selected, click the LEFT mouse button, and the bolt will be deleted.
6. A new Safety Factor will immediately be calculated.
7. Repeat steps 3 to 5 to continue deleting bolts.
8. Press Escape to exit the Delete Bolts option.

To delete ALL bolts at once:

Select: Support → Delete Bolt

1. Enter the asterisk (*) character on the keyboard.
2. ALL bolts will be deleted from the model.

Note that the bolt colour and the "selected" bolt colour, can be modified in the View → Display Options dialog, if necessary, for easier viewing.

Editing Bolts

To edit the properties of a bolt:

Select: Support → Edit Bolt

Bolts are selected for editing in the same manner as for deleting – see the previous page for instructions.

Once a bolt has been selected for editing:

1. You will see the Bolt Properties dialog in the middle of the screen, displaying the properties of the bolt.
2. You can modify the Capacity, Trend, Plunge or Length of the bolt, in the same manner as when you originally added the bolt. See the previous pages for details.
3. When you are finished editing the properties, select OK to save your changes.
4. If you select Cancel, all changes will be cancelled, even if you used the Apply button to apply the changes.

Bolts can only be edited one at a time in this manner. It is not possible to edit the properties of multiple bolts simultaneously.

Listing of Bolt Properties

A listing of all bolts and their properties (Capacity, Length, Trend and Plunge) can be found in the Info Viewer listing.

The Info Viewer option is available in the Analysis menu, and in the toolbar.

Bolts in a Probabilistic Analysis

The above discussion of bolts in SWEDGE assumes a Deterministic Analysis of a single wedge.

If the Analysis Type is PROBABILISTIC:

- the Probabilistic Analysis will be run EACH time a bolt is added or edited (ie. when OK is selected on the Bolt Properties dialog).
- Selecting Apply in the Bolt Properties dialog will calculate a new Safety Factor for the MEAN wedge, but will NOT run the Probabilistic Analysis.
- If you are deleting bolts, the Safety Factor for the MEAN wedge will be re-calculated as each bolt is deleted, but the Probabilistic Analysis will only be run when you exit the Delete Bolts option.

NOTE:

Bolts should be used with some caution in a Probabilistic Analysis if your random variables include the orientation of the planes forming the wedge.

Since the bolts are added while viewing the mean wedge, the orientations of bolts added on the mean wedge may no longer be appropriate in terms of support to wedges of other orientations generated by the Probabilistic Analysis.

If the only random variables in the Probabilistic Analysis are the strength parameters (cohesion and friction angle) of the failure planes, then this will not be an issue, since the wedge geometry will remain constant.

REPORT NO.
UCB/EERC-94/05
MAY 1994

EARTHQUAKE ENGINEERING RESEARCH CENTER

SEISMIC RESPONSE OF STEEP NATURAL SLOPES

by

SCOTT A. ASHFORD
NICHOLAS SITAR

Final report on research sponsored by
the United States Geological Survey
under USGS Award Number 14-08-0001-G2127

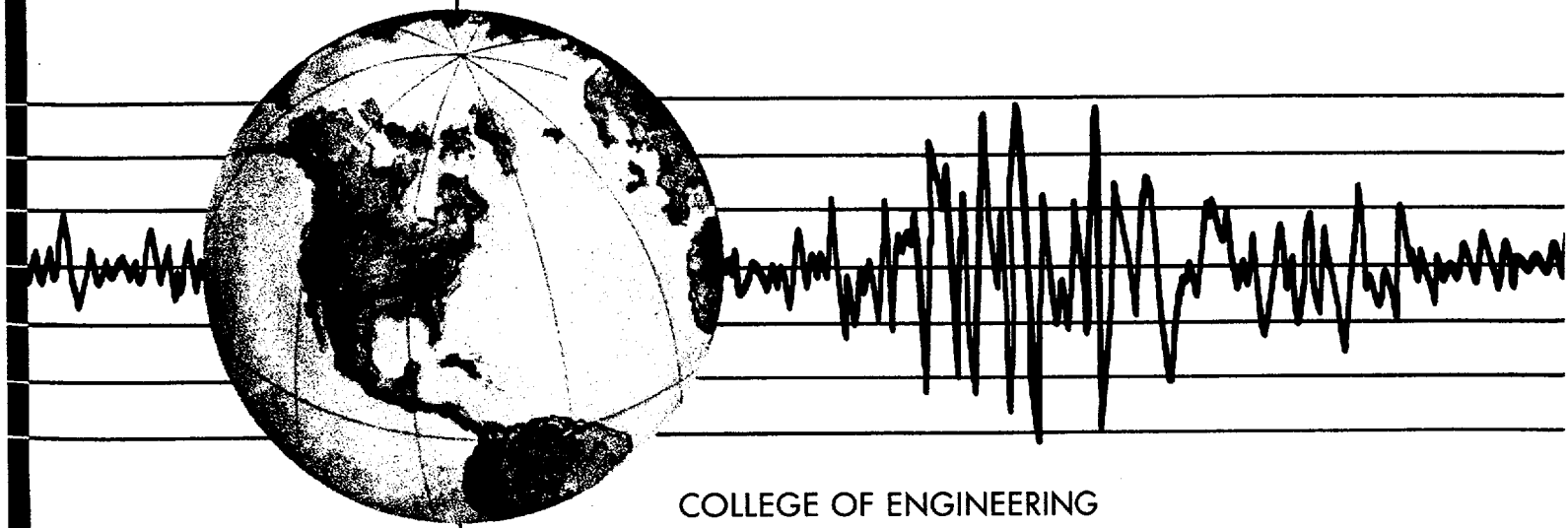

COLLEGE OF ENGINEERING

UNIVERSITY OF CALIFORNIA AT BERKELEY

For sale by the National Technical Information Service, U.S. Department of Commerce, Springfield, Virginia 22161

See back of report for up to date listing of EERC reports.

DISCLAIMER

EARTHQUAKE ENGINEERING RESEARCH CENTER

SEISMIC RESPONSE OF STEEP NATURAL SLOPES

by

Scott A. Ashford

Nicholas Sitar

Report No. UCB/EERC-94/05

Earthquake Engineering Research Center

College of Engineering

University of California at Berkeley

May 1994

Final report on research supported by the U.S. Geological Survey under USGS award number 14-08-0001-G2127. The views and conclusions contained in this document are those of the authors and should not be interpreted as necessarily representing the official policies, either expressed or implied, of the U.S. Government.

ABSTRACT

The results of a research program to evaluate the seismic response of steep slopes are presented. The impetus for this work was the October 17, 1989, Loma Prieta Earthquake which caused extensive landsliding along the coastal bluffs from San Francisco to Santa Cruz. While this research is specific to the bluffs in the San Francisco Bay region, the methods developed are generally applicable to stability analyses of steep, natural slopes.

A frequency domain parametric study on topographic effects, using the generalized hyperelement method, shows that the peak amplification of motion at the crest occurs at a normalized frequency $H/\lambda = 0.2$, where H is the slope height and λ is the wavelength of the motion. Amplification was found to increase with inclined waves traveling into the slope crest, and to decrease with inclined waves traveling away from the crest. More importantly, the natural frequency of the site behind the crest dominates the response, relative to the topographic effect.

The importance of the natural frequency is illustrated by the time domain response of 3 prototype sites using actual seismograms. The results show that the topographic amplification at the crest of a steep slope can be reasonably estimated by increasing the peak acceleration obtained from a one-dimensional site response analysis in the free field behind the crest by 50 percent. Then, for use in limit equilibrium slope stability analyses, the seismically induced force on a potential sliding mass can be estimated using profiles of the average seismic coefficient developed from the analytical results.

One of the objectives of the research was to develop practical analysis guidelines for evaluation of seismic response of steep slopes in weakly cemented natural deposits. A review of the laboratory behavior of weakly cemented sands shows that these materials exhibit brittle behavior under low confining stress, typical of a near-slope environment. This assessment of the behavior is supported by numerous field observations of seismically induced failures. Therefore, a limit equilibrium approach, rather than a deformation based analysis, is recommended.

ACKNOWLEDGMENTS

Professor John Lysmer made a significant contribution to this research effort in the area of two-dimensional seismic site response; his assistance is greatly appreciated. This research was sponsored by the United States Geological Survey under USGS award number 14-08-0001-G2127.

TABLE OF CONTENTS

Page

LIST OF TABLES

LIST OF FIGURES

Figure **Page**

1. INTRODUCTION

The results of a research program to evaluate the seismic response of steep slopes in weakly cemented granular soils are presented in this report. The main objective of the research program was to develop practical analysis guidelines for evaluation of seismic response of steep slopes in weakly cemented natural deposits. The impetus for this work has been the October 17, 1989, Loma Prieta Earthquake which caused extensive landsliding in the epicentral region and along the coastal bluffs from Seaside, south of Santa Cruz, to Daly City (Figure 1.1). While this research is specific to the coastal bluffs in the San Francisco Bay region, the methods developed are applicable to analysis of seismic response of similar marine terrace bluffs along the coast of Southern California, Oregon, and Washington, and should be generally applicable to stability analyses of steep, natural slopes.

The California coastline from Moss Landing northward to San Francisco is characterized by extensive stretches of steep coastal bluffs in marine terrace deposits, ranging from 20 to 200 meters in height. The appearance of the bluffs along this entire stretch of the coast shows evidence of active erosion, and there is abundant historical evidence of slope failures caused by earthquakes, wave erosion, and intense rainfall. Records indicate that seismically-induced slope failures along different portions of this coastline occurred during earthquakes in 1865 (Plant and Griggs, 1990), in 1906 (Lawson, 1908), in 1957 (Bonilla, 1957) and, most recently, during the Loma Prieta earthquake of October 17, 1989 (Plant and Griggs, 1990; Sitar, 1990).

No loss of property was recorded in 1865, probably due to very sparse

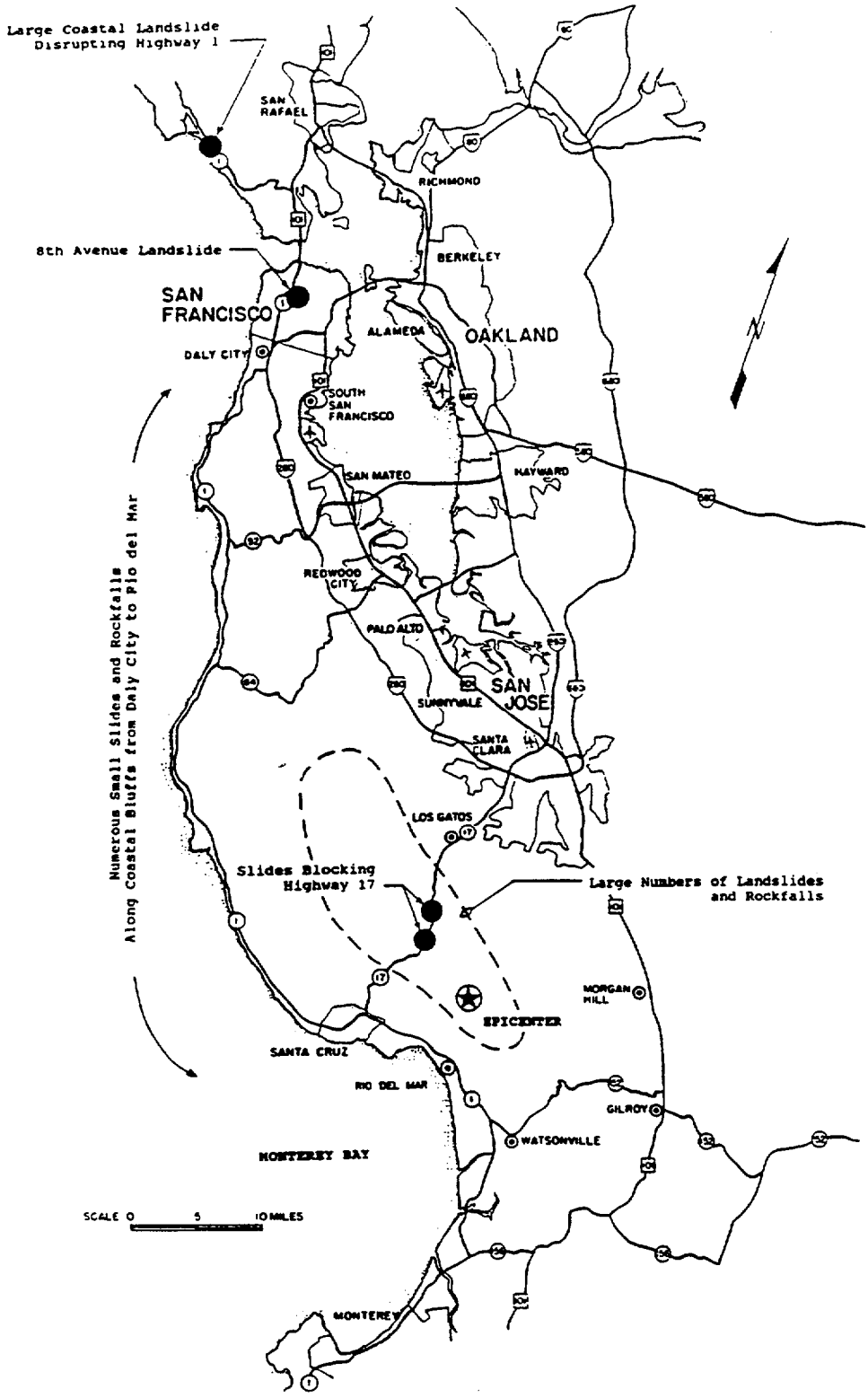

Figure 1.1: Distribution of landslides in the San Francisco area caused by the 1989 Loma Prieta Earthquake (from Seed et al., 1990).

population of the area. In 1906, extensive landsliding was observed, particularly along the bluffs in Daly City, where the railbed of the Ocean Shore Railroad was extensively damaged (Figure 1.2). In 1957, extensive landslides along the bluffs in Daly City blocked State Route 1 for about two weeks (Figure 1.3) and led to the eventual abandonment of the highway by the California Department of Transportation. Most importantly, while cracking was detected along the crest of the bluffs, there was no direct damage to dwellings because the bluff crests were still largely undeveloped. Since then the bluff crests along the coast have been extensively developed, particularly in Daly City, Pacifica, Half Moon Bay, Santa Cruz, Capitola, and Seaside. The risk posed by seismically-induced slope failures to these new developments was amply demonstrated by the October 17, 1989, Loma Prieta earthquake. Fortunately, the extent of damage was surprisingly minor considering the severity of other damage in the epicentral region and in San Francisco. Figure 1.4 shows a shallow failure of the bluffs at Pacifica, on the San Francisco peninsula. Similar slides at Rio Del Mar, south of Santa Cruz, were responsible for relatively minor damage to structures at toe of the slope; however, tensile cracking and loss of crest left many structures more vulnerable to future events. By far the largest failure occurred along the Daly City bluffs, some 55 miles from the epicenter (Figure 1.5). Cracking along the crest of the bluffs was also observed.

Thus, given the apparent potential for damaging landslides during earthquakes, there is a need to develop adequate understanding of the bluff response under seismic loading. Only then can rational procedures for stability evaluation of these slopes be developed.

Figure 1.2: Slope failures along the Ocean Shore Railroad north of Mussel Rock caused by the 1906 San Francisco Earthquake (courtesy of the Bancroft Library, U.C. Berkeley).

Figure 1.3: Landslides along bluffs in Daly City caused by the 1957 San Francisco Earthquake (courtesy of the California Department of Transportation).

Figure 1.4: Localized minor failures of marine terrace deposits in Pacifica caused by the 1989 Loma Prieta Earthquake.

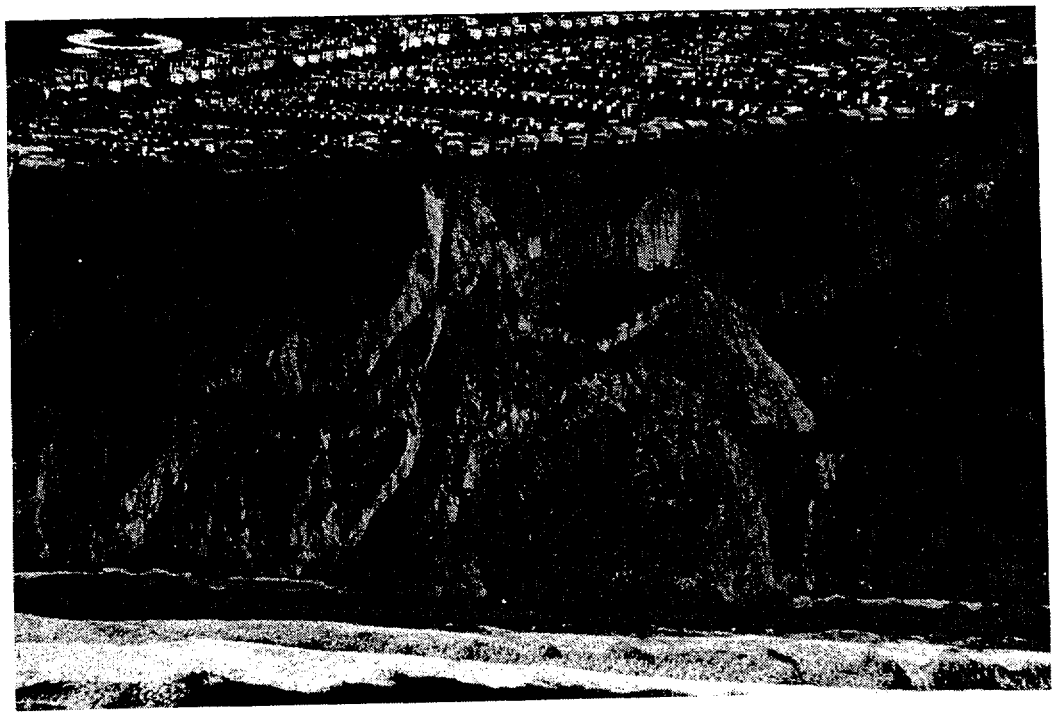

Figure 1.5: Failure of bluffs in Daly City caused by the 1989 Loma Prieta Earthquake.

This report begins with a review of the behavior of weakly cemented sands, both in the laboratory and in the field. The results of the review show that these materials exhibit brittle behavior under low confining stress, typical of a near-slope environment, and this behavior is confirmed by field observations of seismically induced failures. Since the stress conditions in the vicinity of the slope are an important aspect of a slope stability analysis, an evaluation of the accuracy of computed stress distributions using the finite element method is performed. This evaluation shows some of the limitations of a finite element method analysis in this case. The Generalized Hyperelement Method (Deng, 1991) is then presented for the analysis of the seismic response of these steep slopes.

The analysis of steep slopes to seismic loading begins with a frequency domain parametric study of a stepped halfspace and a stepped layer over a halfspace, in order to develop fundamental relationships between response, slope geometry, and material properties. Following this parametric study, the use and applicability of the "average seismic coefficient", originally developed for the seismic response analysis of embankments and dams, is evaluated. Seismic response characteristics of steep slopes in the time domain are then realistically examined using actual slope profiles, material properties, and seismograms. These results are used to develop a simplified methodology, similar to that presented by Makdisi and Seed (1978) to determine the equivalent seismic force induced by an earthquake on a steep slope. Finally, recommendations on the use of the results of this study in appropriate pseudo-static limit equilibrium stability analyses are presented.

2. BEHAVIOR OF WEAKLY CEMENTED SANDS

Weakly cemented granular deposits composed of various proportions of sand, gravel, and silt can be classified as either soft rock or hard soil, depending on the degree of compaction and the degree of cementation. Typical cementing agents include silica, calcium carbonate, clay, and iron. In addition, apparent cementation is achieved by mechanical interlocking of the soil grains or by capillary tension of pore water. Examples of such materials include marine terrace deposits along the Pacific coast of the United States, loess deposits in the mid-western United States and China, and volcanic ash deposits in Japan and Guatemala (Sitar 1990). Though examples of these materials are found around the world, the emphasis in this study is on the marine terrace deposits in the San Francisco Bay area, which are mainly composed of weakly cemented sands.

Nearly vertical natural slopes in weakly cemented sands have been observed in excess of 30 m in height, and slopes steeper than 30 degrees have been observed in excess of 150 m. In addition, the ability of these materials to stand in steep slopes has often been exploited to cut nearly vertical slopes for highways or roadways.

Under the low confining pressures encountered near slope faces, cemented sands exhibit brittle behavior and low tensile strength. As a result, tension cracks are typically observed behind the crests of the slopes, and the brittle behavior makes for spectacular and potentially devastating slope failures during dynamic, earthquake loading. As a preface to the study of the slope response, the following sections of

this chapter contain a review of the static and dynamic behavior of the material to the extent necessary for slope stability evaluation.

2.1 REVIEW OF STATIC PROPERTIES

The static behavior of weakly cemented soils has been the subject of numerous studies in the recent past (Clough et al. 1981, Haruyama 1973, Murata and Yamanouchi 1978, O'Rourke and Crespo 1988, Saxena and Lastrico 1978, and Wang 1986). One of the earliest studies devoted to cemented sands was performed by Saxena and Lastrico (1978) who tested the static stress-strain behavior of lightly naturally cemented sand with calcite as a cementing agent. They found that the cohesion caused by cementation was the predominant strength component at low strain levels (below 1 percent), and at high strain levels the frictional component of strength became predominant. They also found that very high confining stress could destroy the cementation.

Clough et al. (1981) reported on the results of over 100 tests on naturally and artificially cemented sand. They noted that cemented sand tends to behave in a brittle fashion, with brittleness increasing with cement content and decreasing with increasing confining pressure. The relationship between brittleness and confining pressure is apparent from Figure 2.1 which shows a set of typical stress-strain curves for an artificially cemented sand. At low confining pressures, the cementation tends to control behavior, making the material more brittle. As confining pressure increases, the ductility of the material also increases, as intergranular friction

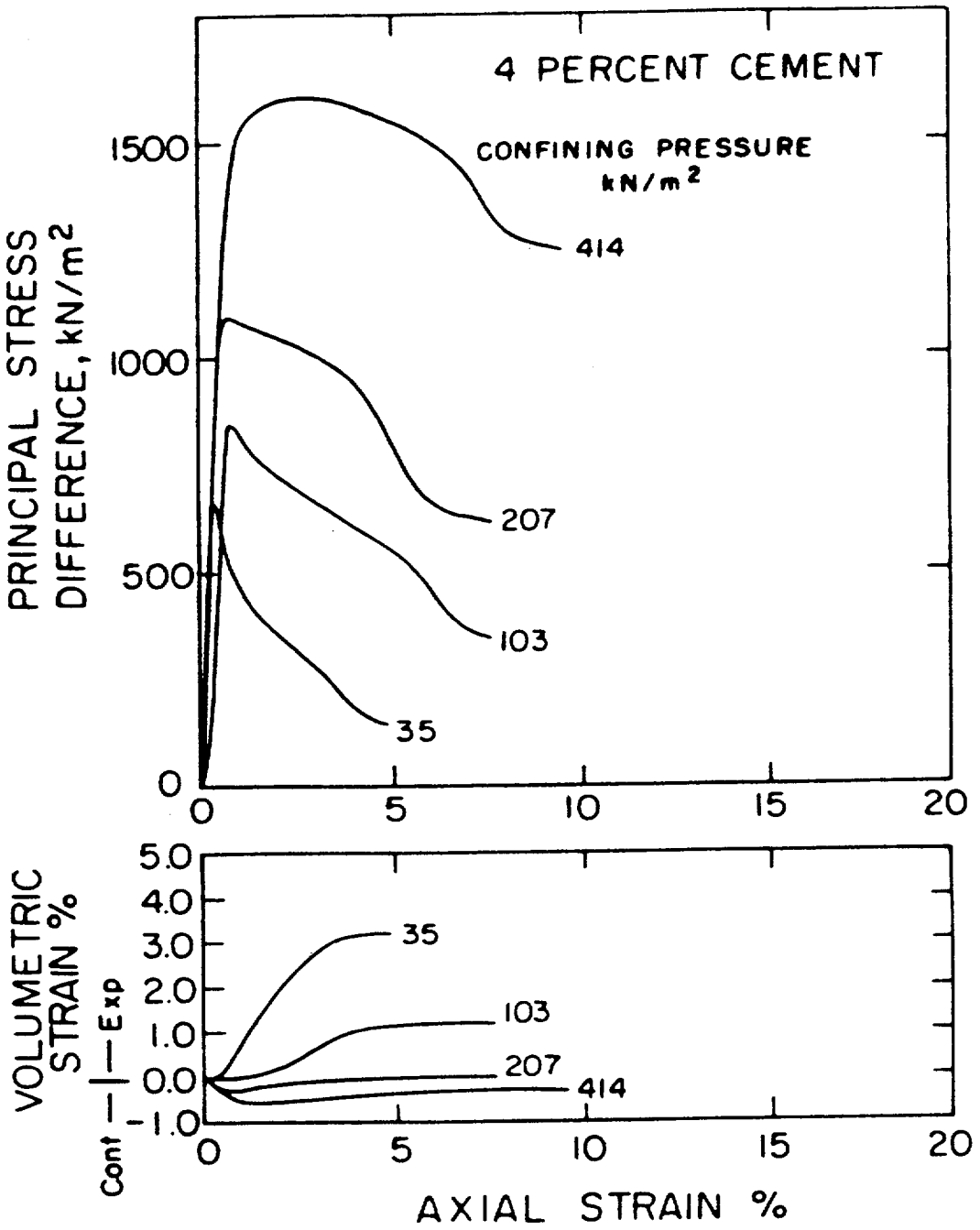

Figure 2.1: Typical stress-strain curves for artificially cemented sand (from Clough et al., 1981).

becomes more important. Also, the material exhibits nearly linear behavior until failure. Typical tensile strength, determined using the Brazilian tensile test, is on the order of 10 percent of the unconfined compressive strength. Thus, the failure envelope curves in the tensile region and gives a lower tensile strength than would be estimated using a straight-line extrapolation of the compression test results.

2.2 REVIEW OF DYNAMIC PROPERTIES

Fewer studies addressing the dynamic properties of cemented sands are available. Acar and El-Tahir (1986) studied the low strain dynamic properties of artificially cemented sands, while Frydman et al. (1980) and Clough et al. (1989) studied the effects of cementation on liquefaction. Studies that are most relevant to dynamic slope response in cemented sands were reported by Sitar and Clough (1983), Sitar (1990), and Wang (1986).

Wang (1986) conducted a comprehensive laboratory study on the dynamic behavior of cemented sand, consisting of over 80 dynamic tests on sands which were naturally and artificially cemented. He found that the shear modulus decreases and damping increases with increasing strain, as is the case with most soil during cyclic loading. Summary plots of shear modulus and damping ratio varying with shear strain are presented in Figures 2.2 and 2.3, respectively. A typical result of a cyclic simple shear test on cemented sand is shown in Figure 2.4. These results, together with results of cyclic triaxial tests, show that the stress-strain curve from static tests tend to provide an envelope for the hysteresis loops from the cyclic stress-strain test.

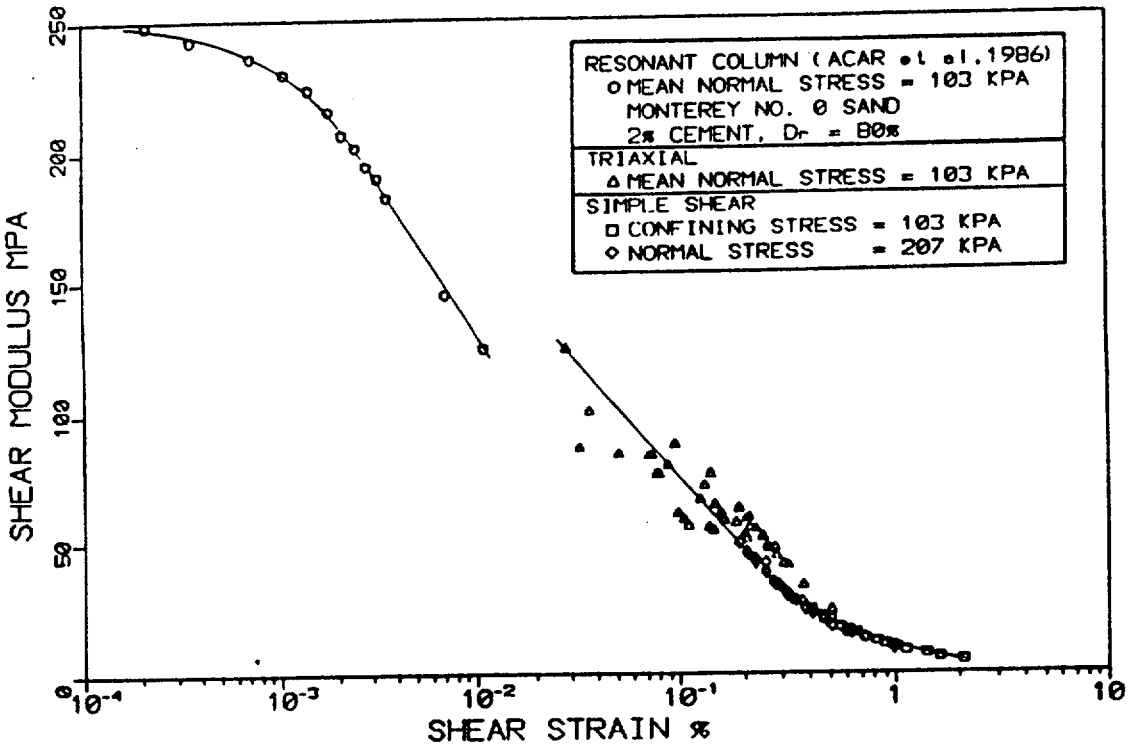

Figure 2.2: Summary plot of shear modulus versus shear strain for cemented sands (from Wang, 1986).

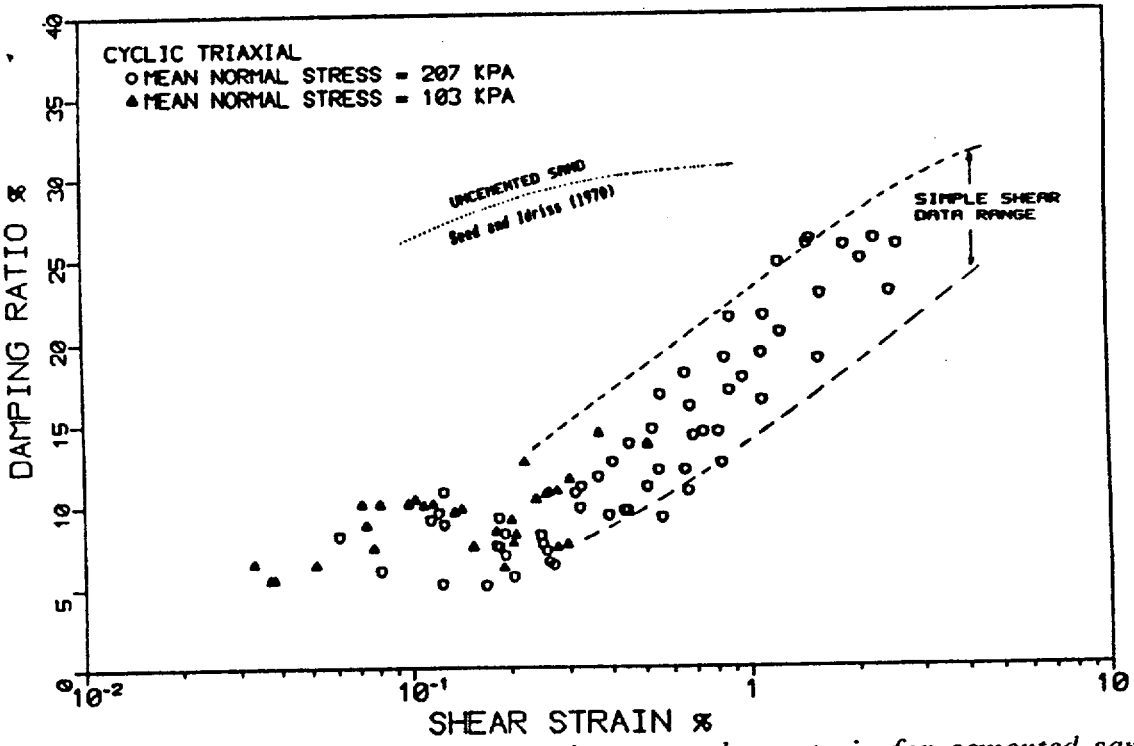

Figure 2.3: Summary plot of damping ratio versus shear strain for cemented sands (from Wang, 1986).

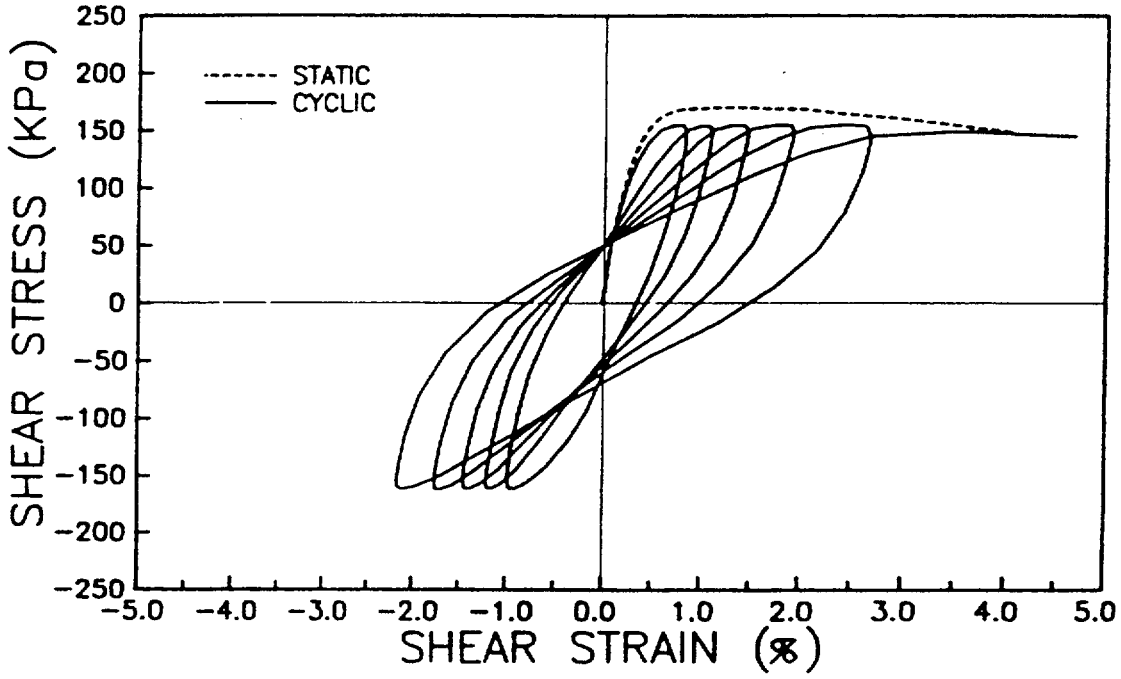

Figure 2.4: Typical static and cyclic stress-strain curves from simple shear tests on cemented sands (from Wang, 1986).

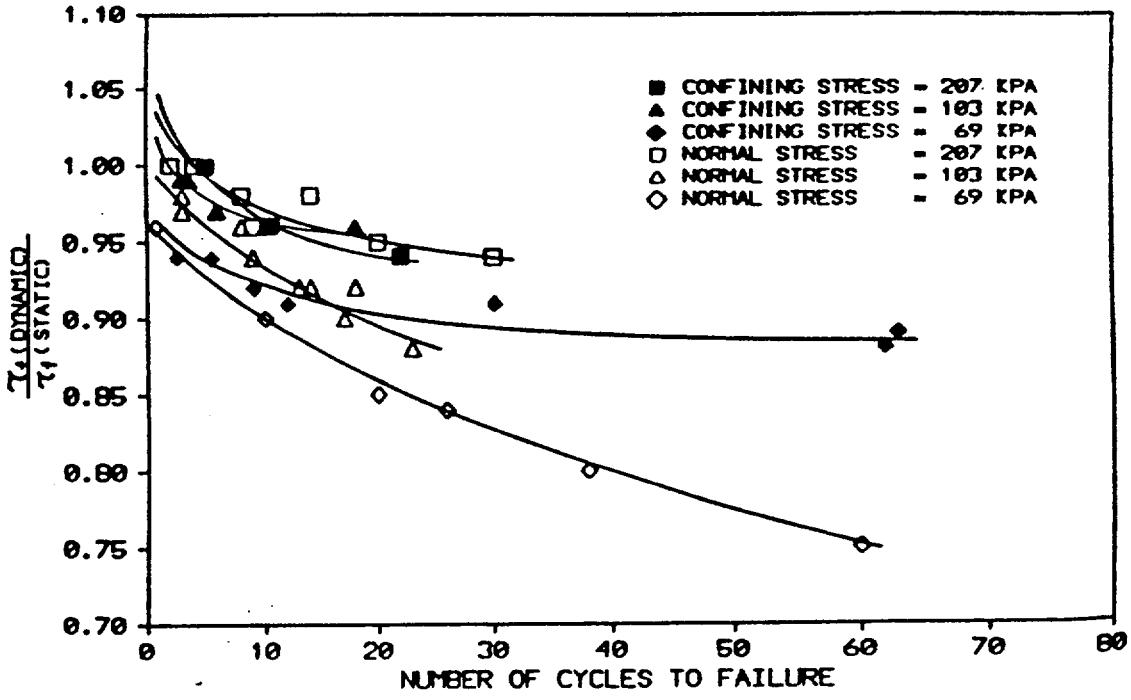

Figure 2.5: Dynamic strength envelopes for cemented sands under cyclic simple shear loading (from Wang, 1986).

Thus, Sitar (1990) has suggested that the large strain cyclic stress-strain behavior can be estimated from the results of static testing.

Figure 2.5 presents a plot of the ratio of static to cyclic simple shear strength with respect to the number of cycles to failure as a function of confining pressure (Sitar 1990). It is apparent that there is a trend for reduction in dynamic strength with increasing number of cycles. The effect is most pronounced at low confining pressures where the reduction can be as much as 15 percent. At higher confining pressures, the effect seems to be less than 10 percent.

2.3 OBSERVED SLOPE FAILURES IN WEAKLY CEMENTED SANDS

Failures of steep slopes in weakly cemented granular soils during seismic events have been recorded in many parts of the world. In California, in the San Francisco Bay region, landslides in coastal bluffs due to a seismic event were first recorded following an earthquake in 1865 (Plant and Griggs, 1990), though no property damage was reported. The first noted failures causing property damage occurred during the San Francisco Earthquake of 1906. "Rockfalls and dry sand flows were particularly disruptive" to highways and railroad grades (Youd and Hoose, 1978). Five kilometers of the Oceanshore Railway between Lake Merced and Mussel Rock were closed due to failure of coastal bluffs. In this area, large cracks were observed extending several hundred feet behind the slope crest (Lawson, 1908). These slopes are mostly in the Merced Formation which is primarily composed of uncemented and weakly cemented sand with interbedded clay layers. Further south,

near Capitola, slope failures were also observed in coastal bluffs in marine terrace deposits of weakly cemented sand (Youd and Hoose, 1978). However, due to the sparse population along the coast at the time, the available information is quite sketchy.

Numerous failures, which closed the coast highway, also occurred in the coastal bluffs between Lake Merced and Mussel Rock in the 1957 San Francisco Earthquake (Bonilla, 1959). The largest slide was several hundred feet wide and 700 feet from top to bottom along a 40 degree slope. The slide material appeared to be dry, and dust was observed rising from the slopes during failure. Cracks were also observed along the coast highway and behind the crests of the failed slopes.

The Loma Prieta Earthquake caused hundreds of failures in marine terrace deposits and coastal bluffs between Marin County and Big Sur (Sitar, 1990). This included a large slide in the bluffs in Daly City, near the site of earlier failures recorded in 1906 and 1957. Closer to the epicenter, slides were mapped all along the coast of Santa Cruz County by Plant and Griggs (1990). At Seacliff State Beach, many slides were observed occurring in the upper 12 m of the 30 m high cliffs. These slides were observed to be up to 60 m wide with tension cracks extending 1 to 6 m behind the crest. The slopes in this area are composed of up to 5 m of Quaternary marine terrace deposits, underlain by moderately indurated, weakly jointed sandstone member of the Purisima Formation. It is interesting to note that the types of failures, based on aerial photographs, appear similar to those which occurred during heavy rains in the winter of 1982.

More recently, failures in steep coastal bluffs occurred during the Petrolia Earthquakes of April 24 and 25, 1992. Failures in coastal bluffs composed of weakly cemented sand were observed at Centerville Beach, located approximately 6 km west of hard-hit Ferndale, California (Figure 2.6). These bluffs, consisting of Pliocene marine terrace deposits, are 10 to 50 m in height and slope angles range from 45° to nearly vertical. Strong motion instrumentation at the Oceanographic Naval Station, just behind the crest of the slope, indicated horizontal peak ground acceleration of 0.5g for the main shock (Shakal et al. 1992). The failures appeared to be relatively shallow and occurred in the upper portion of the slopes. Most of the material in the failure mass seemed to have lost its cementation, though several small intact blocks up to 1 m in diameter and larger were found (Figure 2.7). Three tension cracks were observed at 2 to 3 m intervals behind the crest of the 50 m slope to the west of the Naval Station. No other failures were observed in directly adjacent materials.

Most recently, slope failures occurred in the Pacific Palisades due to the January 17, 1994, Northridge Earthquake near Los Angeles California. These coastal bluffs are located approximately 30 km south of the epicenter of the $M_W = 6.7$ earthquake. Strong motion records at the nearby Santa Monica Fire Station indicate a peak horizontal acceleration of 0.93g and a peak vertical acceleration of 0.25g. The bluff failures closed the northbound lanes of the Pacific Coast Highway (State Route 1) for at least 4 days following the earthquake. Four large landslides were observed in this area, along with several smaller slides. One of the large slides carried a portion of a house down the slope, as shown in Figure 2.8. On properties

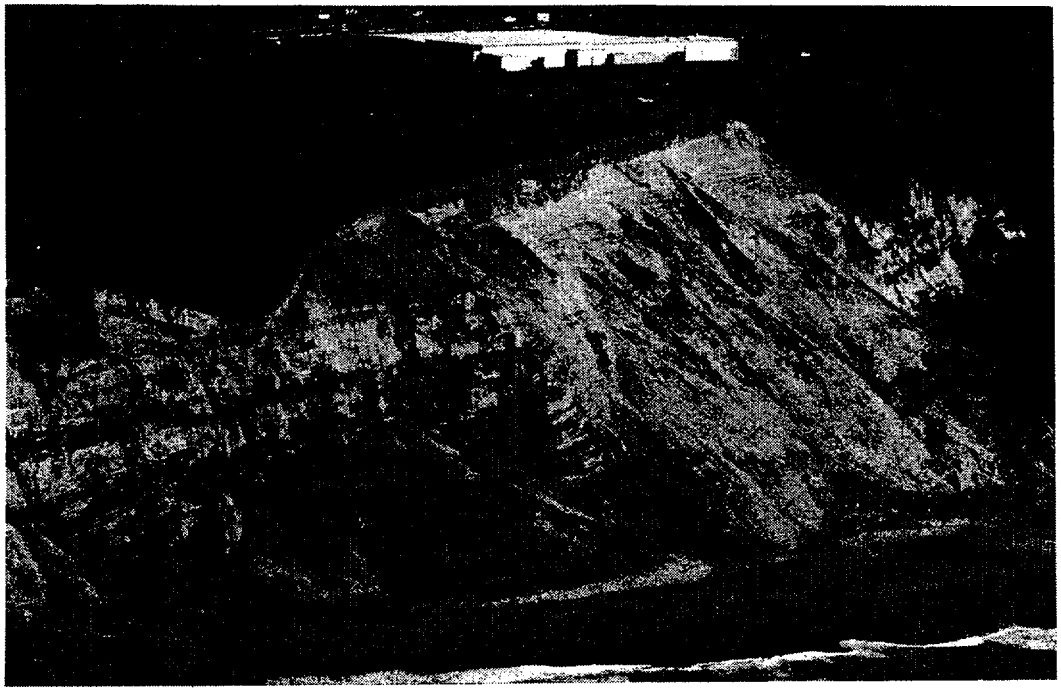

Figure 2.6: Landslides at Centerville Beach caused by the 1992 Petrolia Earthquake.

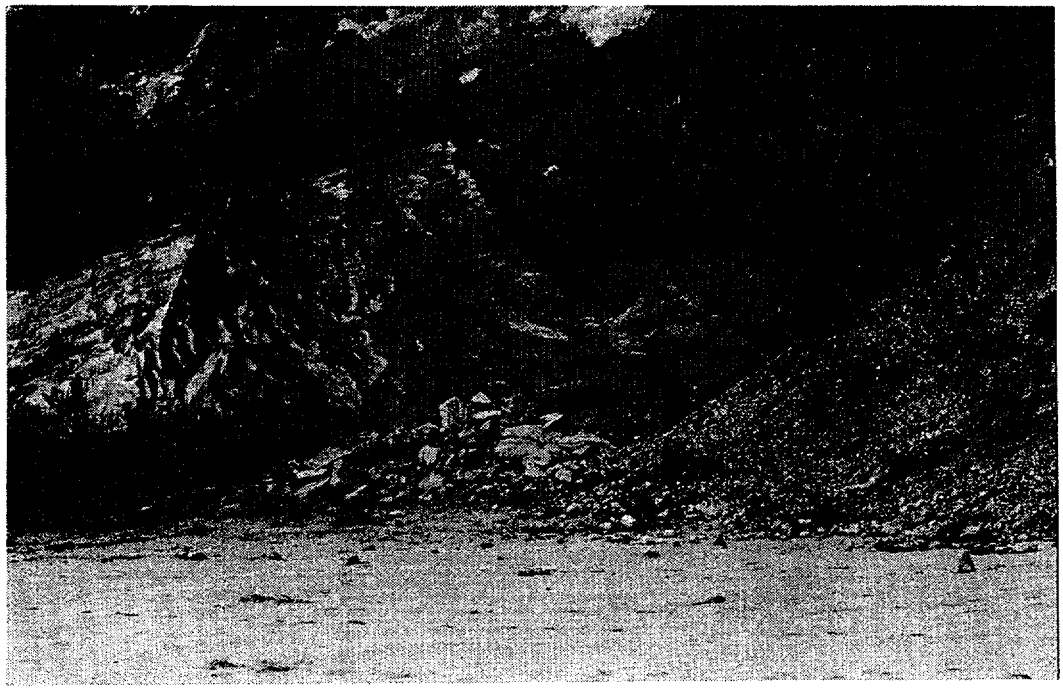

Figure 2.7: Intact blocks in landslide debris at Centerville Beach.

Figure 2.8: Landslide at Pacific Palisades caused by the 1994 Northridge Earthquake.

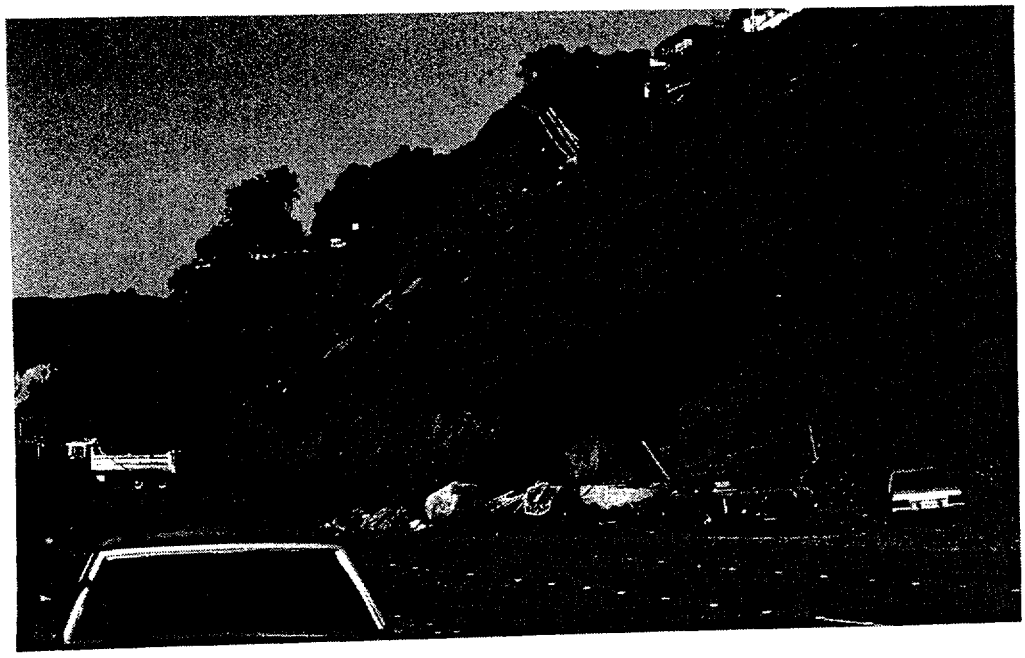

Figure 2.9: Intact blocks in slide debris at Pacific Palisades.

adjacent to this house, shallow concrete piers and H-piles were observed hanging in mid-air at the crest of the slope, implying that they provided little benefit. The failures occurred in Quaternary age deposits of weakly cemented sand (Jennings and Strand, 1969). The slopes on which the failures occurred were 40 to 60 m in height and moderately steep (between 45 and 60 degrees). The failure masses appeared to be only a few yards thick, subparallel to the slope, and had widths on the order of 100 m. The slide debris was predominately loose sand with a few intact blocks, as shown in Figure 2.9.

Failures of this type are not limited to California. Brittle, tensile failures of steep slopes in cemented volcanic ash deposits in Japan following the 1968 Ebino Earthquake were documented by Yamanouchi and Murata (1973) and Yamanouchi (1977). This material, called Shirasu, is a Pleistocene volcaniclastic deposit apparently cemented by welding, interlocking, or electro-static bonding. Again, similar types of failures were observed following heavy rains in 1949 and 1969.

Harp et al. (1978) documented slope failures in the February 4, 1976, Guatemala Earthquake. Landslides in Pleistocene pumice deposits blocked major highways and a railway, stalling relief efforts. This pumice has a very low tensile strength, but derives apparent cohesion from the mechanical interlocking of the angular particles. Nearly all failures occurred in steep-sided canyons. On slopes steeper than 50°, the pumice appeared to fail in tension by spalling off into nearly vertical slabs less than 6 m thick. Tension cracks were observed to extend 15 to 30 m back behind the up to 100 m high, nearly vertical slopes. On 30° to 50° slopes, debris slides less than 1 m thick were observed in sandy soil overlying the pumice.

Almost all individual slides were limited in size to less than 15,000 m^3. Harp noted that both types of failures were heavily concentrated on narrow ridges and spurs, and suggested that topography may have amplified the ground motions.

O'Rourke and Crespo (1988) described similar type of landslides in the Cangahua formation in Ecuador and southern Colombia. This volcaniclastic formation is characterized as a loess-like tephra with silica as a cementation agent. The material has the ability to stand in nearly vertical slopes up to 50 m high. An earthquake in 1987 closed the Pan-American Highway due to landslides in this material.

The "Conglomerate of Lima" has failed in several earthquakes (Carrillo and Garcia, 1985). This material is a coarse-grained granular soil, including gravel, cemented with "fine soils mixed with calcium carbonate". It is of Quaternary age, well jointed, and forms steep coastal bluffs outside of Lima, Peru. Following the failures, tension cracks were typically observed 2 to 4 m back from the slope crests, with some cracks as much as 10 to 20 m behind the slope crests. The slopes were also observed to fail in heavy rainstorms and due to sewer leaks.

Based on a review of documented failures, Sitar (1990) classified slope failures into two general categories. Moderately steep slopes, with slopes angles between 30° and 60°, tend to experience shallow planar failures, subparallel to the slope face. The second category, the very steep slopes with slope angles greater than 60°, tend to develop tension cracks behind the slope crest, and then fail in block toppling or by in shear at the base of the tension cracks. The failure modes for the moderately

steep and very steep slopes are schematically depicted in Figures 2.10 and 2.11, respectively. In both cases, the failure planes tend to be only a few meters deep.

2.4 CONCLUSIONS

A review of laboratory studies of weakly cemented sands shows that the material exhibits brittle behavior, particularly at low confining stresses, as would be anticipated near the face of a steep slope. Dynamic studies show that there is a reduction in strength due to cyclic loading, typically on the order of 85 to 90 percent of the static simple shear strength. In addition, results of dynamic tests have led to the development of shear modulus reduction and damping curves which are suitable for seismic site response analyses.

Numerous observations of seismically induced failures confirm the inference about the brittle behavior of the material based on the results of laboratory tests. Typically, the failure mass at the base of the slide shows an almost complete loss of cementation, with occasional intact blocks. There is little evidence of incremental permanent deformations eventually leading up to failure, though tension cracks are frequently observed at the crest of the slopes. These observations indicate that a failure based stability analysis rather than a deformation based analysis would be more appropriate for these type of slopes.

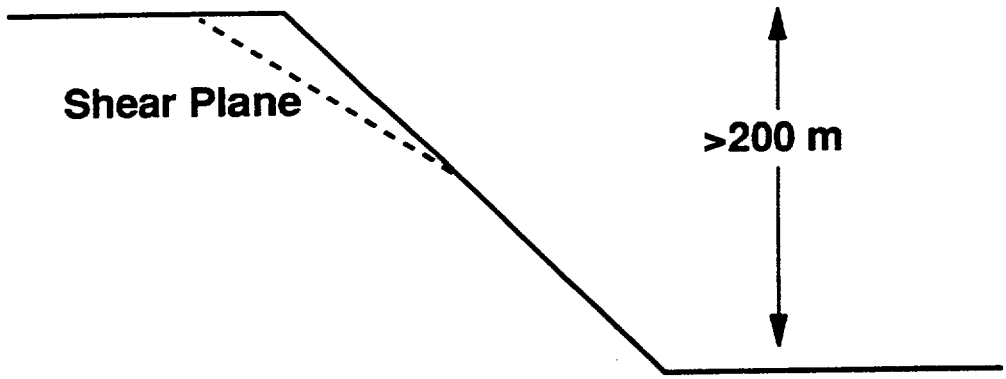

Figure 2.10: Failure mode for moderately steep slopes in cemented sands (after Sitar, 1990).

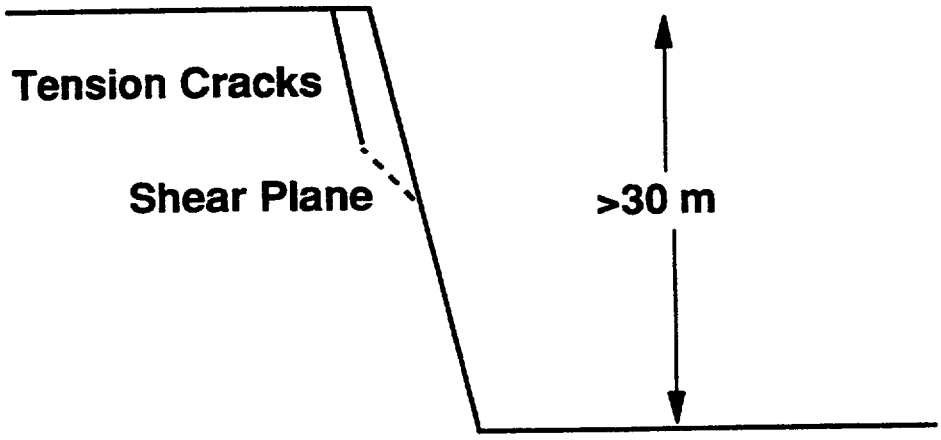

Figure 2.11: Failure mode for very steep slopes in cemented sands (after Sitar, 1990).

3. STATIC FINITE ELEMENT ANALYSIS OF STEEP SLOPES

Limit equilibrium analyses are often used in the assessment of slope stability. However, this method of analysis does not provide any opportunity to assess the actual stress distribution within the slope. Since the deformation characteristics of cemented sands depend on the actual stress conditions, other methods have to be employed to look at the stress distributions. The finite element method has been used extensively to analyze stresses in a variety of man-made and natural slopes. However, most of the work to date has concentrated on embankment slopes, where the desired stresses are often located along some curved failure surface through the interior of the embankment. For steep slopes, for example in weakly cemented soil, the failure surface tends to be shallow and planar, initiating in a zone of tension near the slope face, as already discussed (Sitar and Clough, 1983). Consequently, the critical stresses in a steep slope are located near a free boundary and are of relatively small magnitude; whereas in the flatter embankment slopes, the stresses are larger, since they are averaged along a deep curved surface within the interior of the embankment. Because of these differences, and since most of the finite element work to date has been directed toward embankment analysis, a study of the suitability of the finite element method for analysis of steep slopes was performed. Specifically, the accuracy of the computed stress distribution near the free surface of the slope was evaluated as a function of the element size and shape.

3.1 BACKGROUND

The accuracy of a linear elastic finite element analysis depends on the type of element, fineness of mesh, mesh layout, and the geometry of the problem. The effect of these variables can be estimated empirically, and a review of published FEM analyses of slopes has been carried out. Table 3.1 lists the papers reviewed and also gives the pertinent information about the fineness of the mesh and type of element used. Though the list is not exhaustive, it gives an overview of the history of the development of the finite element method over the last 25 years. Only two-dimensional studies are included, since three-dimensional studies were found not to be applicable to this research effort at this stage (e.g. Lefebrve 1973). In this review, the aspect ration is defined as the ratio of element height to element width.

The first application of the FEM to the analysis of stresses in a slope was performed by Clough and Woodward (1967) in the context of an analysis of stresses in an embankment dam. In their study, 3-node constant stress triangular elements were used with an aspect ratio of 1/2. The analyzed embankments were divided into 7 to 14 layers, so that the element height ranged from H/7 to H/14. In addition to studying the discretization effects, Clough and Woodward compared the effects of incremental construction to single step, or "gravity turn-on," loading and evaluated the effects of soil nonlinearity on an idealized dam. The study was validated by comparison of the computed deformations to deformations observed in an actual dam.

Table 3.1 Summary of Finite Element Analyses of Slopes

Source	Layers	Nodes	Aspect Ratio	Notes
Clough and Woodward (1967)	7,10,14	3	1/2	EM
Idriss and Seed (1967)	4	3	1/2	EM,D
Duncan and Goodman (1968)	10	4	1	EX
Zienkiewicz et al. (1968)	11	3	1	EX
Seed et al. (1969)	5,7	3	1	EM,D
Boughton (1970)	6	3	1/2	EM
Kovacs et al. (1971)	4	3	1/3	EM,D
Kulhawy and Duncan (1972)	9,12	3	NS	EM
Lefebvre et al. (1973)	8	4	1	EM
Smith and Hobbs (1974)	10	4	1/2,1	EM
Vrymoed (1981)	25	4	1/3	EM,D
Sitar and Clough (1983)	4	4	3	N,D
Naylor et al. (1986)	5,9	8,4	1	EM
Acar et al. (1988)	6,8	9	1	EM
Kuwano and Ishihara (1988)	10	4	1/2,1	EM,D
Griffiths and Prevost (1988)	4,6	4	1/2,1	EM,D
Naylor and Mattar (1988)	4,6	8	1	EM

[1]Embankment, [2]Included dynamic analysis, [3]Excavation, [4]Not shown, [5]Natural slope

Based on the results of this study, Clough and Woodward concluded that a staged analysis, in which layers of elements were added to the model to simulate incremental construction, was crucial in predicting deformations during construction. Stresses were affected to a lesser extent, though a staged analysis led to a more accurate prediction of stresses. As for the number of stages, or layers, necessary to

model deformations, virtually no difference was found between 7 and 14 layers for two horizontal sections through the idealized dam. Furthermore, they found that nonlinearity could easily be accounted for by changing the soil properties between stages in the analysis.

Duncan and Goodman (1968) used the FEM to analyze stresses and deformations in excavated rock slopes. For analysis of homogenous rock, they used a 4-node quadrilateral linear stress element with a height of H/10 and an aspect ratio of one. In their study, two sequences of analysis were considered: the "gravity turn-on" method, in which gravity was applied to the finite element mesh with the excavation at its final geometry; and the staged analysis, in which stresses were reduced according to the sequence of excavation. They found that for the purposes of estimating the stress distribution around an excavation, the simpler gravity turn-on method was adequate. However, for estimating displacements, the staged procedure was necessary to obtain reasonable accuracy. They concluded that the coefficient of lateral earth pressure, K, was critical for determining the stresses in the rock mass, and that the aspect ratio of elements should be between 1/5 and 5. In addition, they investigated the effect of joints on stresses and deformations. For a joint set occurring in only one direction, an equivalent anisotropy was used to model the joints. Joints were also modeled using one- and two-dimensional elements (1-D and 2-D, respectively). They concluded that the 1-D joint element was more versatile than the 2-D element for modelling joints, and that joints had little effect on initial stresses in the rock mass.

Excavation in rock has been analyzed by Zienkiewicz (1968) assuming the rock was a "no-tension" material. In his study, a 4-node quadrilateral element was used with a height of H/11 and an aspect ratio of one. The rock mass was considered to be unable to carry tensile stress due to the formation of joints and fractures, and an iterative process was used transfer stress to other regions of the rock such that in the end, no tensile stresses existed. Zienkiewicz concluded that this type of analogy represented a "lower bound" solution to the stress distribution in the rock mass.

Sitar and Clough (1983) used the FEM to specifically model naturally occurring steep slopes in weakly cemented soils. A 4-node quadrilateral element with an aspect ratio of 3 was used in their analyses. Sitar and Clough concluded that a zone of tension occurs behind the crest of the slope, as well as in a small zone on the face of a vertical slope. This appeared to concur with observed failures in these types of materials. However, it should be noted that they used elements with an aspect ratio greater than one.

Smith and Hobbs (1974) used the FEM to analyze the observed behavior of model slopes in a centrifuge. In particular, aspect ratios of 1/2 and 1 were compared. Discrepancies were noted when the coarser mesh (aspect ratio of 1/2) was used. In addition, the effect of overall width of the finite element mesh was studied. They showed that, even with boundaries as close as 1H from the toe and crest, the proximity of the boundary had little effect on the stress distribution in the vicinity of the slope. Of particular interest to the current research, is the fact that relatively poor agreement was observed between the finite element model and the centrifuge models of steep slopes.

Naylor and Mattar (1988) studied the effects of element height when using FEM to model embankment dams. They concluded that only 4 to 6 layers are necessary in most cases to properly analyze stresses in an embankment, not the 10 layers as is the common practice. However, in their analyses, 8-node serendipity elements were used, not the 4-node quadrilateral elements used in most of the previous studies.

The different discretization schemes used in FEM analyses of slopes during the 25 years since the publication of Clough and Woodward's pioneering work are summarized on Table 5-1. It can be seen that there is little consistency in the size and shape of the elements. The initial studies used element heights of approximately H/10. Since then heights have ranged from H/4 to H/25, though H/10 appears to be close to the most commonly used value. The most commonly used element in the studies reviewed herein is the 4-node element, though the 3-node element was common in earlier studies, and 8- and 9-node elements have become more common over the past 5 years. The aspect ratios (height/width) have typically been close to one, though they vary from approximately 1/3 to 3. Most of the above studies were analyses of embankments, where stresses in the interior of the slope were of greatest interest. In addition, many of the studies performed were subject to a limitation of the total number of elements due to computer costs. Most importantly, it is evident from this review that there is no commonly agreed upon approach to the discretization of the modelled domain. Therefore, a study was deemed necessary to determine the optimum size and aspect ratio of elements for use in studying steep slopes, where shallow zones of tension may occur.

3.2 PHYSICAL MODEL

Before the advent of computers, methods of studying stress distributions were relatively limited, and physical models using photoelastic materials were often used to obtain stresses and stress distributions directly. Photoelastic materials, such as gelatine, bakelite, and glass show contours of equal stress when polarized light is shone through them (Timoshenko and Goodier, 1970). Of these, gelatine is the only material sensitive enough to be of practical use when looking at stresses caused by the weight of the material itself.

Therefore, the gelatine slope model built by La Rochelle (1960) is used for comparison with the numerical analyses performed as a part of our study. La Rochelle studied the stability of excavations in London clay and used gelatine models to determine stress distributions. He considered four different slopes: a vertical slope, a 1 horizontal to 2 vertical (1H:2V) slope, a 2H:1V slope, and a "Bradwell" (benched) slope. Only the vertical slope is of interest herein.

La Rochelle's model was constructed by pouring a heated liquid gelatine mixture into a mold comprised of 13-mm thick perspex plates mounted on a wooden frame. All wood within the mold was lined with 2-mm thick perspex plates. Prior to pouring the mixture into the mold, all interior surfaces of the mold were coated with silicon grease. Once the mixture had dried, the perspex plates were removed and coated with heavy gear oil. The grease and oil effectively removed any friction between the mold and model. A schematic of the mold is presented in Figure 3.1.

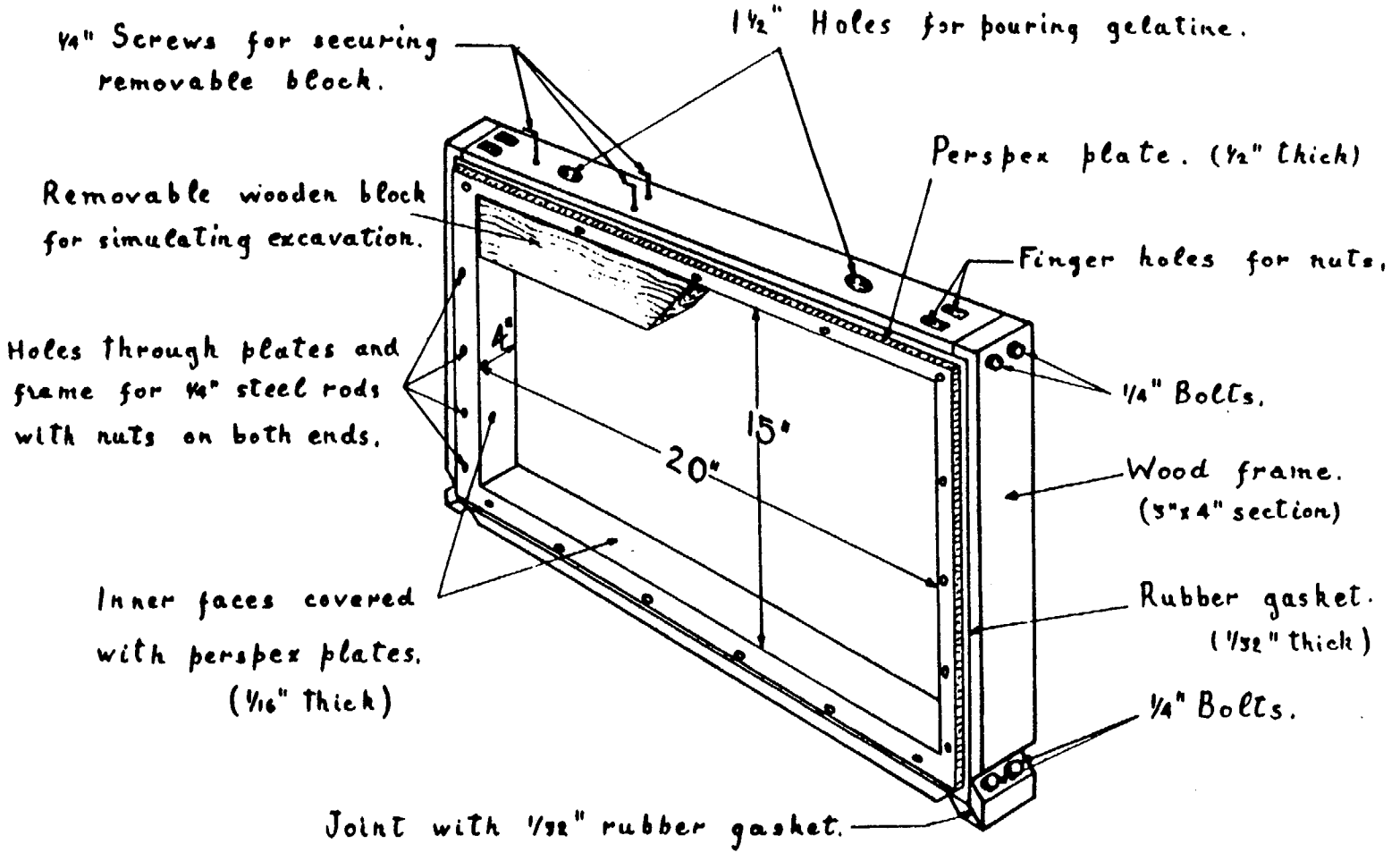

Figure 3.1: Gelatine model (from La Rouchelle, 1960).

The gelatine mix contained 12% leaf gelatine, 28% glycerine, and 60% water. Poisson's ratio of the mix was approximately 0.5, the unit weight was 10.7 kN/m^3, and for the analysis presented herein, Young's modulus will be assumed to be 62 kPa (Farquharson and Hennes, 1940).

Prior to testing, the model was checked for initial stresses and none were found. The wooden block supporting the molded slope face was then removed to simulate excavation and polarized light was shone through the mix to determine the "isoclinics", contours of constant direction of major principal stress, and the "isochromatics", contours of constant shear stress. La Rochelle was then able to separate the principal stresses using a numerical solution of the Laplace equation for the sum of the stresses.

La Rochelle concluded that boundary effects were eliminated in the vicinity of the slope by locating model boundaries at a distance of 2H; however, he noted some difficulties with modelling of the vertical slopes due to severe deformations. This problem was somewhat eliminated by cutting the toe of the slope with a 6-mm radius instead of a right angle. Nevertheless, approximately 5 percent deformation still remained, and a tension crack opened up to a depth of H/5 between the mold and the top of the model behind the crest of the slope. La Rochelle concluded that as a result, stresses in the vicinity of the slope included up to approximately 10 percent error, while stresses at the base of the model included approximately 2 percent error.

3.3 FINITE ELEMENT MODEL

The computer program FEAP (Taylor 1977) was used to model the gelatine slopes. An enhanced, plane strain 4-node quadrilateral element capable of modeling a Poisson's ratio very close to 0.5 was used, and the actual value of Poisson's ratio used in the analyses was 0.499. The left and right boundaries of the mesh were restrained from lateral movement, and the bottom of the mesh was restrained from vertical movement to simulate the gelatine model. The gravity turn-on method was used, in which full gravity was applied to the entire mesh at once.

Nine different meshes are discussed herein, though many others were used in the course of the study. Most of the analyses were performed using meshes containing elements of uniform size, as shown in Figure 3.2. A mesh curved at the base of the slope and an extremely fine mesh with variably-sized elements were also used to complete the study (Figures 3.3 and 3.4, respectively). A description of each mesh is given in Table 3.2. The number of uniformly-sized elements required to model the slope height is given by the variable n. As can be seen from Table 3.2, values of n ranged from 4 to 32. The aspect ratio, a, is defined as the vertical dimension, h, of a given element divided by its width, w. Aspect ratios (height/width) from 0.25 to 4 were used in the analyses.

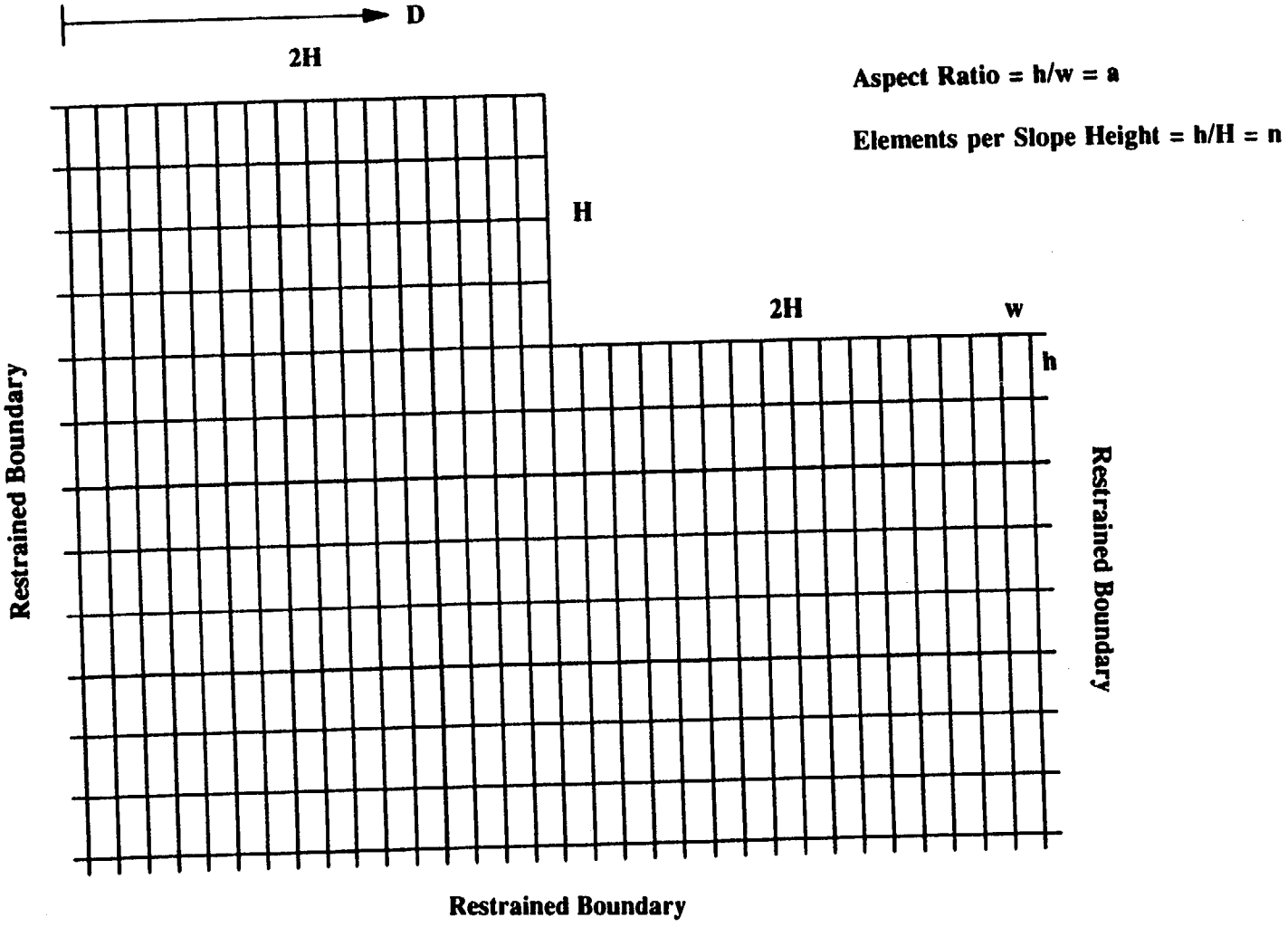

Figure 3.2: Typical FEM mesh and parameter definition.

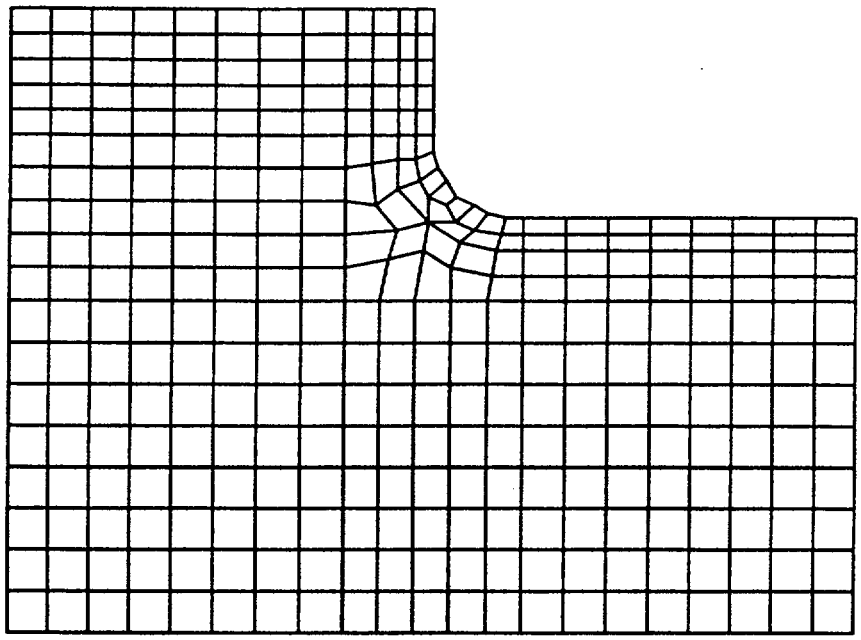

Figure 3.3: Curved FEM mesh.

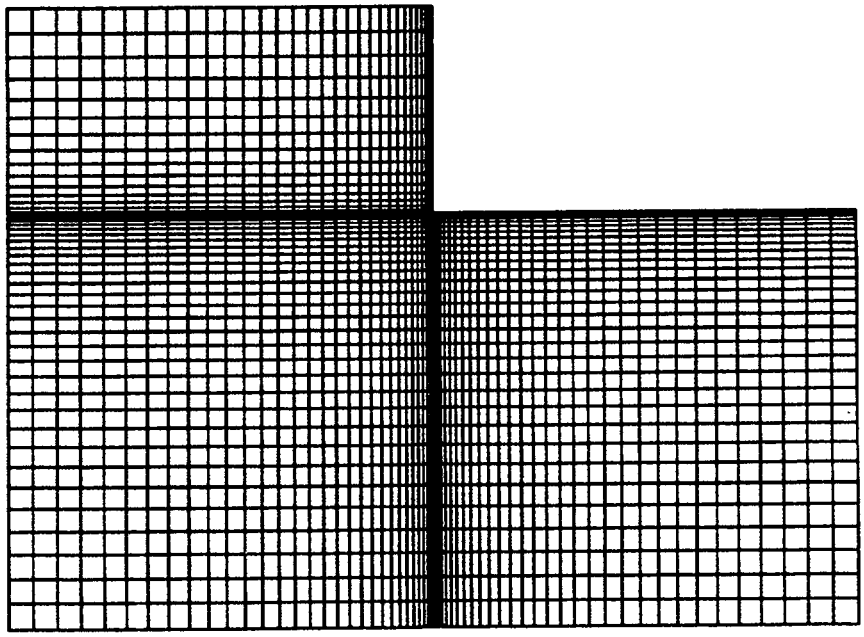

Figure 3.4: Variable sized element mesh.

Table 3.2 Summary of Meshes Used in Study

Mesh Description	Element Height	Aspect Ratio
n4a1	H/4	1
n4a4	H/4	4
n8a1	H/8	1
n12a1	H/12	1
n16a0.25	H/16	0.25
n16a1	H/16	1
n32a1	H/32	1
n64a0.25	H/64	0.25
n128a0.25	H/128	0.25
curved	NA	NA
variably-sized element	NA	NA

3.4 RESULTS

The most direct method to compare the gelatine and FEM model is to compare the shear stress, σ_1-σ_3, because this is the only stress which is obtained directly from the gelatine model, while the values of the principal stresses must be calculated numerically from the shear stress measurements. Shear stresses computed using the meshes *n4a1* and *n16a1* are compared to the shear stresses from the gelatine model in Figures 3.5 and 3.6, respectively. These meshes are composed of square elements with element heights of H/4 and H/16, respectively. Figure 3.5 shows only a general agreement with the gelatine model for the larger element size,

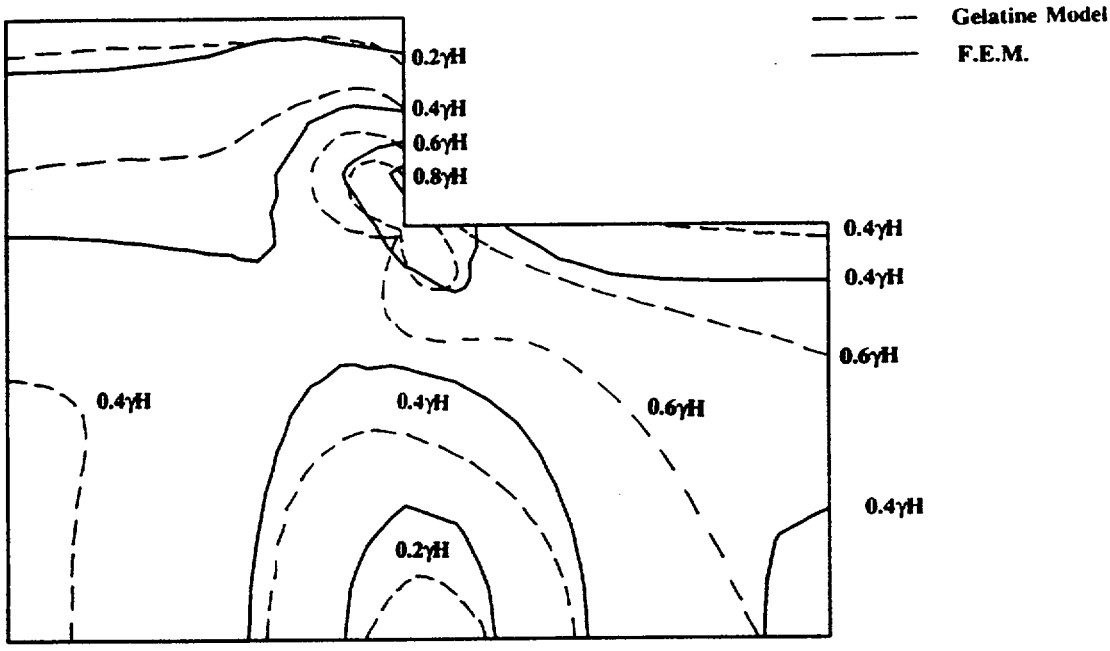

Figure 3.5: Comparison of σ_1-σ_3 between gelatine model and FEM using element n4a1.

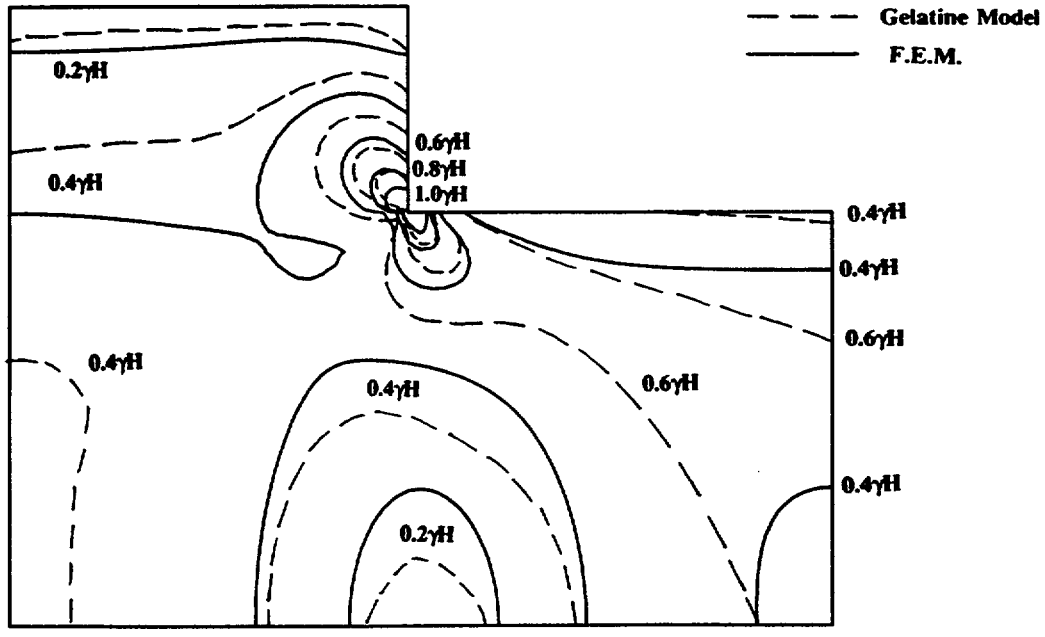

Figure 3.6: Comparison of σ_1-σ_3 btween gelatine model and FEM using element n16a1.

and this general agreement tends to decrease with increasing shear stress. The difference near the base of the slope is in excess of 25 percent, with the FEM model always underestimating the stress. The agreement is somewhat improved by quartering the element size (*n16a1*). The difference at the base of the slope is less than 20 percent.

The principal stresses were obtained from the gelatine model by applying the finite difference method to the results of the photoelastic test. The comparisons between the principal stresses computed from the gelatine model and those obtained from the FEM analyses are presented in Figures 3.7 through 3.10. Figures 3.7 and 3.8 show the comparison between the minimum principal stress, σ_3, contours for the large and small elements, respectively, and those obtained from the gelatine model. Similarly, Figures 3.9 and 3.10 compare the maximum principal stress, σ_1, contours between the finite element and gelatine models. All of these results indicate that there is a better agreement between the gelatine model and the finite element model for principal stresses than for shear stresses. There is excellent agreement between the minimum principal stresses in Figures 3.7 and 3.8, except within about 0.2H of the slope face. Good agreement is also found in Figures 3.9 and 3.10 for the maximum principal stresses. The figures also show that there is better agreement in both cases for the finer mesh (n=16). However, even with n=4, the overall agreement is still good.

The major differences between the gelatine and finite element model occur along the slope face for σ_3, and near the base of the slope for σ_1 and the shear stresses. Though it is not apparent from the stress contours, the finite element model

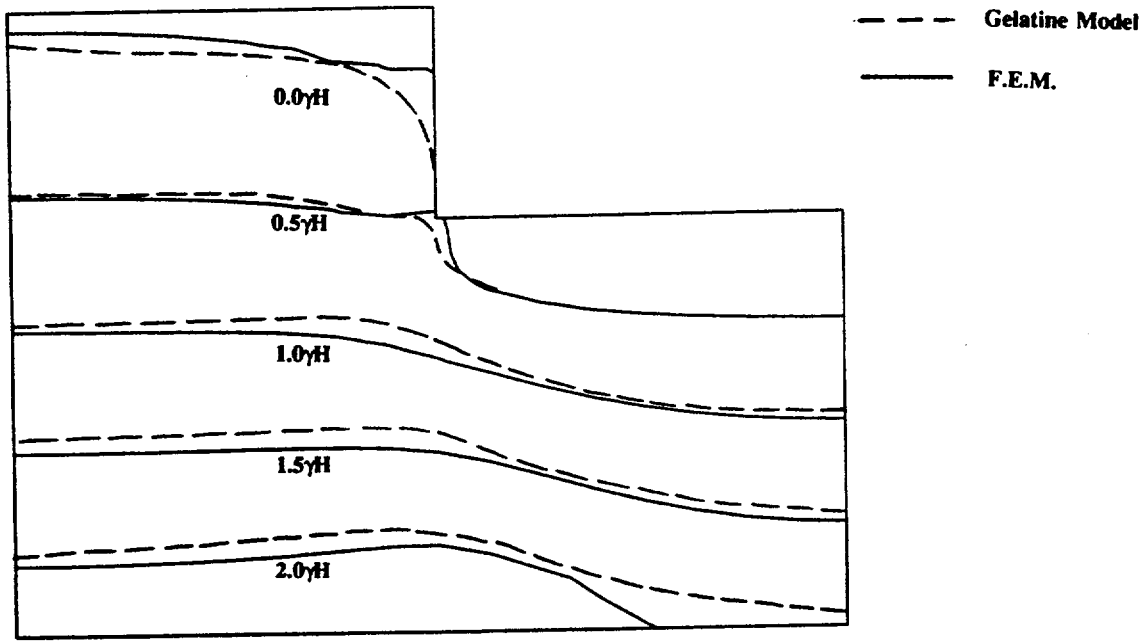

Figure 3.7: Comparison of σ_3 between gelatine model and FEM using element n4a1.

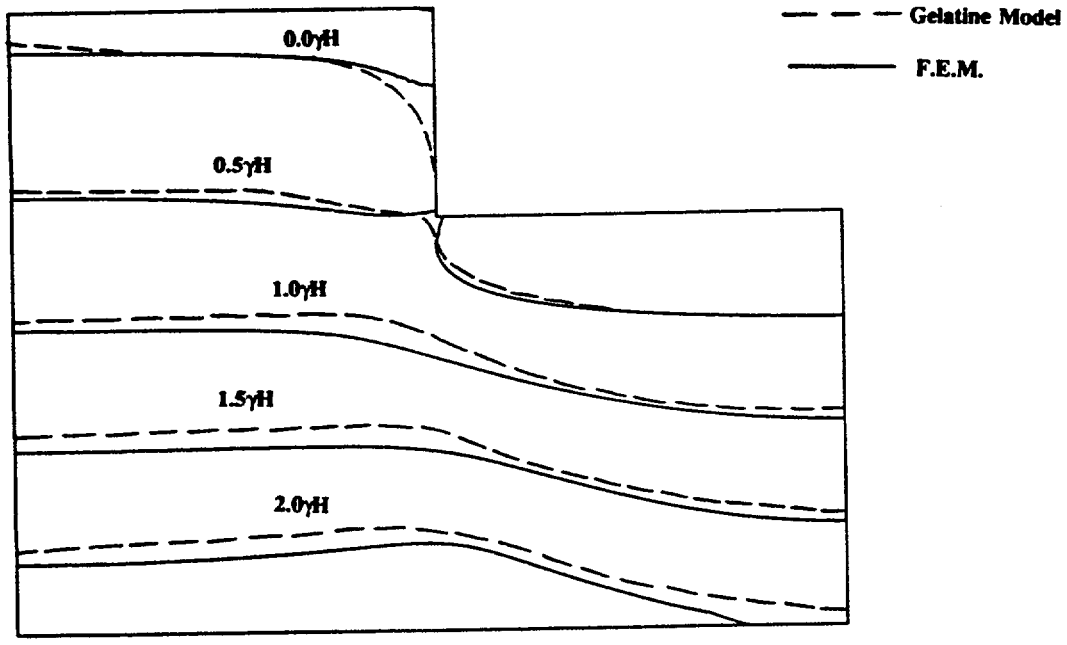

Figure 3.8: Comparison of σ_3 between gelatine model and FEM using element n16a1.

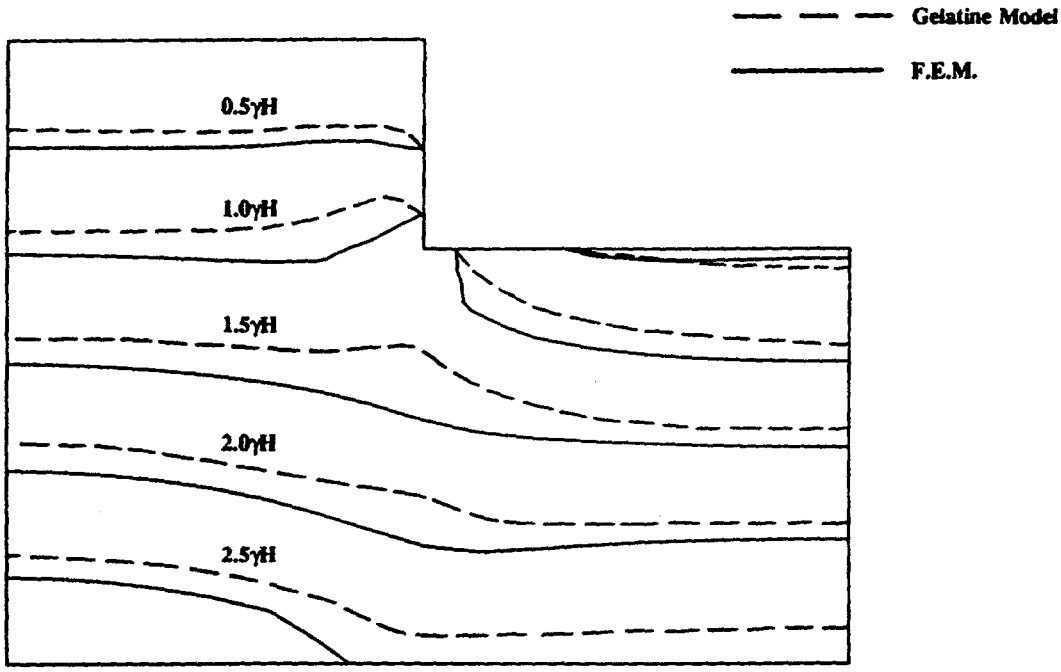

Figure 3.9: Comparison of σ_1 between gelatine model and FEM using element n4a1.

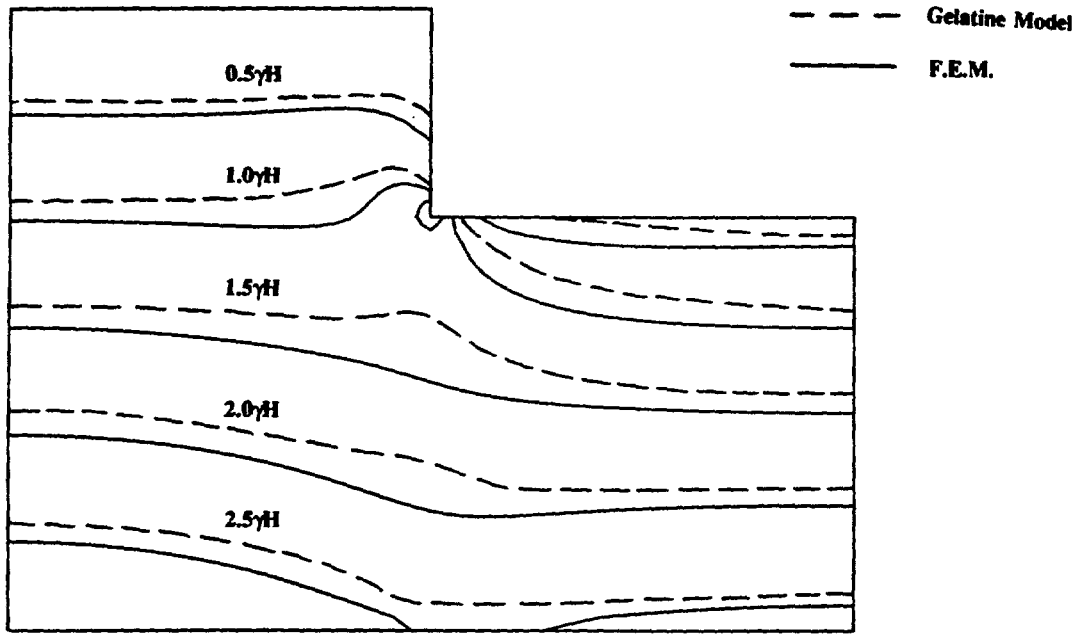

Figure 3.10: Comparison of σ_1 between gelatine model and FEM using element n16a1.

breaks down near the base of the slope. A review of stresses at the Gauss integration points reveals an oscillation between compression and tension within elements near the face of the slope. This oscillation dies out rather quickly, within about 0.2H of the face. The oscillation is apparently caused by a singularity in the solution matrix originating in the element at the base of the slope. It is important to note that stresses in this zone may not be critical in a typical slope stability analysis because the interior stresses are well defined. However, for shallow shear or tensile failures, these stresses are critical and must be quantified.

In an attempt to reduce this error, two additional meshes were used to compare the FEM model to the gelatine model: a mesh curved at the slope base and a very fine mesh with elements increasing in size away from the slope base. The results of these comparisons are shown for all stresses in Figures 3.11 through 3.13, and 3.14 through 3.16, respectively. It is apparent from these figures that not much improvement is achieved from using these more complicated meshes. In fact, Figures 3.15 and 3.16 match very closely the results for *n16a1* shown in Figures 3.9 and 3.10.

Tensile stresses along the top of the slope from the model edge to the crest of the slope are compared in Figure 3.17. The stresses from four uniform meshes with different sized elements are shown. Meshes indicated by *n4a1* and *n16a1* used square elements. Element *n4a4* is a tall element with the same height as *n4a1* and the same width as *n16a1*. Conversely, *n16a0.25* is a short element, with the same height as *n16a1* and the same width as *n4a1*. The figure shows that elements with the same heights give similar results, and the square elements bound the results. Since the results obtained using the meshes *n4a1* and *n4a4* give similar results, as

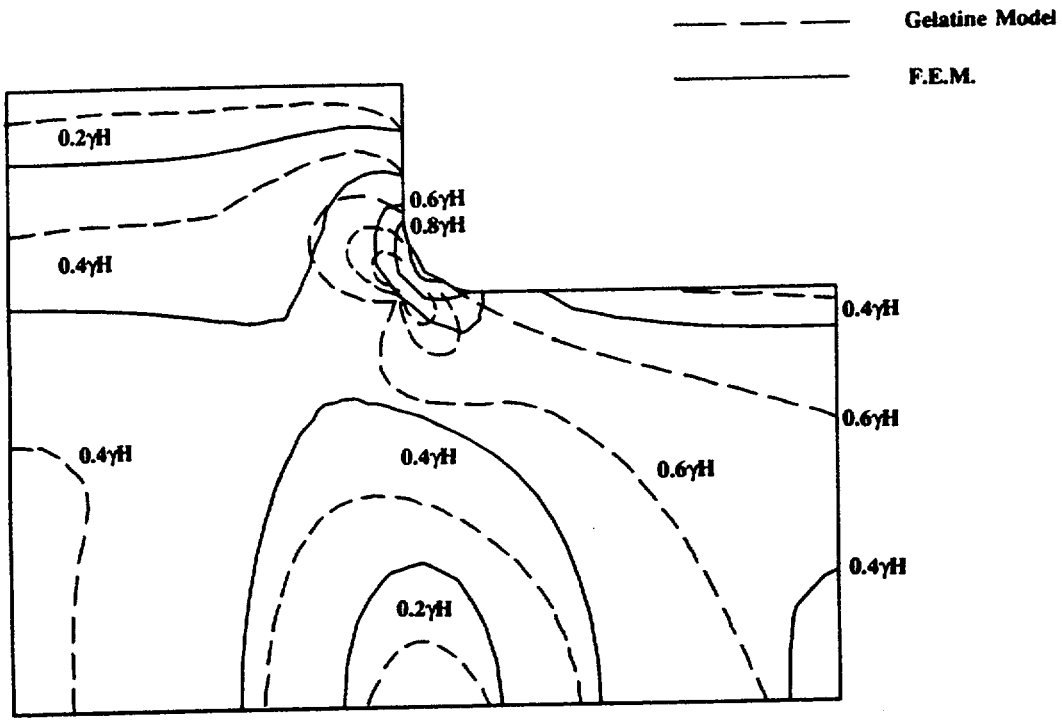

Figure 3.11: Comparison of σ_1-σ_3 between gelatine model and FEM using curved mesh.

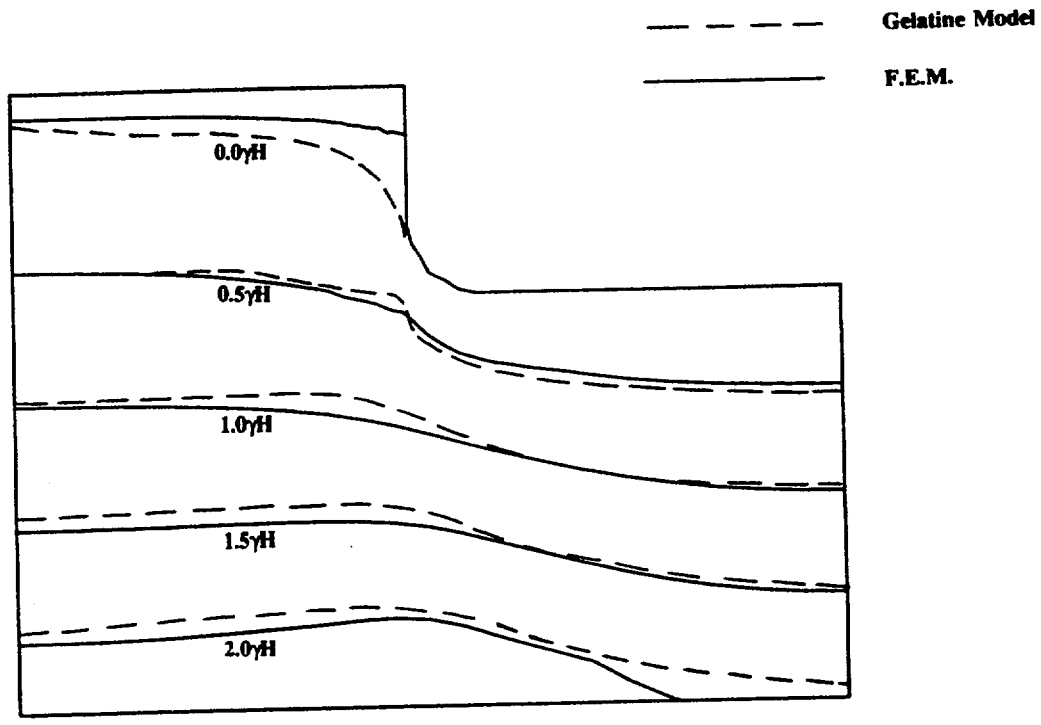

Figure 3.12: Comparison of σ_3 between gelatine model and FEM model using curved mesh.

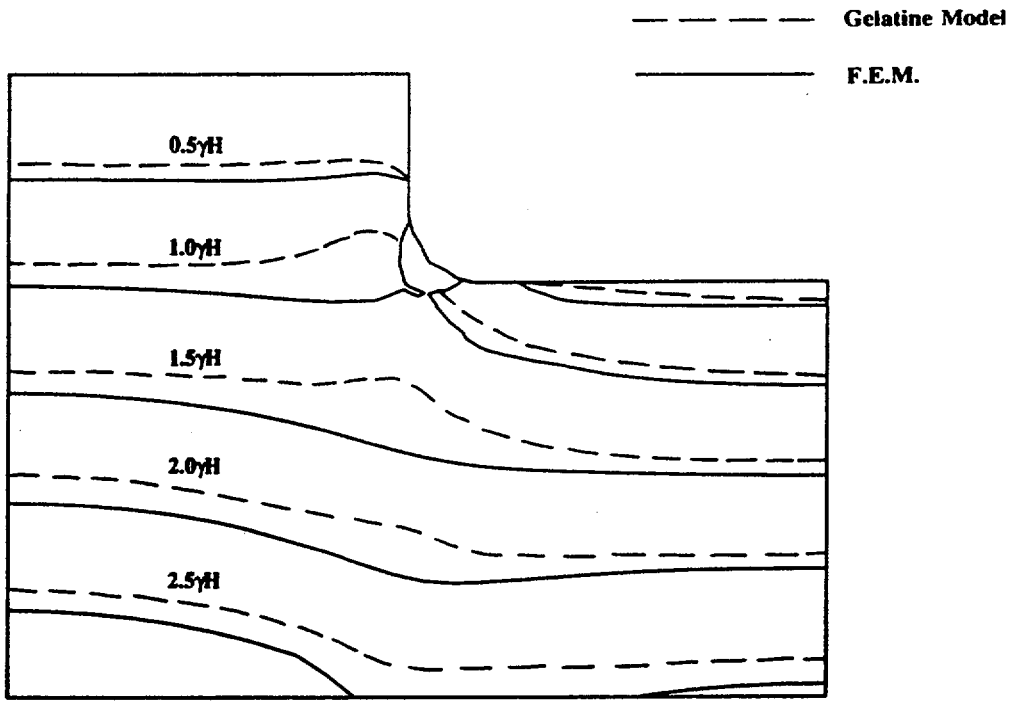

Figure 3.13: Comparison of σ_1 between gelatine model and FEM using curved mesh.

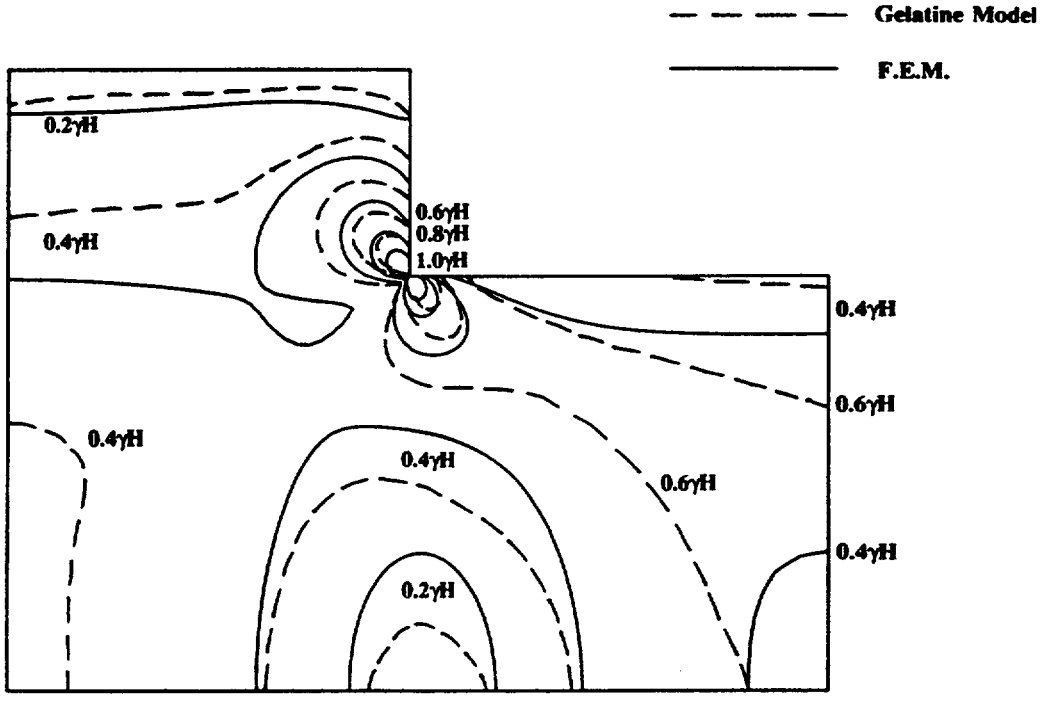

Figure 3.14: Comparison of σ_1-σ_3 between gelatine model and FEM using variable sized element mesh.

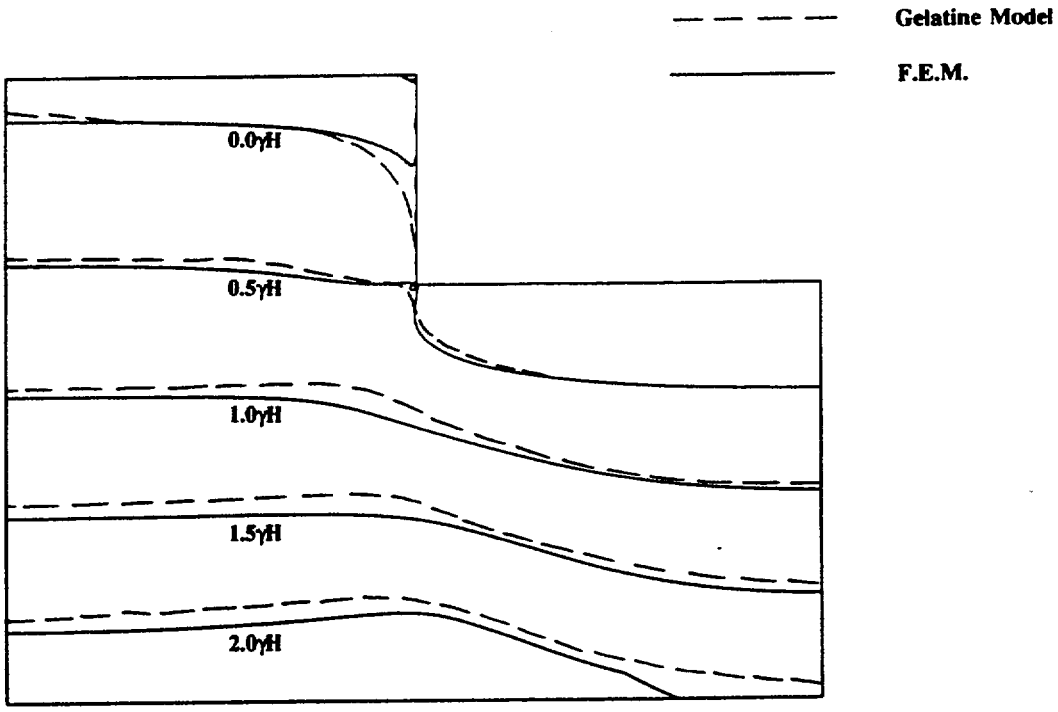

Figure 3.15: Comparison of σ_3 between gelatine model and FEM using variable sized element mesh.

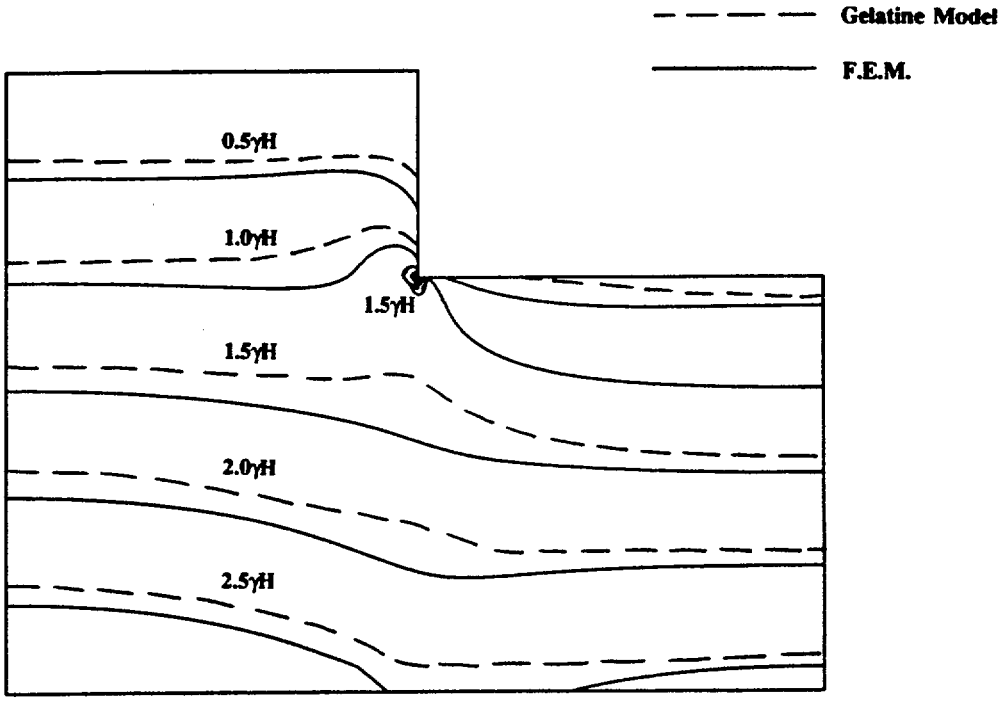

Figure 3.16: Comparison of σ_1 between gelatine model and FEM using variable sized element mesh.

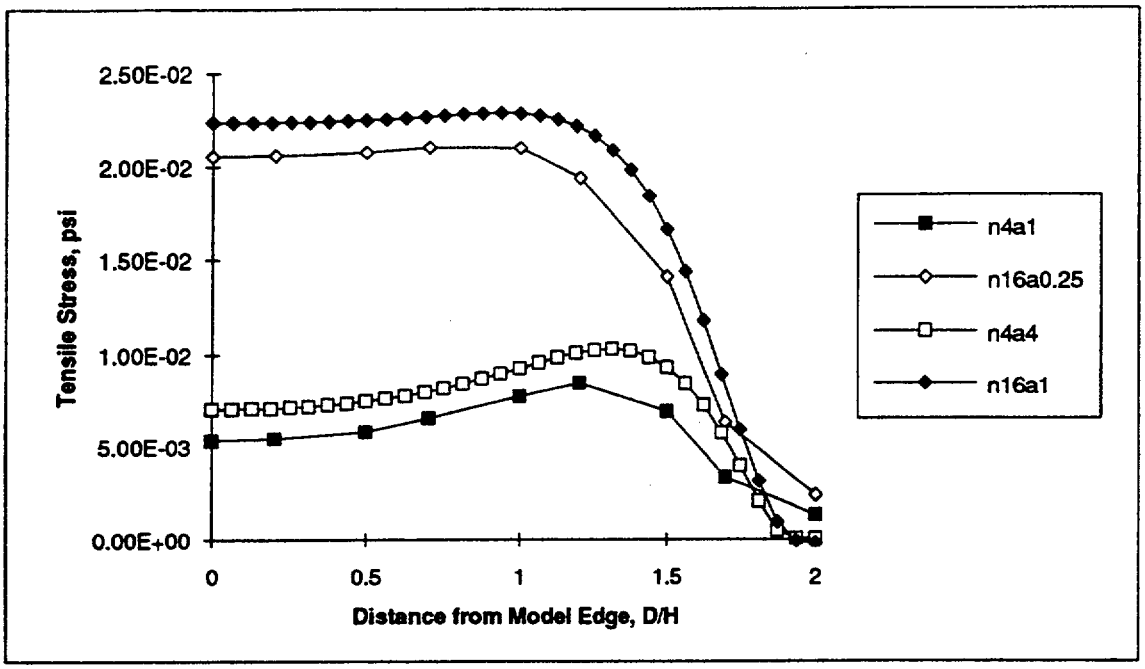

Figure 3.17: Variation of maximum tensile stress along top of slope with varying aspect ratio.

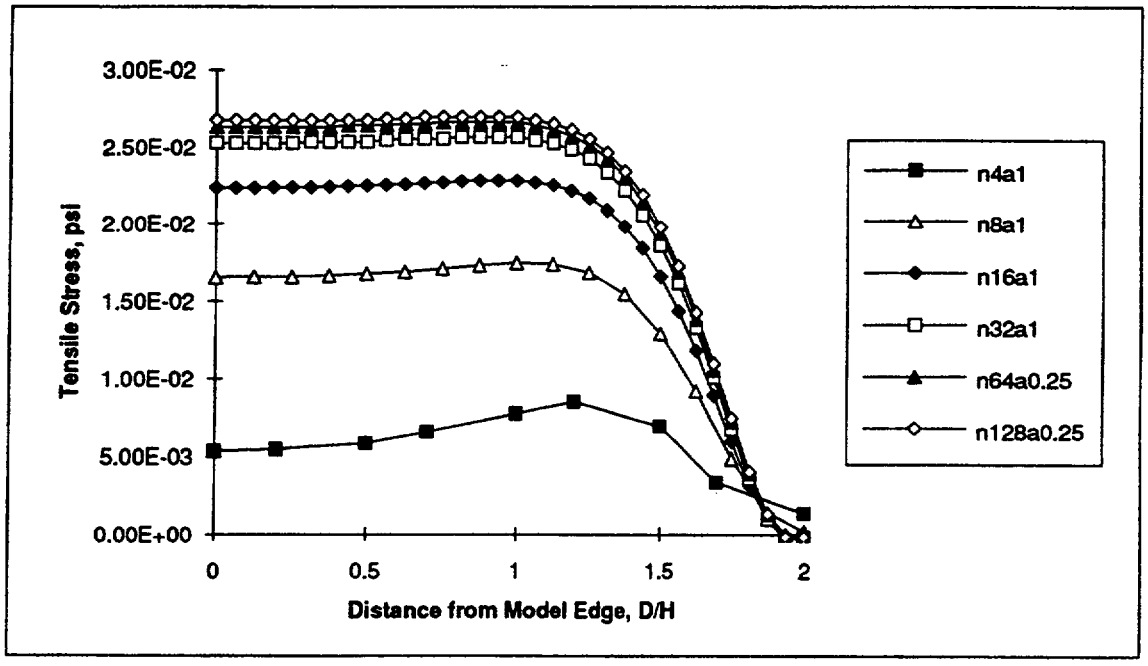

Figure 3.18: Variation of maximum tensile stress along top of slope with varying element size.

do *n16a1* and *n16a0.25*, it appears that the element height has more effect than aspect ratio when computing tensile stresses behind the crest of the slope.

The effect of element size on the magnitude of tensile stress is shown in Figure 3.18. All meshes are composed of uniformly sized square elements, except *n64a0.25* and *n128a0.25* which contained short rectangular elements in the upper portion of the mesh. Figure 3.18 shows that progressively finer meshes yield higher tensile stresses at a decreasing rate, with the finest mesh approaching a practical upper-bound. Based on these results, it appears that the element height of H/10 typically used in many studies predicts a much lower tensile stress behind the crest than may be actually present, and an element height of H/32 may be required to get within 10 percent of the upper-bound.

3.5 CONCLUSIONS

The results of the analyses indicate a reasonable agreement between the physical (gelatine) model and the numerical (FEM) model for shear stresses, and an overall good agreement between the two models for the principal stresses, even for coarse meshes. When looking at stresses along the top of the slope, the height of the element tends to be more important than the aspect ratio, at least for aspect ratios up to 4. In all cases, the greatest difference between the two models occurs in the vicinity of the slope. Therefore, due to limitations in the FEM analyses used herein, accurate stresses could not be determined within 0.2H of the slope face. Finally, an element height of H/10 commonly used in FEM analyses of slopes does not appear

to accurately define tensile stresses behind the crest of the slope, and an element as small as H/32, or higher order elements, may be necessary to determine stresses within 10 percent of the upper-bound.

The difficulty of modeling stresses behind the free face of steep slopes, and the fineness of mess required to accurately model stresses behind the crest of steep slopes are of concern. In light of these results, an approach other than the finite element method, and in fact, other than detailed stress analysis, may be advantageous to the study of the response of steep slopes in weakly cemented soil, as is explored next.

4. THE GENERALIZED HYPERELEMENT METHOD

The generalized hyperelement (GHE) method was developed by Deng (1991) for two-dimensional seismic response analysis. Deng showed that this method works well for steep slopes, and in fact, is not applicable to shallow slopes (less than about 20 degrees). The GHE method, coded by Deng into the computer program GROUND2D (Deng et al., 1994), greatly reduces the number of degrees of freedom required for the analysis of two-dimensional site response, as compared to the finite element method. In addition, the current program offers greater capability for analysis of a variety of seismic waves than readily available finite element programs. For these reasons, the GHE method, as coded in GROUND2D, is used for the analysis of the seismic response of steep slopes presented herein.

4.1 COMPUTATIONAL MODEL

In order to illustrate the concepts used in the computational model, consider a site shown in Figure 4.1. A model of this site using the methods coded in GROUND2D is presented in Figure 4.2. The site is divided into two large blocky regions and two semi-infinite regions on the left and right sides, respectively. Within each region, the soil and rock strata are divided into a group of perfectly horizontal layers, with material properties perhaps varying from layer to layer. The boundaries between the regions can be of arbitrary shape. The whole model rests on a visco-elastic halfspace.

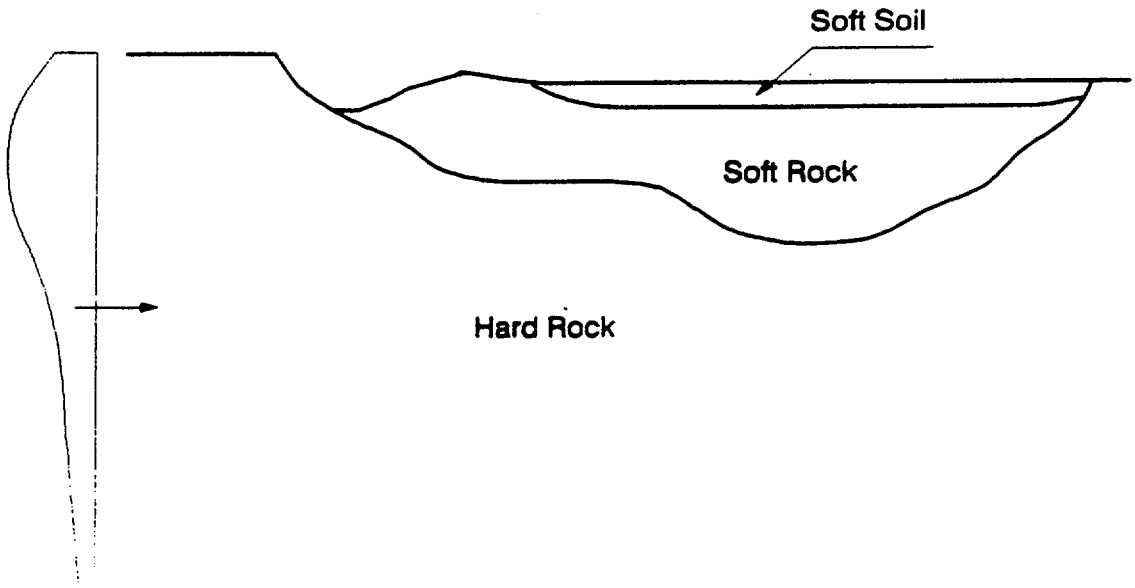

Figure 4.1: Site for two-dimensional seismic site response analysis (after Deng, 1991).

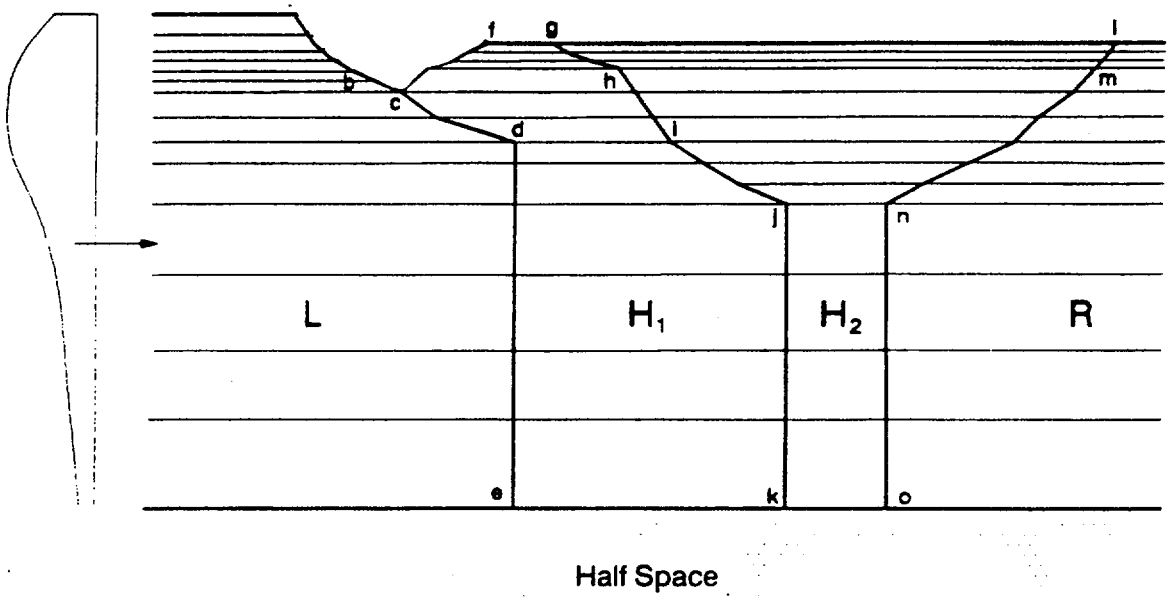

Figure 4.2: Typical model of site using GROUND2D (after Deng, 1991).

In general, each blocky region is simulated by a generalized hyperelement, H_1, H_2, ..., H_n. The semi-infinite regions, L and R, are simulated by generalized transmitting elements. The prefix "generalized" refers to the ability of these elements to model arbitrarily shaped boundaries. Nodal points exist only at the boundaries between any two regions, and only the motions at the nodal points need to be solved in the global equations of motion. Once the nodal point motions are obtained, the motions within each region can be recovered through a nodal expansion process.

4.1.1 The Complex Response Method

The techniques used in formulation of the generalized transmitting element (GTE) and the generalized hyperelement (GHE) utilize the complex response method to simulate viscous damping within the elements. For simplicity, the complex response method is described below for a simple damped oscillator. The general form of the equation of motion for the simple damped oscillator is:

$$M\ddot{u} + C\dot{u} + Ku = q(t) \tag{4.1}$$

where M, C, and K are mass, viscous damping and stiffness, respectively; $q(t)$ is the driving force; and $\ddot{u}$, $\dot{u}$, and u are the acceleration, velocity, and displacement of the system. The solution of the equation of motion for harmonic motion at circular frequency ω is given by:

$$(K + i\omega C - \omega^2 M)U' = Q' \tag{4.2}$$

where U' and Q' are the complex amplitudes of the displacement and force, respectively. Employing the concept of complex stiffness, the above equation can be reduced to the following:

$$(K' - \omega^2 M)U' = Q' \tag{4.3}$$

where $K' = K + i\omega C$ is the complex stiffness which can be formulated using the complex modulus for linear visco-elastic materials. In the context of the methodology used herein, viscous damping is employed through the use of the complex shear modulus G',

$$G' = G(1 - 2\beta^2 + i2\beta\sqrt{1-\beta^2}) \tag{4.4}$$

and complex constrained modulus

$$M_C' = M_C(1 - 2\beta^2 + i2\beta\sqrt{1-\beta^2}) \tag{4.5}$$

where β is the ratio of critical damping for S- and P-waves. Though some laboratory studies indicate that β may be different for S- and P-waves, there are treated as equal in this study. It is possible, however, to define separate values in GROUND2D. It should be noted that $M_C' = \lambda' + 2G'$, where the complex value of Lame's constant is

$$\lambda' = \lambda(1 - 2\beta^2 + i2\beta\sqrt{1-\beta^2}) \tag{4.6}$$

Using definitions of complex modulii leads to:

a real value of Poisson's ratio,

$$\nu = \frac{\lambda'}{2(\lambda' + \mu')} = \frac{\lambda}{2(\lambda + \mu)} \tag{4.7}$$

an exact value for amplitude, because

$$|K'| = K \tag{4.8}$$

and, for small values of β, a small error in the phase of the solution:

$$\phi_2 - \phi_1 \approx \frac{2\beta}{1+\alpha} \tag{4.9}$$

where ϕ_1 and ϕ_2 are the phase lags between the displacement and the driving forces using the complex response method and modal analysis, respectively. The phase lag is greatest at low frequencies (for the static case $\alpha = 0$); is approximately β (in radians) near the natural frequency; and disappears with high frequencies. For the sake of simplicity, the prime symbol (') indicating complex values will be dropped from here on, though it should be understood that the complex values of these variables are used throughout. For a detailed discussion of the complex response method, see Deng (1991).

4.1.2 Equations of Motion

The equations of motion for the model shown in Figure 4.2 can be written generally as

$$([L]_L+[R]_R+\sum_1^n [H]_i)\{U\}=\{P\} \tag{4.10}$$

where $[L]_L$ is the stiffness matrix for the left semi-infinite region, $[R]_R$ is the stiffness matrix for the right semi-infinite region, and $[H]_i$ is the stiffness matrix for the i-th blocky region H_i. $\{U\}$ is vector containing the motions at all nodal points, and $\{P\}$ is the force vector, which is of different form for different incident wave cases. For surface wave incidence, assuming the wave propagates from left to right, the vector $\{P\}$ can be expressed as

$$\{P\}=([L]_L+[R]_L)\{U\}_L^R \tag{4.11}$$

where $\{U\}_L^R$ is the incident surface wave vector, the subscript L refers to the left boundary, and the superscript R refers to the direction of wave propagation. Similarly, if the incident surface wave propagates from right to the left, the $\{P\}$ vector becomes

$$\{P\}=([L]_R+[R]_R)\{U\}_R^L \tag{4.12}$$

For body wave incidence, the $\{P\}$ vector is

$$\begin{aligned}\{P\}=&[L]_L\{U_f\}_L+[R]_R\{U_f\}_R+\sum_{i=1}^n [H]_i\{U_f\}_i\\ &+[L_0]_L\{U_f\}_L-[R_0]_R\{U_f\}_R+\sum_{i=1}^n [H_0]_i\{U_f\}_i\end{aligned} \tag{4.13}$$

where $\{U_f\}_L$, $\{U_f\}_R$, $\{U_f\}_i$ are the "free field" motion vectors for the left, right, and H_i regions, respectively (i.e. the response vectors of the regions corresponding to the incident wave, if the motions in the regions are computed using one-dimensional layer

models with no lateral boundaries). The matrices $[L_0]$, $[R_0]$ and $[H_0]_i$ are defined as follows:

$$[L_0]_L = i\kappa_a[A]_L + [D]_L \tag{4.14}$$

$$[R_0]_R = i\kappa_a[A]_R + [D]_R \tag{4.15}$$

$$[H_0]_i = \begin{bmatrix} -(i\kappa_a[A]_{L_i} + [D]_{L_i}) & 0 \\ 0 & i\kappa_a[A]_{R_i} + [D]_{R_i} \end{bmatrix} \tag{4.16}$$

where the subscripts L_i and R_i are for the left and right boundaries of the H_i region, respectively. The matrices $[A]$ and $[D]$ are related to the eigenvalue problem of a layered system and will be defined in the following section. The parameter κ_a is the apparent wavenumber of the incident body wave in the underlying halfspace and is defined as

$$\kappa_a = \kappa_0 \sin\theta_0 \tag{4.17}$$

where $\kappa_0 = \kappa_s$ for SH- and SV-waves, and $\kappa_0 = \kappa_p$ for P-waves. θ_0 is the incident angle, measured from the z-axis, with the positive value corresponding to a wave propagating toward the positive x-direction.

4.1.3 Eigenvalue Problem of the Layered Halfspace

Consider a semi-infinite layered region bounded at the left end by an irregular boundary S, shown in Figure 4.3. According to Deng (1991), the surface wave motions in the region along a curve S^*, which is parallel to the boundary S at a

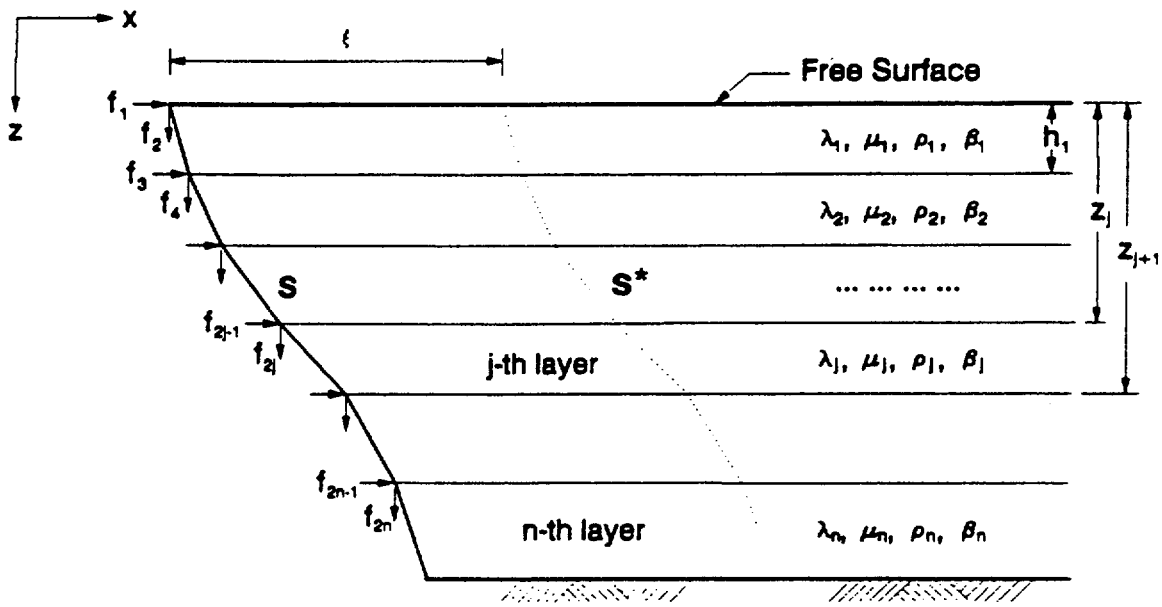

Figure 4.3: Semi-infinite layered region (after Deng, 1991).

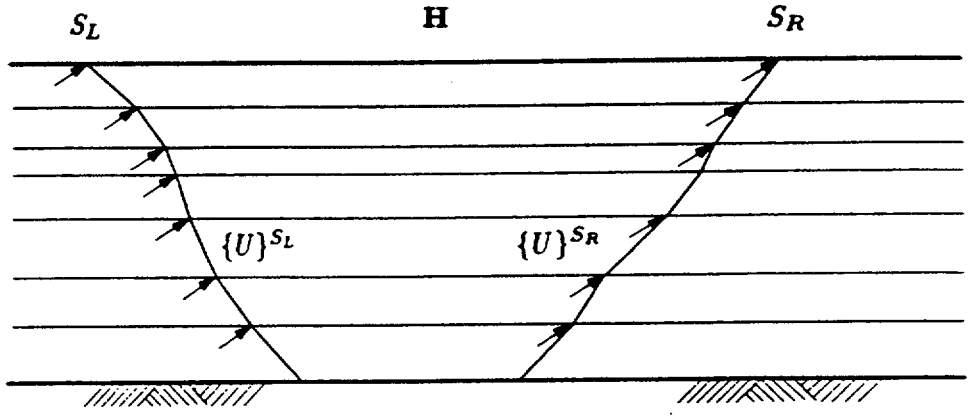

Figure 4.4: Layered blocky region bounded by irregular boundaries (from Deng, 1991).

distance x, can be generally expressed as a superposition of the generalized surface wave modes:

$$\{U(\omega,x)\}=\sum_{s=1}^{N}\{v\}_s\, e^{-i\kappa_s x}\alpha_s \tag{4.18}$$

where $\{U(\omega,x)\}$ is the frequency-dependent displacement vector, $\{v\}_s$ is the s-th wave mode of the layered region, κ_s is the s-th wavenumber, and α_s is the mode participation factor for the mode. Equation (4.18) is the general form for both in-plane (e.g. SV-waves) and out-of-plane motions (e.g. SH-waves). Assuming, for example, that the bottom of the layered system is fixed, then $N = 4n$ for in-plane motions, where n is the number of discretized nodal points along the boundary S, and $N = 2n$ for out-of-plane motions.

The eigenvalues and eigenvectors must be solved for each frequency from the following generalized eigenvalue problem

$$([A]\kappa^2+i[B]\kappa+[G]-\omega^2[M])\{v\}=\{0\} \tag{4.19}$$

where ω is the circular frequency, $[A]$, $[B]$, $[G]$, and $[M]$ are frequency independent matrices related to the material properties of the layered region and the geometry of the irregular boundary S. Depending on the different type of motions concerned, (e.g. in-plane or out-of-plane) and different order of the discretization (e.g. 1st- or 2nd-order), the matrices may have different forms and dimensions.

Equation (4.19) can be solved by a method proposed by Deng (1991). This solution yields $4n$ pairs of the wave modes and wavenumbers for the in-plane motions ($2n$ pairs for the wave modes and wavenumbers for the out-of-plane motions). Half

of the wave modes represents the surface waves propagating in the positive x-direction and the other half represent the waves in the negative x-direction. The wave modes and wavenumbers are used in generating the transmitting boundary matrices and in computing the motions in any part of the layered regions.

4.1.4 Generalized Transmitting Elements

The generalized transmitting elements (GTE) are formulated by using the exact analytical solution in the horizontal direction and a discretized displacement shape function along the irregular boundary S. The boundaries of these elements transmit energy accurately in the horizontal direction and represent the perfect "infinite" boundary condition. The GTE stiffness matrix represents the response of the semi-infinite region to the boundary nodal forces. For each irregular boundary S, two stiffness matrices exist. One is for the waves propagating toward the positive x-direction, i.e., the semi-infinite region is at the RIGHT of the boundary, and is denoted $[R]$. The other is for the waves propagating toward the negative x-direction, or the semi-infinite region is at the LEFT of the boundary, and is denoted $[L]$. We have generally the following force-displacement relationship for the right region

$$\{P\}=[R]\{U\} \tag{4.20}$$

and, for the left region

$$\{P\}=[L]\{U\} \tag{4.21}$$

where $\{P\}$ is the nodal force vector along the boundary, $\{U\}$ is the nodal displacement vector along the boundary respectively, and $[L]$ and $[R]$ are the GTE stiffness matrices.

According to Deng (1991), the GTE stiffness matrices for both the in-plane and the out-of-plane motions can generally be written in the following form:

$$[R]=i[A][V][\bar{\kappa}][V]^{-1}+[D] \tag{4.22}$$

$$[L]=i[A][W][\bar{\kappa}][W]^{-1}-[D] \tag{4.23}$$

In the two equations, the dimensions of all matrices are $2n$ x $2n$ for the in-plane motions (n x n for the out-of-plane motions). $[V]$ is the matrix containing all right eigenvectors and $[W]$ is the matrix containing all left eigenvectors, respectively; and $[\bar{\kappa}]$ is a diagonal matrix containing all the wavenumbers (i.e., the eigenvalues) for the corresponding modes. These eigenvalues and eigenvectors serve as the basis for the mode superposition of the motions in the layered region, as defined in Eq.(4.19). The matrix $[D]$ is related to the geometry of the lateral boundary and the material properties of the layered region, and is assembled from the submatrices of individual layers.

4.1.5 The Generalized Hyperelement

Each of the blocky regions in Figure 4.2 is simulated by a generalized hyperelement (GHE) which is an extension of the generalized transmitting element. The following gives a brief outline of the formulations of GHE. The detailed derivation can be found in Deng (1991).

Consider a layered blocky region bounded laterally by two irregular boundaries, S_L and S_R, respectively, as shown in Figure 4.4. The layers inside the region are assumed to be perfectly horizontal, but material properties may differ from layer to layer. Nodal points exist only along the boundaries. The displacement shape functions in the region, i.e., the correlations between the displacement vectors of the two boundaries, are obtained by the superposition of all right-propagating modes from S_L and all left-propagating modes from S_R. After considering the effect of the boundary geometry, the general form of the displacement vector within the region can be written as

$$\begin{aligned} \{U(\xi)\} &= \{U(\xi)\}_{LR} + \{U(\hat{\xi})\}_{RL} \\ &= [Q(\xi)]_{LR}\{U(L)\}_{LR} + [Q(\hat{\xi})]_{RL}\{U(R)\}_{RL} \end{aligned} \tag{4.24}$$

where the vector $\{U(L)\}_{LR}$ is the right-propagating component of the displacement vector defined at the left boundary, the vector $\{U(R)\}_{RL}$ is the left-propagating component of the displacement vector defined at the right boundary. $\{\xi\}$ is the vector which defines the distance from the left boundary to the line of interest, and $\{\hat{\xi}\} = \{d\}-\{\xi\}$ is the vector which defines the distance from the right boundary to

the line of interest, where {d} is the distance vector between the left and the right boundaries.

The matrix operator $\otimes$ is defined as a term-by-term multiplication of the matrix entries. i.e., [C] = [A] $\otimes$ [B] implies that $c_{ij} = a_{ij} \times b_{ij}$. In this manner, $[Q]_{LR}$ and $[Q]_{RL}$ are matrices of the following form:

$$[Q]_{LR}=([V]_L \otimes [\psi]_L)[V]_L^{-1}$$
$$[Q]_{RL}=([W]_R \otimes [\psi]_R)[W]_R^{-1} \tag{4.25}$$

where $[V]_L$ is the right eigenvector matrix defined along S_L, $[W]_R$ is the left eigenvector matrix defined along S_R. The entries in the matrices $[\Psi]_L$ and $[\Psi]_R$ are defined as

$$(\psi_{st})_L=e^{-i\xi_s\kappa_t}$$
$$(\psi_{st})_R=e^{-i\hat{\xi}_s\hat{\kappa}_t} \tag{4.26}$$
$$s,t=1, \ldots, n$$

for the out-of-plane motions, and

$$(\psi_{2s-1,t})_L=e^{-i\xi_s\kappa_t}, \quad (\psi_{2s,t})_L=e^{-i\xi_s\kappa_t}$$
$$(\psi_{2s-1,t})_R=e^{-i\hat{\xi}_s\hat{\kappa}_t}, \quad (\psi_{2s,t})_R=e^{-i\hat{\xi}_s\hat{\kappa}_t} \tag{4.27}$$
$$s=1, \ldots, n; \quad t=1, \ldots, 2n$$

for in-plane motions, where $\{\kappa\}$ and $\{\hat{\kappa}\}$ are defined from the left and right boundaries, respectively. All the matrices are of dimension n x n for the out-of-plane motions, and of dimension $2n$ x $2n$ for the in-plane motions.

For the left boundary, $\{\xi\} = \{0\}$ and $\{\hat{\xi}\} = \{d\}$. For the right boundary, $\{\xi\} = \{d\}$ and $\{\hat{\xi}\} = \{0\}$. Thus the nodal displacement vector of the blocky region can be written as

$$\begin{aligned}\{U\} &= \begin{Bmatrix}\{U(L)\}\\ \{U(R)\}\end{Bmatrix} = \begin{Bmatrix}\{U(L)\}_{LR} + \{U(L)\}_{RL}\\ \{U(R)\}_{LR} + \{U(R)\}_{RL}\end{Bmatrix} \\ &= \begin{bmatrix}[I] & [Q]_{RL}\\ [Q]_{LR} & [I]\end{bmatrix}\begin{Bmatrix}\{U(L)\}_{LR}\\ \{U(R)\}_{RL}\end{Bmatrix}\end{aligned} \tag{4.28}$$

where $[I]$ is the identity matrix. Similarly, applying the boundary conditions of the GTE on both lateral boundaries, S_L and S_R, and considering all propagating components of the displacement field, the nodal force vector of the blocky region can be written as

$$\{F\} = \begin{bmatrix}[R]_L & -[L]_L[Q]_{RL}\\ -[R]_R[Q]_{LR} & [L]_R\end{bmatrix}\begin{Bmatrix}\{U(L)\}_{LR}\\ \{U(R)\}_{RL}\end{Bmatrix} \tag{4.29}$$

where $[R]$ and $[L]$ are the left and the right GTE stiffness matrices, respectively. The subscripts L and R denote that the matrices are defined at S_L and S_R, respectively. Combination of the Equations (4.28) and (4.29) leads to the following relationship:

$$\{F\} = [H]\{U\} \tag{4.30}$$

where the matrix $[H]$ is the hyperelement matrix:

$$[H] = \begin{bmatrix}[H]_{11} & [H]_{12}\\ [H]_{12} & [H]_{22}\end{bmatrix} \tag{4.31}$$

The components of the matrix $[H]$ are

$$
\begin{aligned}
[H]_{11} &= [R]_L[\psi]_1 + [L]_L[Q]_{RL}[\psi]_2[Q]_{LR} \\
[H]_{12} &= -[R]_L[\psi]_1[Q]_{RL} - [L]_L[Q]_{RL}[\psi]_2 \\
[H]_{21} &= -[R]_R[Q]_{LR}[\psi]_1 - [L]_R[\psi]_2[Q]_{LR} \\
[H]_{22} &= [R]_R[Q]_{LR}[\psi]_1[Q]_{RL} + [L]_R[\psi]_2
\end{aligned}
\tag{4.32}
$$

The matrices $[\Psi]_1$, $[\Psi]_2$ are defined as the following

$$
\begin{aligned}
[\Psi]_1 &= ([I] - [Q]_{RL}[Q]_{LR})^{-1} \\
[\Psi]_2 &= ([I] - [Q]_{LR}[Q]_{RL})^{-1}
\end{aligned}
\tag{4.33}
$$

The component matrices $[H]_{11}$, $[H]_{12}$, $[H]_{21}$, $[H]_{22}$ are of dimension n x n for out-of-plane motions, and $2n$ x $2n$ for in-plane motions.

4.2 FREE FIELD MOTIONS IN THE LAYERED REGIONS

The term "free field" herein denotes the responses of a layered system to a incident wave field, either an inclined body wave, or a surface wave, computed by one-dimensional model, i.e., without the lateral boundaries. The free field motions will be different for the different types of incident waves. The procedures used in GROUND2D in determining the free field motions are described below.

4.2.1 Inclined In-Plane Waves (SV- and P-Waves)

Consider a one-dimensional layered system, shown in Figure 4.5. Using a method similar to Chen et al (1981), the response of the layered system to incident in-plane (SV- or P-waves) can be obtained by solving the following equation:

$$([A]\kappa_a^2+i[B]\kappa_a+[G]-\omega^2[M])\begin{Bmatrix}U_f\\U_b\end{Bmatrix}=\begin{Bmatrix}0\\P_b\end{Bmatrix} \tag{4.34}$$

where the matrices $[A]$, $[B]$, $[G]$ and $[M]$ are the same matrices as defined in the eigenvalue problem, as shown in Equation (4.19), except that the dimension of the matrices are $(2n+2)$ x $(2n+2)$, since the motions at the interface between the layered system and the underlying halfspace are now taken into account. κ_a is the apparent wavenumber for the incident wave, as defined in Equation (4.27). U_f is the to-be-solved free field displacement vector in the layered system; U_b is the interface displacement vector; and P_b is the interface force vector. The vectors U_b and P_b each have two components, one for horizontal motion and one for vertical motion, and they define the influence of the incident waves upon the layered system. The vectors are dependent on the properties of the underlying halfspace, the incident angle, and the type of the impinging wave, and must be determined from case to case. The procedure used in determining U_b and P_b in GROUND2D is a variation of the technique developed by Chen et al (1981). The detailed formulation can be found there.

Solution of Equation (4.34) yields the free-field displacement vector $\{U\}_f$, which is defined along S. Assuming the x-coordinate of the reference curve at top

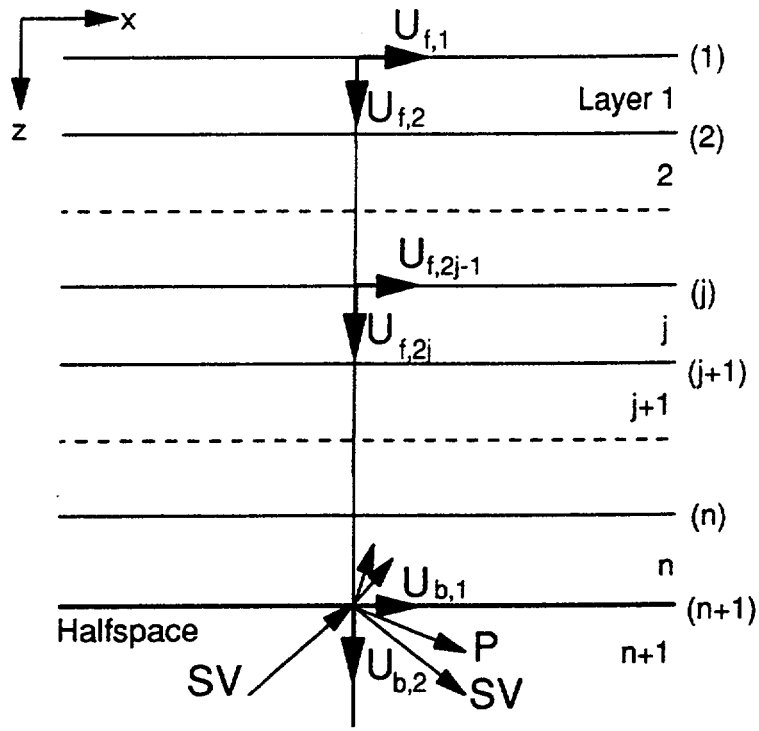

Figure 4.5: Wave-scattering in a layered system (after Chen, 1981).

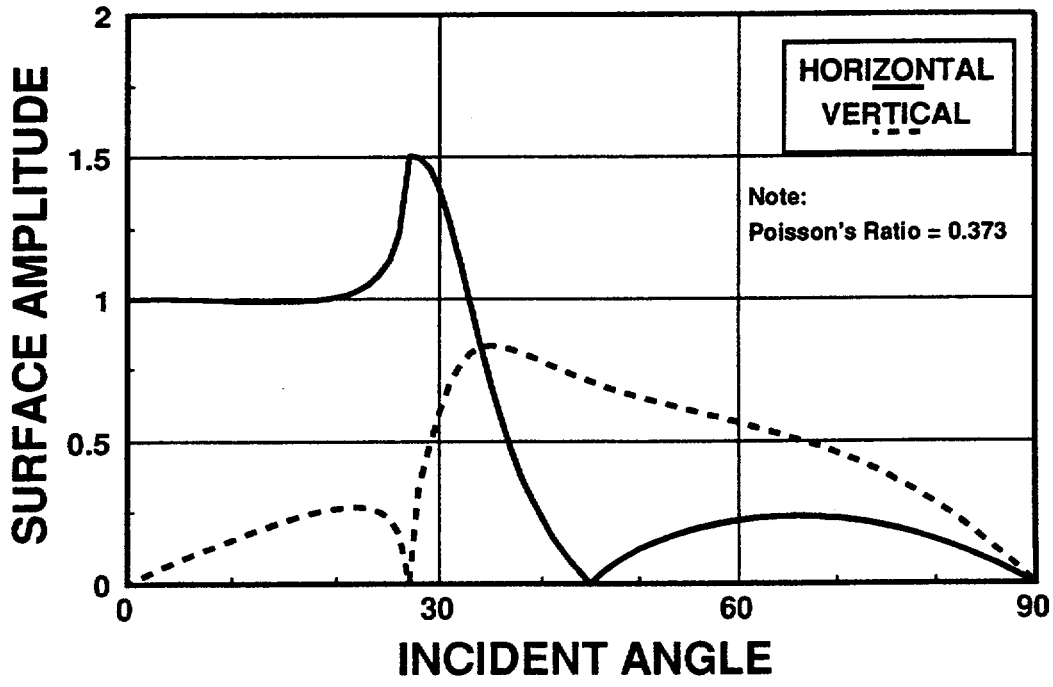

Figure 4.6: Variation of surface amplitude with incident angle.

of the layers is x_0, the free-field displacements along any curve which is parallel to the reference curve and at a distance x-x_0 can then be obtained using the relation

$$\{U(x)\}_f=\{U(x_0)\}_f\, e^{-ik_a(x-x_0)} \tag{4.35}$$

It is worthy to note that Equation (4.35) not only defines the free field motions along a curve which is parallel to the reference curve, it can also be used to determine the free field motions along any curves in the layered system, since the relationship defined in Equation (4.35) as a vector can also be applied for each individual term as well. Suppose it is necessary to determine the free field motions along S^* (see Figure 4.3) which is not parallel to the reference curve S. The vector defining the distances of the nodal points of the two curves is

$$\{\xi\}=\begin{Bmatrix}\xi_1\\ \xi_2\\ \xi_3\\ \vdots\\ \xi_n\end{Bmatrix}=\begin{Bmatrix}x_{1,1}-x_{0,1}\\ x_{1,2}-x_{0,2}\\ x_{1,3}-x_{0,3}\\ \vdots\\ x_{1,n}-x_{0,n}\end{Bmatrix} \tag{4.36}$$

The free-field displacement vector along S^*, $\{U(X_1)\}_f$ can then be determined as

$$\{U(X_1)\}_f=\begin{bmatrix} e^{-ik_a\xi_1} & & & & \\ & e^{-ik_a\xi_2} & & & \\ & & e^{-ik_a\xi_3} & & \\ & & & \ddots & \\ & & & & e^{-ik_a\xi_n}\end{bmatrix}\{U(X_0)\}_f \tag{4.37}$$

4.2.2 Inclined Out-of-Plane Waves (SH-Waves)

The free-field displacement vector $\{U\}_f$ due to SH-wave (out-of-plane) incidence can also be solved in the same way as the SV- and P-wave case. That is, to solve the equation

$$([A]\kappa_a^2+i[B]\kappa_a+[G]-\omega^2[M])\begin{Bmatrix}U_f\\U_b\end{Bmatrix}=\begin{Bmatrix}0\\P_b\end{Bmatrix} \tag{4.38}$$

where the matrices $[A]$, $[B]$, $[G]$ and $[M]$ are defined for the out-of-plane motion, and κ_a is the apparent wavenumber of the inclined SH-wave in the underlying halfspace. The determination of the terms of U_b and P_b is much simpler, however, because each term contains only one component. In fact, the interaction of the SH-wave at the interface of the layered system and the underlying halfspace can be represented by a simple viscous force.

4.3 SIMULATION OF SEMI-INFINITE HALFSPACE AT BASE

The approach described above was first developed for layered systems resting on a rigid base. A rigid base will reflect the scattered energy back into the system and will cause the site to have erroneous natural frequencies which will affect the overall response. This becomes especially critical for two-dimensional site response analysis. Since the model often covers a large distance, any small deviation from the true solutions is likely to be amplified. However, at some sites, soil layers may extend

to such a great depth that an artificial boundary must be introduced at a certain depth. The following two techniques are used in GROUND2D to remedy these problems in simulating the semi-infinite halfspace at the base of the layered system.

The first technique used in the program is to add some additional layers to the original model of the site. The total thickness, h, of the additional layers varies with frequency and is set to

$$h=1.5\frac{V_s}{f} \tag{4.39}$$

where f is the frequency of analysis in Hz, and V_s is the shear wave velocity of the underlying halfspace. The choice of this thickness is based on the observation that fundamental mode Rayleigh waves in a halfspace decay exponentially with depth and essentially vanish at a depth corresponding to one and a half wave length. Since the scattering motions generated due to the geometrical and geological irregularities in a site can be expressed as generalized surface wave motions, i.e., the generalized Rayleigh wave motions in the in-plane motion case, and higher modes usually decay faster than the fundamental mode, only minimal error is introduced by placing a rigid base at this depth. In GROUND2D, the total thickness of the layers is automatically adjusted according to the frequency under consideration, and all layers in the extended region are of uniform thickness. This type of discretization provides sufficient depth for the scattered motions to decay, and also allows the pathway of the incident wave be accurately modeled.

The second technique used in the program is to attach viscous dashpots at the base, thus the base becomes a viscous boundary instead of a rigid boundary. The

dashpots are formulated into the eigenvalue problem for each region, and Equation (4.19) becomes

$$([A]\kappa^2+i[B]\kappa+[G]-\omega^2[M]+[C_H])\{v\}=\{0\} \tag{4.40}$$

where, for out-of-plane motion,

$$[C_H]=diag\{0, ..., 0, i\omega\rho V_s\} \tag{4.41}$$

with dimensions $(n+1)$ x $(n+1)$; and for in-plane motions

$$[C_H]=diag\{0, ..., 0, i\omega\rho V_s, i\omega\rho V_p\} \tag{4.42}$$

with dimensions $(2n+2)$ x $(2n+2)$. V_s and V_p are the shear wave velocity and P-wave velocity of the halfspace, respectively; ρ is the mass density of the halfspace; and ω is the circular frequency. The mode vectors and wavenumbers are obtained by solving Equation (4.40), are usually different from the solutions of Eq.(4.19), and are used as the base in the computation of all the boundary matrices, the hyperelement matrices, and the mode superposition for expansion of the motions within a layered block region. Thus, the effect of the radiation damping of a perfect halfspace is built in.

Since the dashpot representation of the halfspace is only exact for the vertically propagating P- and S-waves, and the directions of the scattered motions are usually unknown, this technique is approximate in the sense that some of the scattered energy may still be able to bounce back into the system. However, the use of both techniques gives very satisfactory results in most practical problems.

4.4 INPUT GROUND MOTION

Ever since one-dimensional site response analyses became commonplace with the advent of readily available computer programs like SHAKE (Schabel et al, 1972), the ground motions used as input into the analyses are derived from a reference "outcrop" motion. That is, the data input into the computer program is the motion recorded on a rock outcrop. The actual motion used by these earlier programs at the base of the soil model is equal to 0.5 of the input "outcrop" motion, because for the vertically propagating waves considered by these programs, the amplitude of the incident wave is equal to 0.5 of the amplitude of the outcrop motion. The outcrop motion is assumed to occur on the surface of a homogeneous, isotropic halfspace.

The use of the outcrop motion as the reference motion for site response analyses is reasonable for analyses that do not consider inclined incident waves. The approach is also reasonable for inclined SH-waves. However, it has been shown (Lysmer et al, 1994) that for the same amplitude of the outcrop motion, the amplitude of incident P- and SV-wave is extremely dependent on the angle of incidence. An example of this relationship between incident angle and incident wave amplitude for a given outcrop motion is shown in Figure 4.6, after work performed by Knopoff (1957). This figure indicates that the amplitude of the incident wave back-calculated from a given outcrop motion can vary several-fold, depending on the incident angle. The most extreme case is for an incident angle of 45 degrees, where no horizontal surface motions are generated, thus leading to an incident wave amplitude of infinity. The effect of inclined incident waves is most noticeable at soil

sites, because as the seismic waves travel upward through less and less stiff materials, they tend to become more vertical due to Snells Law. Thus, by the time the seismic waves reach the ground surface, they may be near vertical and there is no reduction in surface amplitude due to hitting the free surface at an inclination.

Therefore, Deng et al. (1994) recommended that the amplitude of the incident wave, and not the outcrop motion, be used as the basis for analysis using inclined waves. In particular, the recommended amplitude of incident wave is that which would be backcalculated for a vertically propagating wave incident on a rock outcrop, which is the same amplitude as would be used in SHAKE. This procedure then allows the user to directly consider the effect of inclined incident waves without the added variable of incident wave amplitude.

4.5 GENERATION OF GROUND MOTIONS

After all boundary matrices, hyperelement matrices and load vectors are computed for a particular frequency, the global equations of motion are assembled according to Equation (4.20) and the final equations are solved. Since the use of the generalized boundary element and the generalized hyperelement greatly reduces the total degrees-of-freedom in the global equations, only an in-core active column solver is coded in GROUND2D. The solution process is repeated for each of the frequencies specified. All of the solution vectors, which consist of the displacements at all nodal points, and free field motions for all blocky regions in case of a body

wave incidence are stored in external files for post-processing to obtain required ground motions.

The post-processing of the nodal point solutions is an integral part of the solution process to generate necessary results due to the uniqueness of the analytical model adopted in the program. Three types of post-processing techniques are required, namely: (1) the spatial interpolation through modal superposition to extract the motions within blocky regions from nodal point solutions at each specified frequency; (2) the frequency domain interpolation through discrete Fourier wavenumber transform to obtain a continuous form of transfer functions at a specified point from solutions at discrete frequencies; and (3) the Fourier transform to convert frequency domain (steady state) solutions to time domain (transient state) solutions, or from transfer functions to acceleration time histories and acceleration response spectra, given a reference earthquake motion. Details of the three post-processing techniques can be found in Deng et al. (1994).

5. TOPOGRAPHIC EFFECTS

"...The effect of the vibration on the hard primary slate, which composes the foundation of the island, was still more curious: the superficial parts of some narrow ridges were as completely shivered as if they had been blasted by gunpowder. This effect, which was rendered conspicuous by the fresh fractures and displaced soil, must be confined to the near surface, for otherwise there would not exist a block of solid rock throughout Chile; nor is this improbable, as it is known that surface of a vibrating body is affected differently form the central part. It is, perhaps, owing to this same reason that earthquakes do not cause such terrific havoc within deep mines as would be expected..." (Charles Darwin, 1835).

5.1 BACKGROUND

The above quote by Darwin (Barlow, 1933) describing the effects of the February 20, 1835 Chilean earthquake suggests that topographic amplification of seismic motions is a phenomenon that has been well recognized for some time. Certainly, in the recent past, there have been numerous cases of observed earthquake damage pointing to topographic amplification as an important effect. As a result, a considerable amount of work has been done in an attempt to model, quantify, and predict these effects.

Some of the earliest experiments aimed at evaluating topographic amplification were performed by F. J. Rogers (Lawson, 1908) following the 1906 San Francisco earthquake. These early experiments were conducted with buckets of sand on a shaking table. Rogers observed vibrations on the top of the sand pile to be greater than those at the base. These results were later discussed by Reid (1910) who suggested that the observed effects could be the result of irregular reflections

and refractions in the immediate neighborhood of the slope. Similar experiments were repeated later by Goodman and Seed (1966) with comparable results.

The apparent effects of topographic amplification were observed by Celebi (1987) following the M_S=7.8 1985 Chile Earthquake. While four- and five-story buildings on ridgetops were extensively damaged, similar buildings in adjacent canyons suffered no damage. In addition, one- and two-story buildings along ridgetops suffered only minor damage. The concentration of damage along the ridgetops prompted the deployment of an array to measure possible topographic amplification.

The ridges in question were approximately 20 m in height with side slopes of 10 to 15 degrees. The seismograph stations were set on alluvial deposits or weathered granite, with care taken so that a station in the base of a canyon was set upon similar material as the station on the corresponding ridgetop. Aftershock data was then collected for a period of 5 months following the main shock.

Results were presented in the form of spectral ratios between the ridge crests and canyon bases for a frequency range of 0 to 10 Hz. These results indicated considerable frequency-dependent amplification, particularly in the range of 2 to 4 Hz, and 8 Hz. Spectral amplifications up to 10 and above were noted. Similar amplification was noted between the canyon station and a nearby reference station sited on bedrock. No consideration was given in the study for differences in soil amplification between the canyon and ridge sites.

Celebi (1991) presented additional evidence of topographic amplification observed in aftershock data following the 1983 Coalinga and 1987 Superstition Hills

earthquakes. A 3 station array (1 crest and 2 opposing gully stations) set across a ridge was able to record motions from a M_S=5.3 aftershock of the Coalinga event. The ridge was approximately 30 m high, with average side slopes of 10 to 15 degrees. The geology was described as weathered sandstone near the surface, with harder Pliocene sandstone at depth. Amplification was calculated between the crest and gully stations. Spectral amplifications of up to 10 were noted, with most amplification occurring between 1 and 6 Hz, and at 7.5 Hz. Eleven aftershocks of the 1987 Superstition Hills earthquake were recorded at the base and crest of Superstition Mountain. The mountain has side slopes of less than 5 degrees and the observed amplifications were as high as 20 in the 2 to 12 Hz range.

One of the first numerical studies of the effect of topography on seismic response was carried out by Boore (1972). This study, prompted by observations of high accelerations near Pacoima Dam during the 1971 San Fernando earthquake, considered the effect of simple topography on vertically propagating SH-waves. Boore noted that numerical models were necessary when considering steep slopes, or when the wavelength and size of topographic feature are similar (i.e. analytical solutions are not possible). Boore used the finite difference method to model 20 m high ridges with side slopes of 23 and 35 degrees. The medium was assumed to be homogeneous, isotropic, and linearly elastic. The shear wave velocity of the material was 500 m/s, and the frequency range under consideration was approximately 1 to 10 Hz. Damping values ranged from 2 to 20 percent, depending on the frequency. Since no layering was included in the model, the level of damping had little effect on the spectral ratios.

Boore concluded that the motion within the ridge consisted of 3 phases: a direct wave, a reflected wave, and a diffracted wave. The results showed that there was amplification at the ridge crest, and that both amplification and attenuation could occur along the side slopes, depending on the slope geometry and the frequency of motion. The effect of topography was found to vary with frequency, and amplification up to 100 percent was noted over the free-field. The amplification was found to decrease with slope angle and as the wavelength became large compared to the characteristic length.

Rogers et al. (1974) performed experiments using a physical model to study ridge effects on P-waves. Amplifications on the order of 50 percent were found on broadband input motion, and on the order of 200 percent on band limited input. When this data was compared to actual field measurements of ground motion (Davis and West, 1973), qualitative, but not quantitative, agreement was found. The field studies showed amplifications of 400 percent for peak velocities, and amplifications as high as 20 times in relative spectral velocity from base to crest.

May (1980) studied the effectiveness of vertical scarps on reducing the seismic energy transmitted to a site above or below the scarp. May used the finite element method to analyses horizontally propagating SH- and Love waves passing through 60- to 150-m high vertical scarps in a halfspace and a layer over a halfspace. The frequencies of motion considered ranged from 1.5 to 6 Hz. May found that refection off the scarp face played a large role in the response, and that the effect of the scarp could be related to the ratio of slope height, H, and the wavelength of the motion

under consideration. May performed tests using an instrumented granite block to validate his numerical model, and found a good comparison between the two models.

Geli et al. (1988) reviewed previous analytical studies of topographic amplification, which used the following methods: finite difference (Boore, 1972; Zahradnik and Urban, 1984), finite elements (Smith, 1975), integral equation method (Sills, 1978), boundary methods (Sanchez-Sesma et al., 1982), and discrete wavenumber methods (Bouchon, 1973, Bard, 1982). All of these studies considered the analysis of an isolated two-dimensional ridge on the surface of a homogeneous halfspace and all yielded consistent results: the amplification of acceleration of no more than 2 at the crest, peaking when the wavelength is about equal to the ridge width; and varying amplification and attenuation along the surface of the slope from the crest to the base. However, these results considerably under-estimate amplifications observed in the field, which mostly range from 2 to 10, and up to as much as 30. Geli et al. then analyzed a more detailed model configuration using a layered profile and introduced nearby ridge effects, but arrived at conclusions similar to those of the previous researchers. In addition, they found that neighboring ridges may have greater effect on site response than layering, and concluded that future models should be able to analyze SV- and surface waves and three dimensional geologic configurations.

Sitar and Clough (1983) used a two-dimensional finite element model to analyze the seismic response of steep slopes in weakly cemented sands. They found that accelerations tended to be amplified in the vicinity of the slope face. However, in contrast to Geli et al. (1991) they noted that these topographic effects tended to

be small relative to the amplification that occurs in the free field due to the site period.

Most recently, various methods of analyzing topographic effects were reviewed in an NSF/EPRI workshop (EPRI 1991). Recommendations resulting from the workshop include the need for instrumented sites to verify numerical analyses of topographic effects. It was also suggested that there is a need for simple, easy to measure parameters and empirical correction factors for determining topographic effects, since 2- and 3-dimensional modeling can become quite cumbersome.

5.2 ANALYSIS OF A STEPPED HALFSPACE

To determine the effect of a steep cliff on the dynamic response of a uniform visco-elastic material subject to out-of-plane (SH) waves and in-plane (SV) waves, a parametric study using the computer program GROUND2D has been performed as part of this study. For clarity, the definition of the wave types as used herein is illustrated in Figure 5.1. A SV-wave is the in-plane shear wave with displacement in the plane of the slope cross-section, i.e. within the plane shown in Figure 5.1. The SH-wave is the out-of-plane shear wave with displacement normal to the slope cross-section, i.e. out of the plane shown in Figure 5.1. These definitions are consistent with those commonly used for the case of a wave traveling normal to the slope face, i.e. in the plane of Figure 5.1.

The problem of a steep slope in a uniform visco-elastic material can be simplified to that of a stepped uniform halfspace. The analysis of this problem is

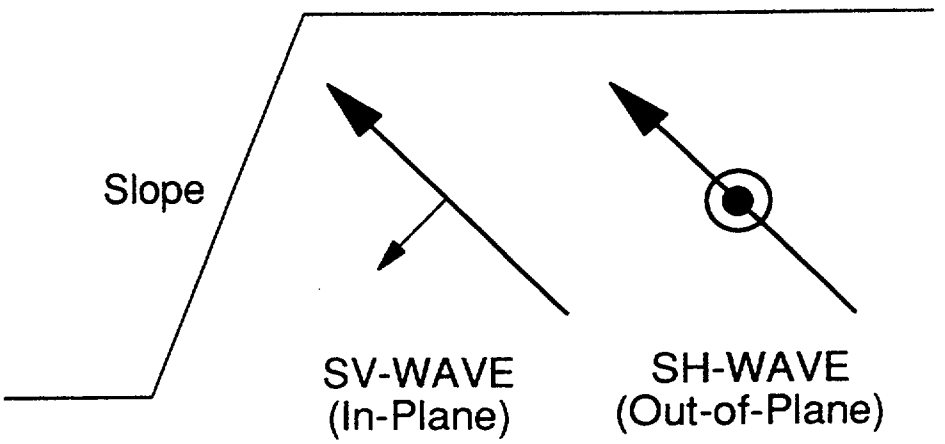

Figure 5.1: Definition of wave types used in study.

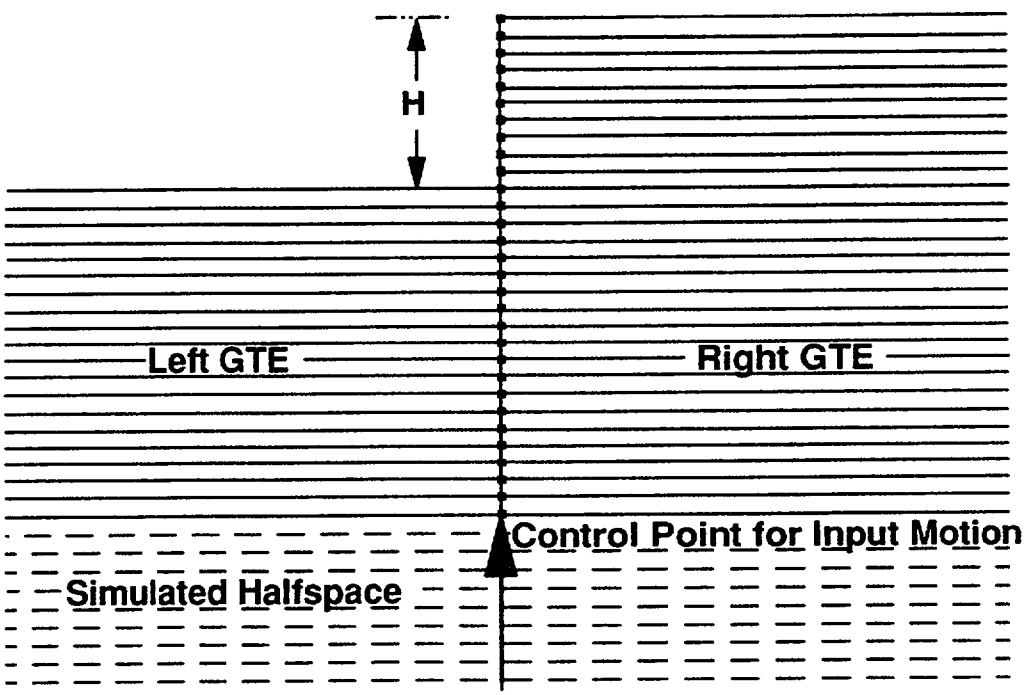

Figure 5.2: Stepped halfspace model for a vertical slope.

very useful for the development of an understanding of the fundamental parameters necessary to quantify the effect of topography on seismic response, because the only variables are the slope height and the wavelength. This allows the analysis to focus on the relationship between these two parameters without having to incorporate the natural frequency of the site. Once this relationship is examined, then other variables such as slope angle and wave inclination can be incorporated.

The development of the generalized hyperelement and the generalized transmitting element and their incorporation into GROUND2D make two-dimensional modelling relatively simple, particularly for steep slopes. To consider the effect of a slope on a uniform soil deposit, only a left and a right GTE are required, as shown in Figure 5.2.

The results of the analyses are presented as a function of H/λ, i.e. the ratio of the slope height and the wavelength of the motion under consideration. This definition of the normalized wavelength is in contrast to earlier studies of ridge effects (e.g. Boore, 1972; Geli et al., 1988) and dams (e.g. Gazetas and Dakoulas, 1993), in which the correlation was made between the wavelength and the width of the topographic feature, but is similar to the "dimensionless frequency" proposed by Dakoulas (1993) for the study of SH-waves in earth dams.

5.2.1 Effect of SH- (Out-of-Plane) Waves on a Vertical Slope

The effect of vertically propagating SH-waves on the seismic response of a vertically stepped halfspace is evaluated in the frequency domain over the range of

0.5 to 10 Hz. The uniform halfspace has a shear wave velocity of 300 m/s, a Poisson's Ratio of 0.3, and the fraction of critical damping ranging from 1 to 20 percent. The height of the slope is 30 m.

The results are presented in the form of transfer functions for the normalized frequencies of motion, and in terms of the amplification of the free field motion behind the crest. The transfer function is the multiple required to transfer the input motion, at a given frequency, from the control point in Figure 5.2, to the output motion at the point of interest. The actual transfer function is a complex number which accounts for the phase difference between the motions; however, only the magnitudes of the transfer functions are needed to compare the amplification of motion. The frequency range of 0.5 to 10 Hz includes the typical range of engineering interest and spans the range of dominant frequencies most often observed in large earthquakes.

The results of the analyses are presented in Figures 5.3 through 5.6, for damping values of 1, 5, 10, and 20 percent, and for distances varying from the slope crest to 4H behind the slope crest. The transfer functions plotted in Figures 5.3a through 5.6a show that increased damping significantly reduces the response of the free-field and of the slope, particularly at higher frequencies. The transfer functions also show that the effect of the slope is more pronounced at low levels of damping.

A comparison of the amplification of the free field motion at various distances behind the slope (Figures 5.3b through 5.6b) shows that damping does not greatly affect the amplification, though the amplification decreases slightly with increased damping. Again, the effect of damping is more pronounced at higher frequencies.

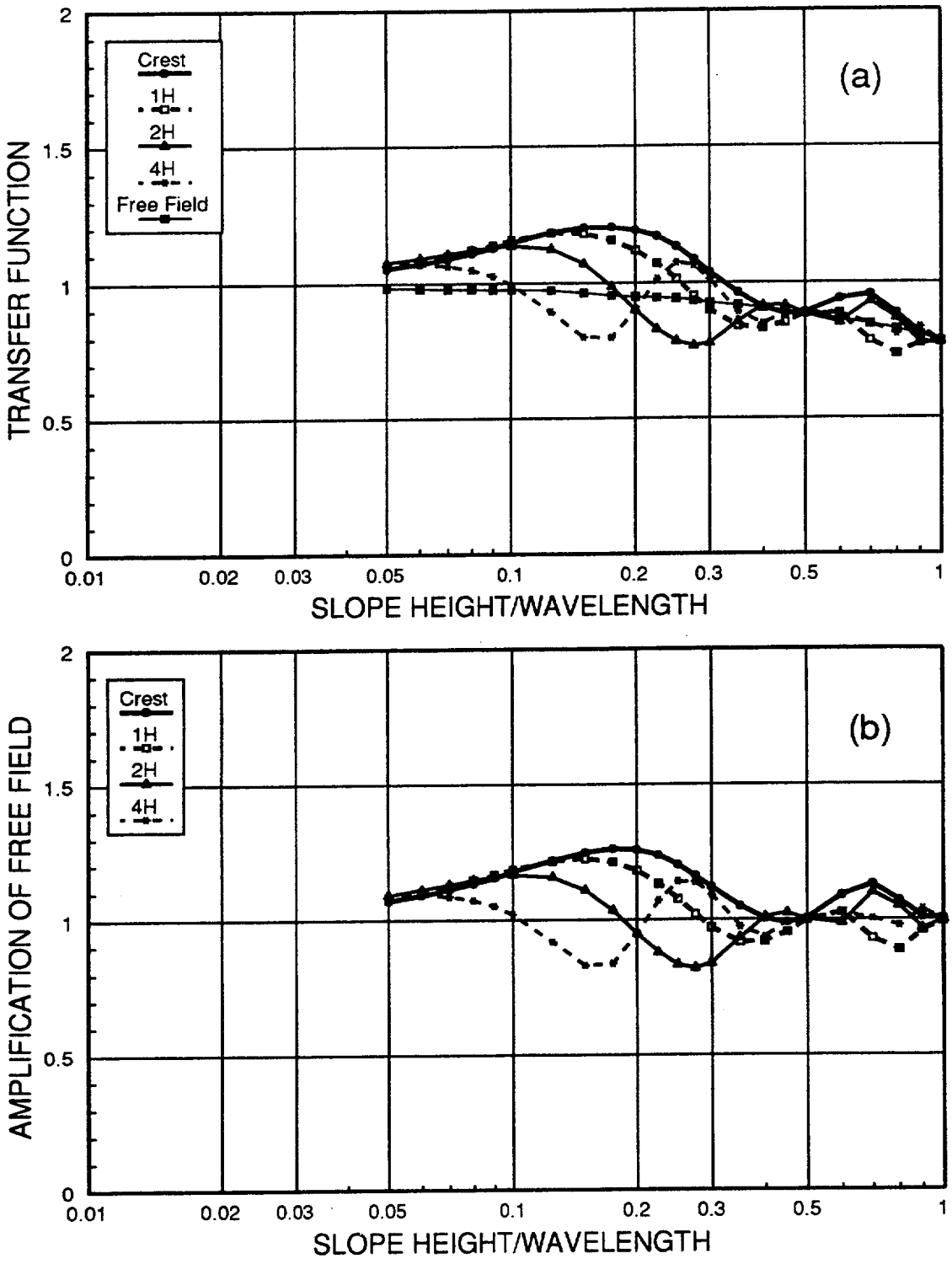

Figure 5.3: Horizontal transfer functions (a) and amplifications (b) for vertically incident SH-wave on a stepped halfspace for various distances behind crest, β = 1%.

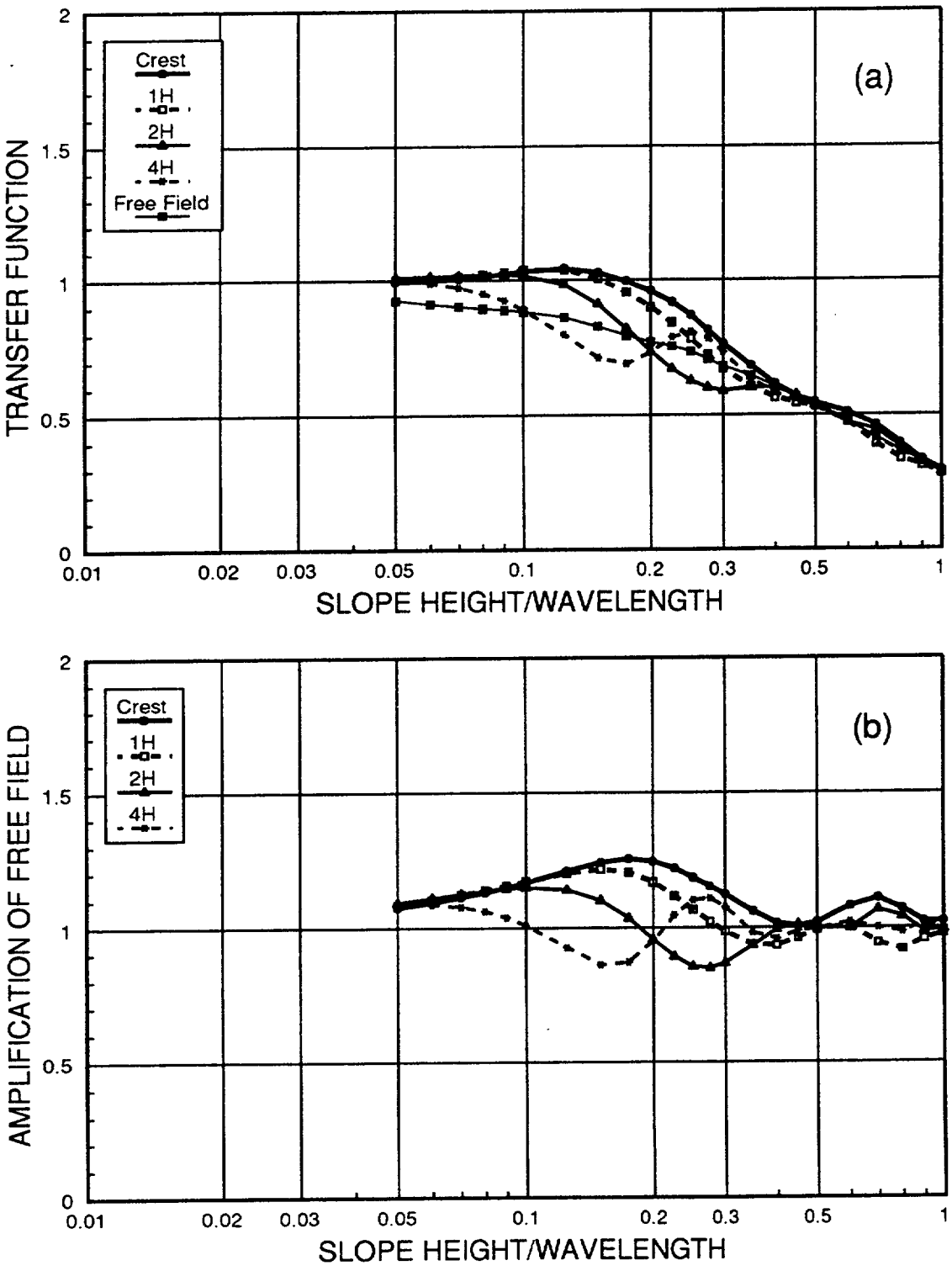

Figure 5.4: *Horizontal transfer functions (a) and amplifications (b) for vertically incident SH-wave on a stepped halfspace for various distances behind crest, β = 5%.*

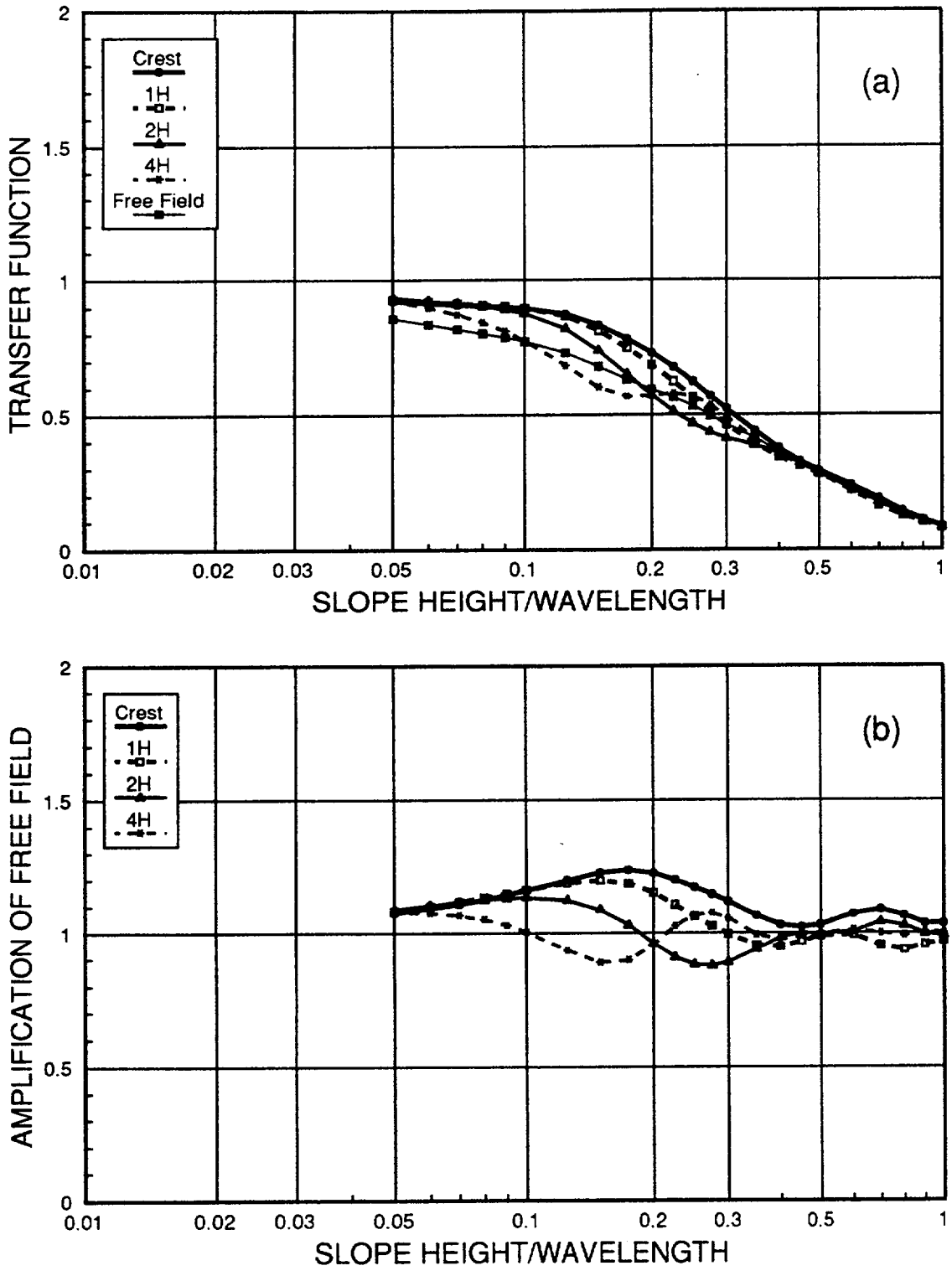

Figure 5.5: Horizontal transfer functions (a) and amplifications (b) for vertically incident SH-wave on a stepped halfspace for various distances behind crest, β = 10%.

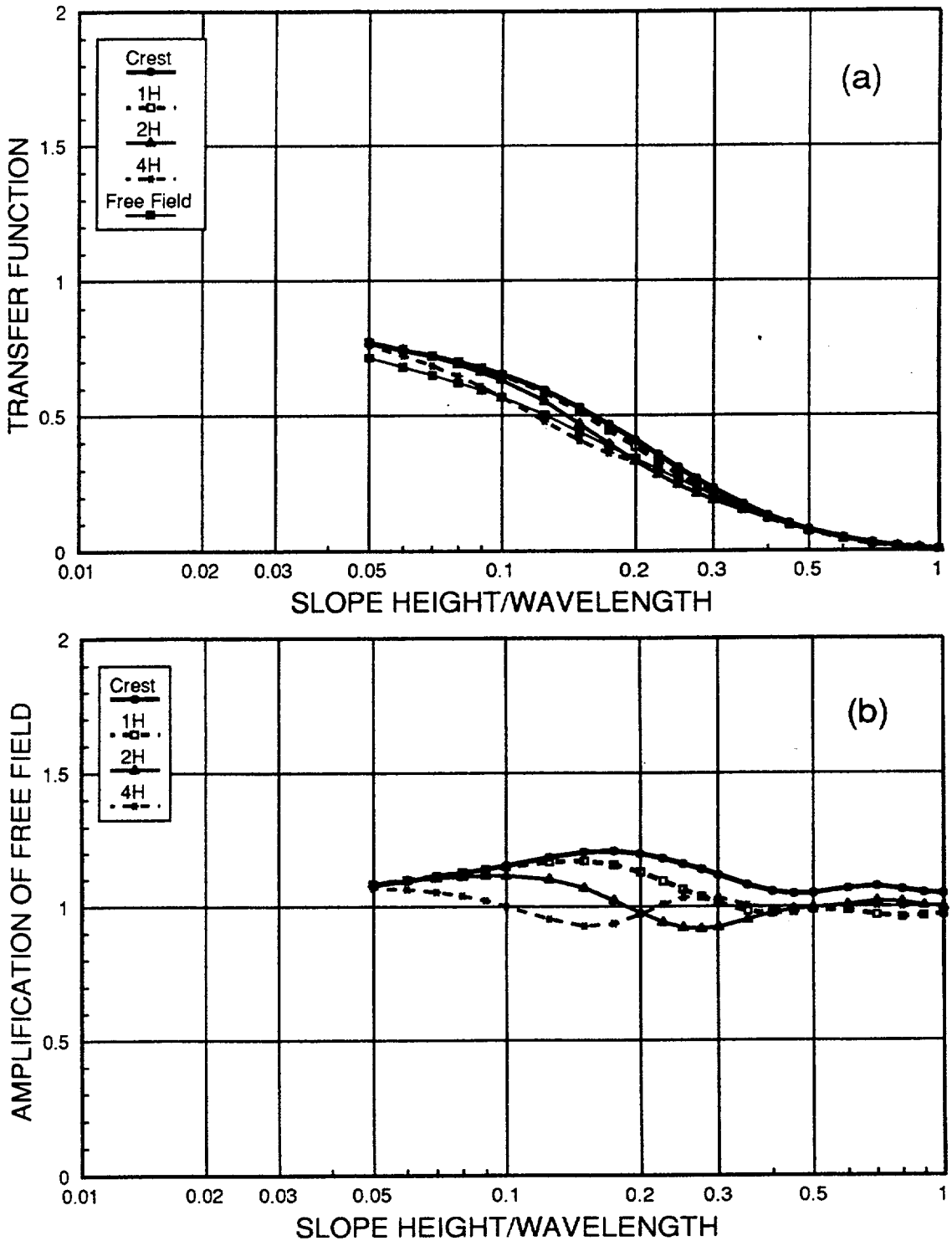

Figure 5.6: Horizontal transfer functions (a) and amplifications (b) for vertically incident SH-wave on a stepped halfspace for various distances behind crest, β = 20%.

Looking only at the amplification at the crest, a peak amplification of nearly 30 percent occurs at approximately $H/\lambda = 0.2$, a secondary peak of 15 percent at about $H/\lambda = 0.7$, and a null at $H/\lambda = 0.45$. The peaks correspond somewhat to the natural frequency of the soil column behind the crest for the height of the slope, which would occur at $H/\lambda = 0.25$ and $H/\lambda = 0.75$ for the first and second modes. This implies that the relationship between the slope height and the shear wave velocity of the soil behind the slope is very important in quantifying the effect of topography. The two peaks are seen at all levels of damping, though the peaks appear to shift to slightly lower values of H/λ with increased damping.

The magnitude of the amplification decreases away from the slope crest, primarily as a function of damping. The peak amplification seems to decrease and occur at a lower frequency with increasing distance from the crest, though in any case, the amplification is on the order of 15 to 20 percent of the free field motion. In addition, attenuation occurs at certain frequencies with increasing distance from the crest. At low values of H/λ, where the topographic step is small compared to the wavelength, the slope has little effect on the response.

5.2.2 Effect of SV- (In-Plane) Waves on a Vertical Slope

For the analysis of the response to SV-waves, both a horizontal and vertical component need to be considered. Since the input motion only consists of horizontal motion, the transfer functions for the vertical response are given relative to the

horizontal input motion, and the vertical amplification is relative to the free field horizontal response.

The results of the horizontal response due to SV-waves are shown in Figures 5.7 through 5.10 for frequencies ranging from 0.1 to 10 Hz ($H/\lambda = 0.01$ to 1.0). Considering first the horizontal response, the results are similar to those obtained for the SH-waves. The first peak amplification occurs at $H/\lambda = 0.2$, and the second peak occurs at $H/\lambda = 1.0$. For all levels of damping, the magnitude of both amplification peaks are on the order of 50 percent, which is higher than those observed for SH-waves, the second peak significantly so. However, as with SH-waves, increased damping significantly reduces the response at higher frequencies, so the second peak has a lesser importance in the overall response at higher damping levels. The pattern of attenuation and amplification with increasing distance away from the slope is also similar to the SH-wave case, though the magnitudes are greater for the SV-case.

The results showing the vertical response are presented in Figures 5.11 through 5.14. The vertical response is most pronounced at the crest of the slope, and at $H/\lambda > 0.2$, it is greater than the free field horizontal response. The amplitude at the crest does not seem to be effected by damping. The amplification of the vertical response away from the crest is never greater than about 50 percent the free field motion, and decreases with increased damping. Finally, it appears that the amplitude of the vertical response at the crest tends to increase with increasing frequency, and seems to be independent of the horizontal response at frequencies above $H/\lambda > 0.2$.

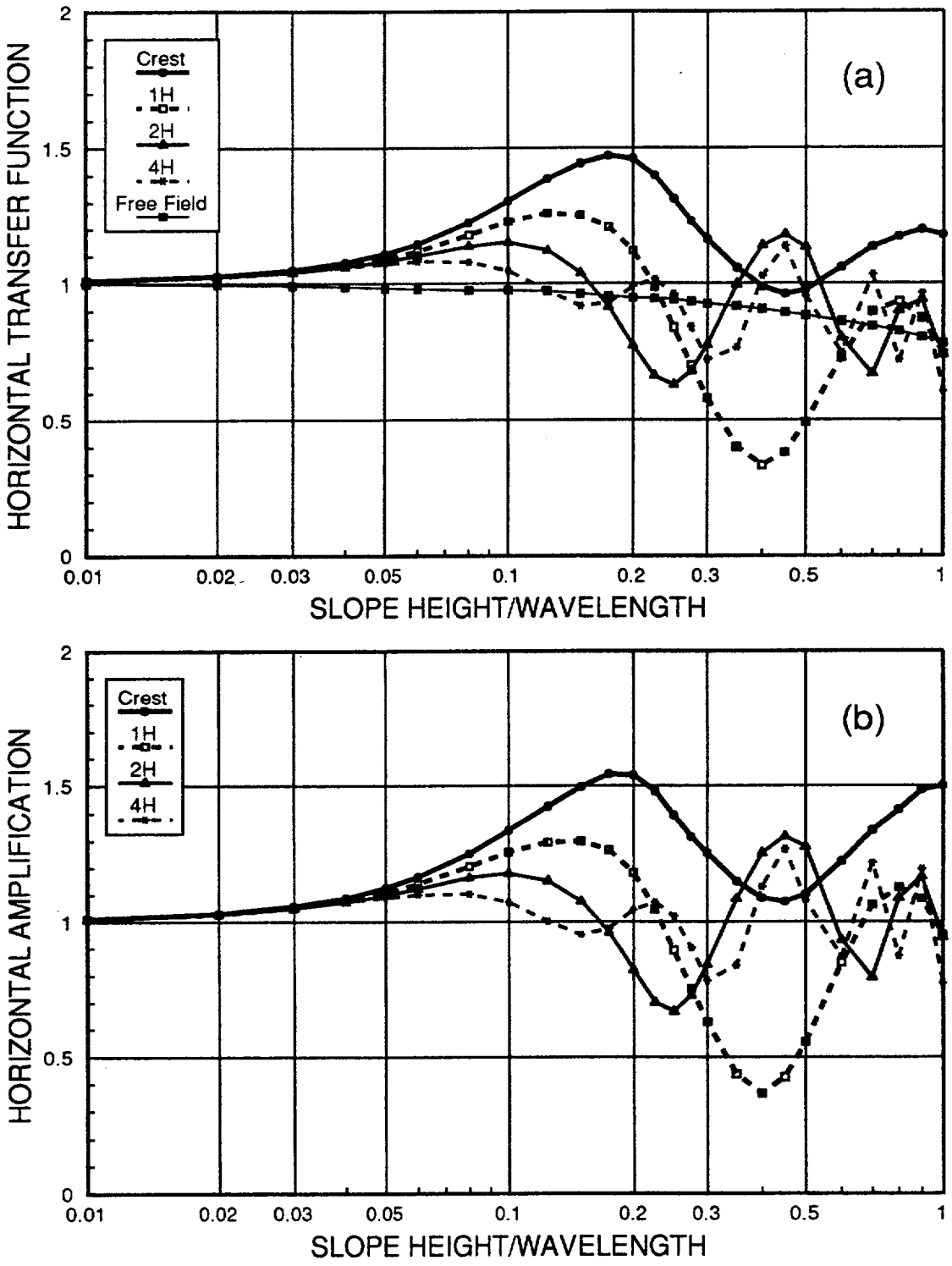

Figure 5.7: Horizontal transfer functions (a) and amplifications (b) for vertically incident SV-wave on a stepped halfspace for various distances behind crest, β = 1%.

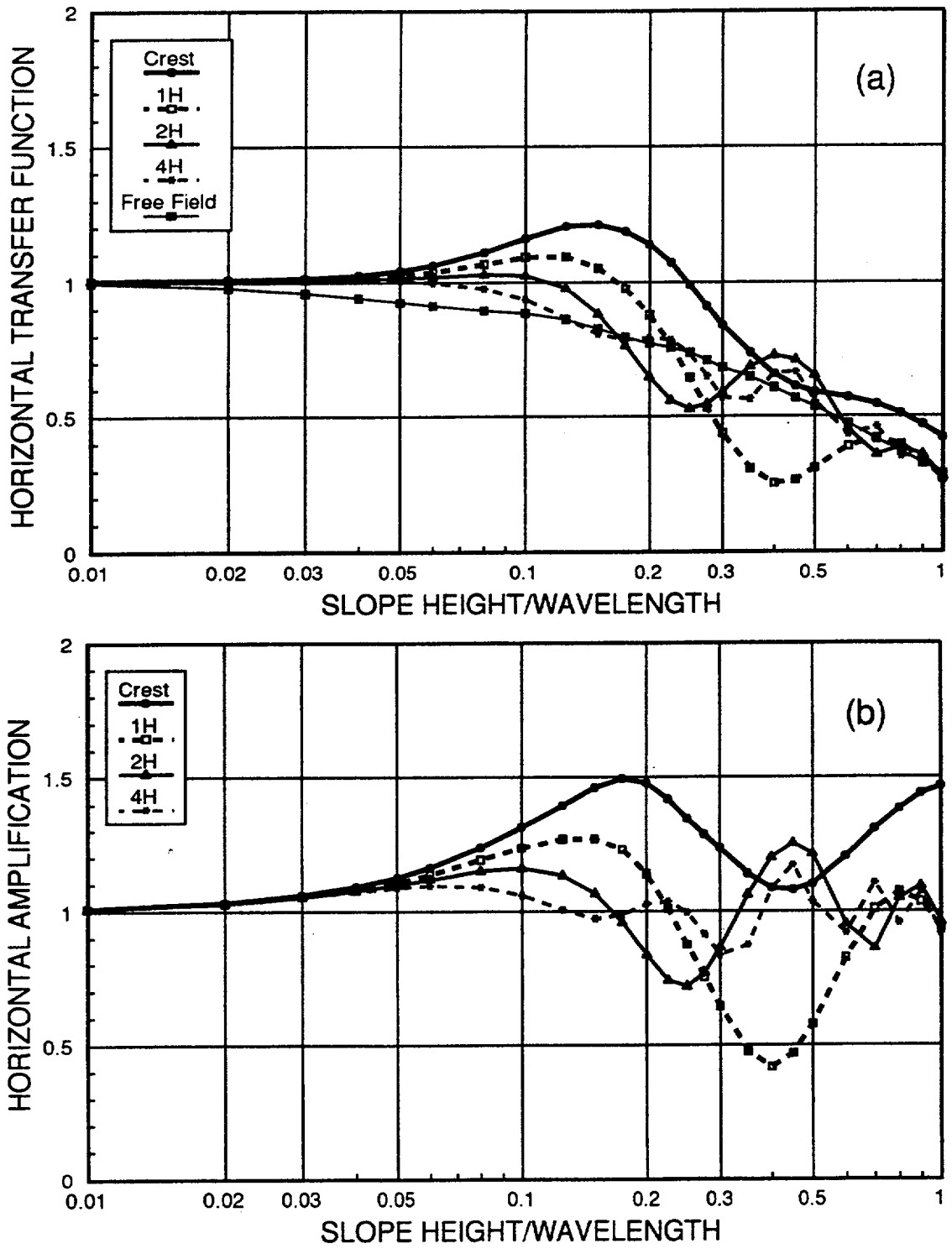

Figure 5.8: Horizontal transfer functions (a) and amplifications (b) for vertically incident SV-wave on a stepped halfspace for various distances behind crest, β = 5%.

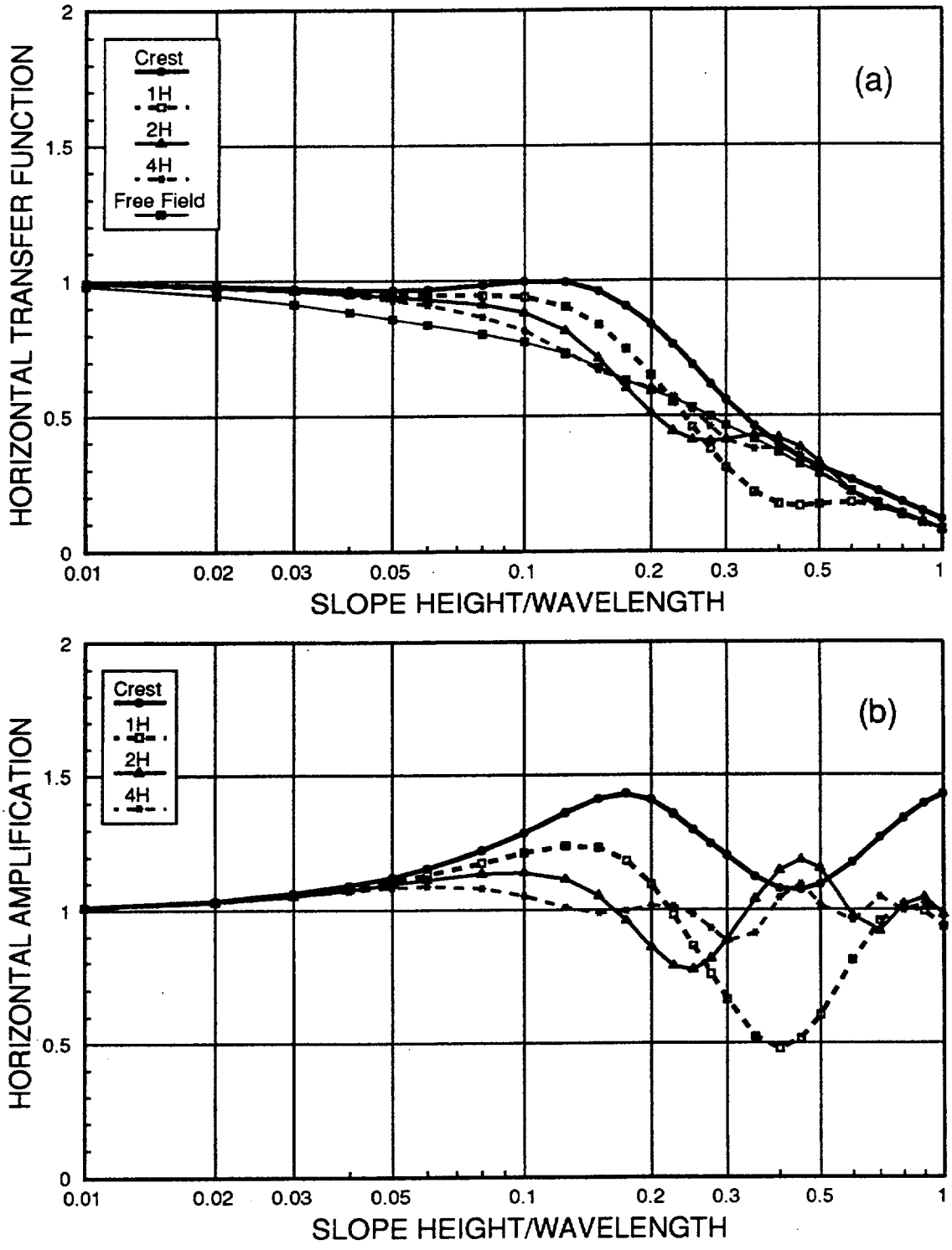

Figure 5.9: Horizontal transfer functions (a) and amplifications (b) for vertically incident SV-wave on a stepped halfspace for various distances behind crest, β = 10%.

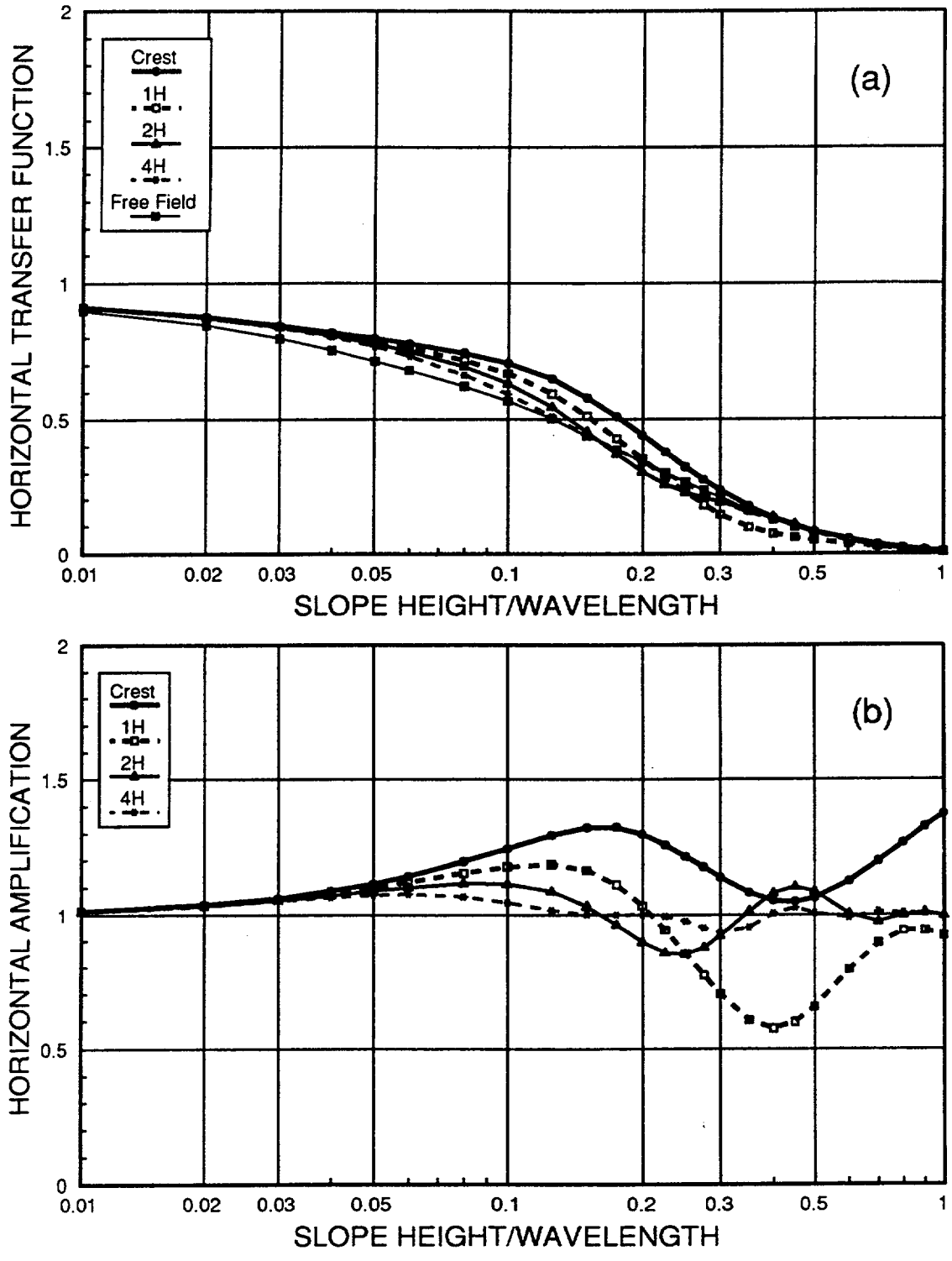

Figure 5.10: Horizontal transfer functions (a) and amplifications (b) for vertically incident SV-wave on a stepped halfspace for various distances behind crest, β = 20%.

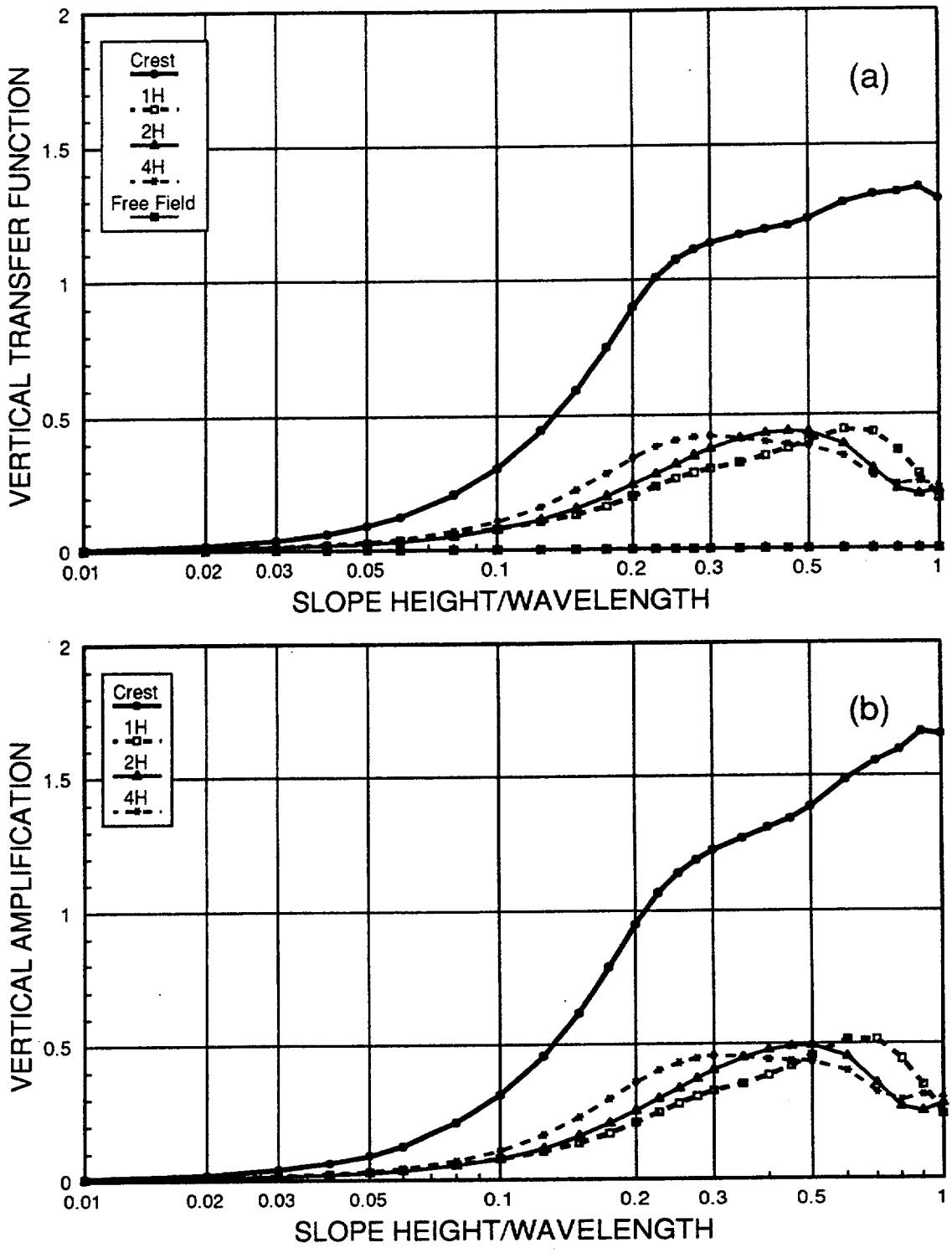

Figure 5.11: Vertical transfer functions (a) and amplifications (b) for vertically incident SV-wave on a stepped halfspace for various distances behind crest, β=1%.

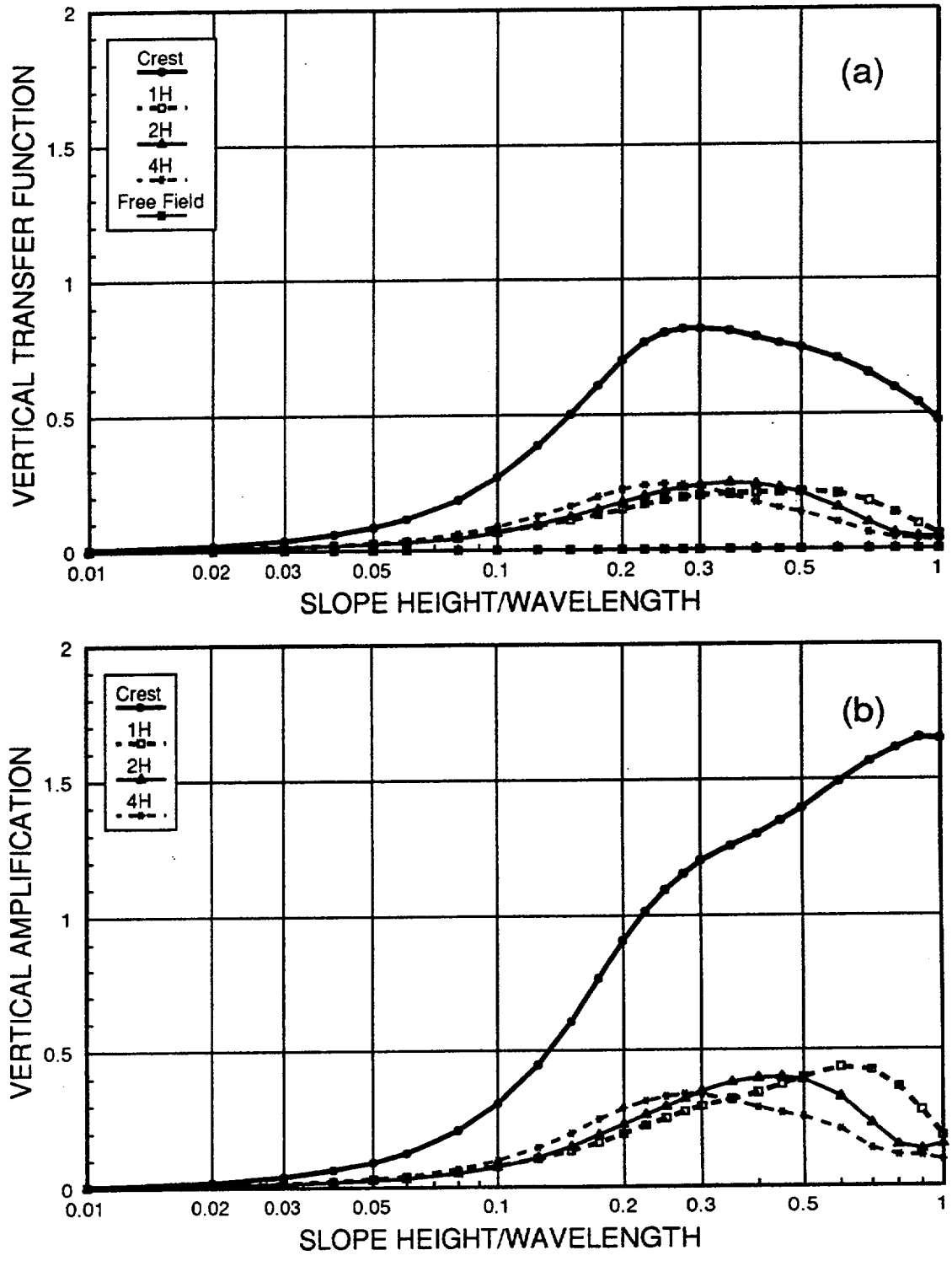

Figure 5.12: Vertical transfer functions (a) and amplifications (b) for vertically incident SV-wave on a stepped halfspace for various distances behind crest, β=5%.

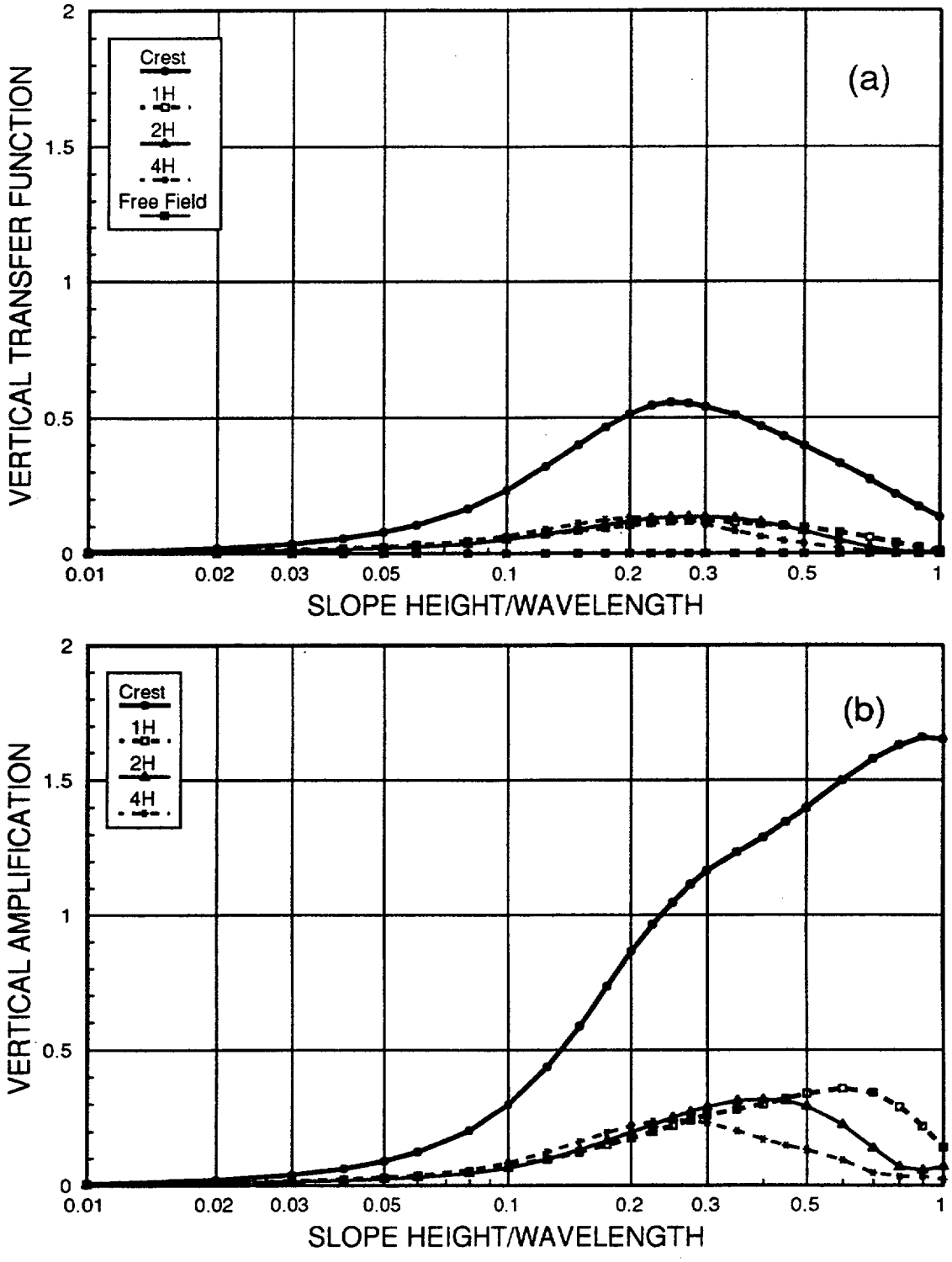

Figure 5.13: Vertical transfer functions (a) and amplifications (b) for vertically incident SV-wave on a stepped halfspace for various distances behind crest, β=10%.

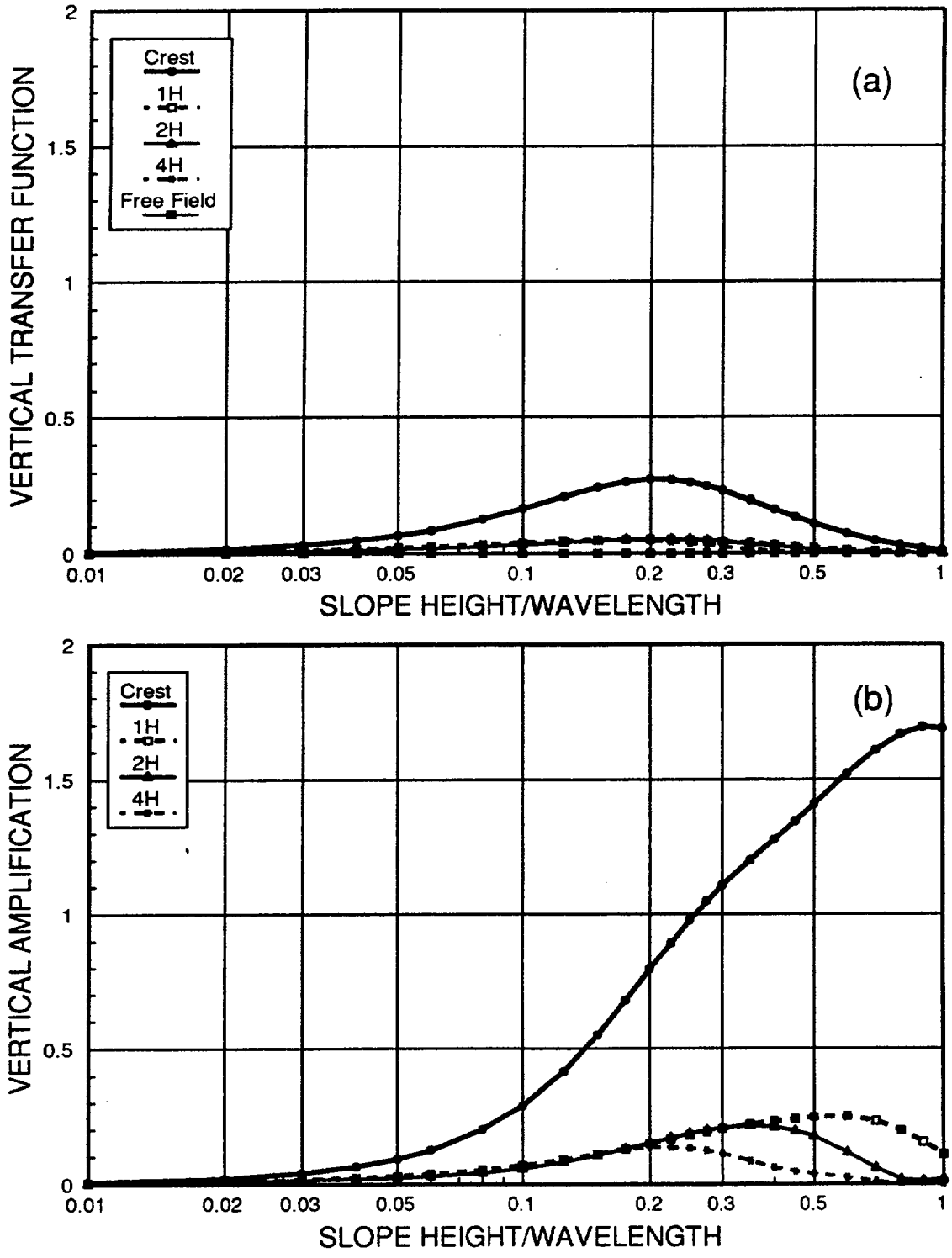

Figure 5.14: Vertical transfer functions (a) and amplifications (b) for vertically incident SV-wave on a stepped halfspace for various distances behind crest, β=20%.

5.2.3 Effect of Slope Angle

The effect of slope angle on topographic amplification was considered by varying the slope angle, S, as shown in Figure 5.15. Since steep slopes are the subject of this study, only slopes between 45 and 90 degrees were considered (30 and 90 degrees for SV-waves). The slope-crest amplification of the SH-wave free field motion is shown in Figure 5.16. With decreasing slope angle, the magnitude of the amplification at the first peak decreases from about 25 percent to about 15 percent, while the response at higher frequencies tends to increase to about 50 percent, with no apparent second peak. The horizontal response due to SV-waves is shown in Figure 5.17. In general, the magnitude of the amplification decreases with decreasing slope angle, from about 55 percent to about 15 percent, for $H/\lambda < 0.4$. Results at higher frequencies, above $H/\lambda = 0.4$, indicate no clear trend. The vertical response due to SV-waves is presented in Figure 5.18. Again, the vertical response decreases with decreasing slope angle.

5.2.4 Effect of the Incident Angle

The effect of varying the incident angle of SV-waves has until recently been a subject of little understanding. With the development of GROUND2D, the analysis of inclined SV-waves is made relatively easy, and provides us with an opportunity to consider their effect on the seismic response of steep slopes. Though our ability to determine the angle of incidence for the purposes of a site-specific stability analysis

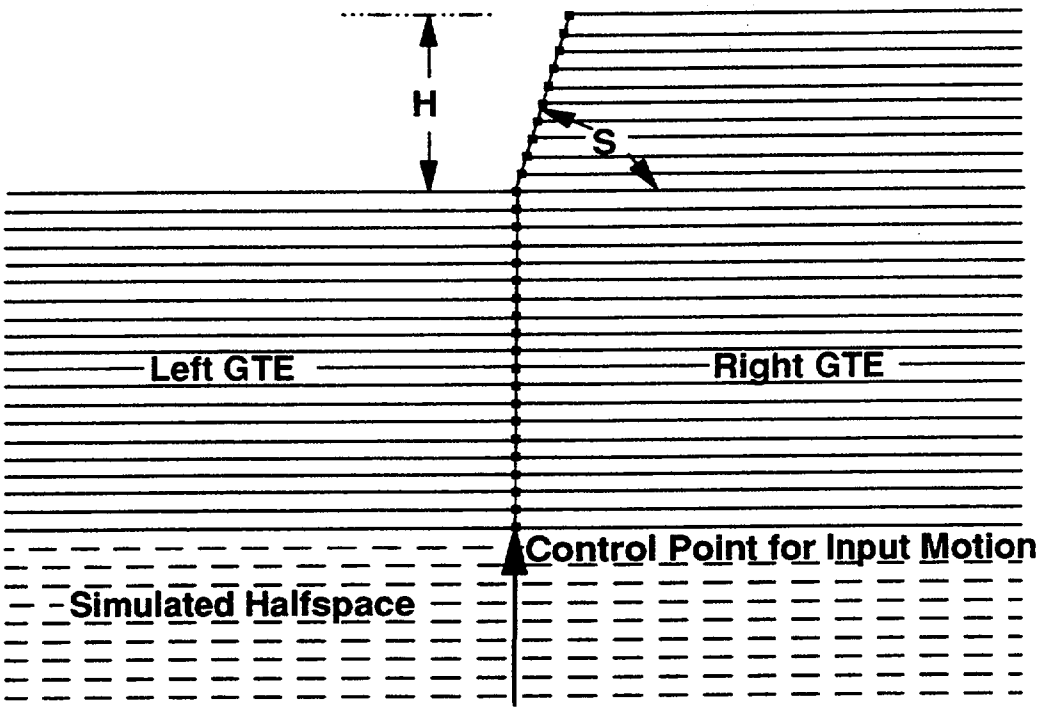

Figure 5.15: Stepped halfspace model for an inclined slope.

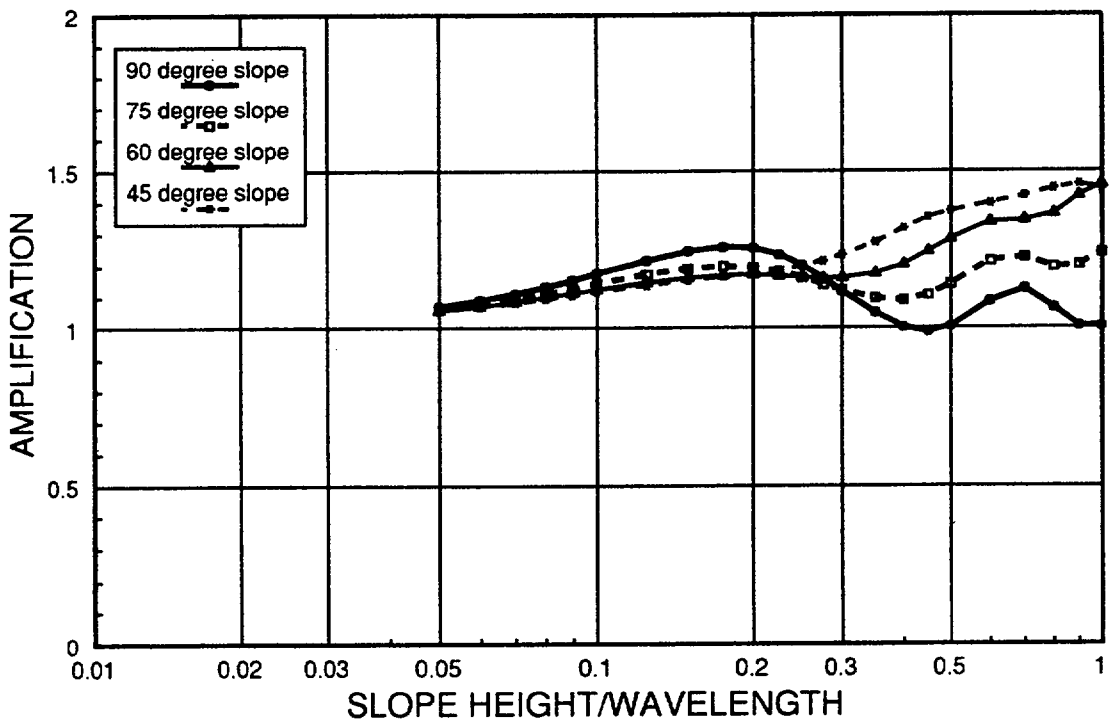

Figure 5.16: Horizontal amplification at the crest for a vertically incident SH-wave on an inclined slope, β = 1%.

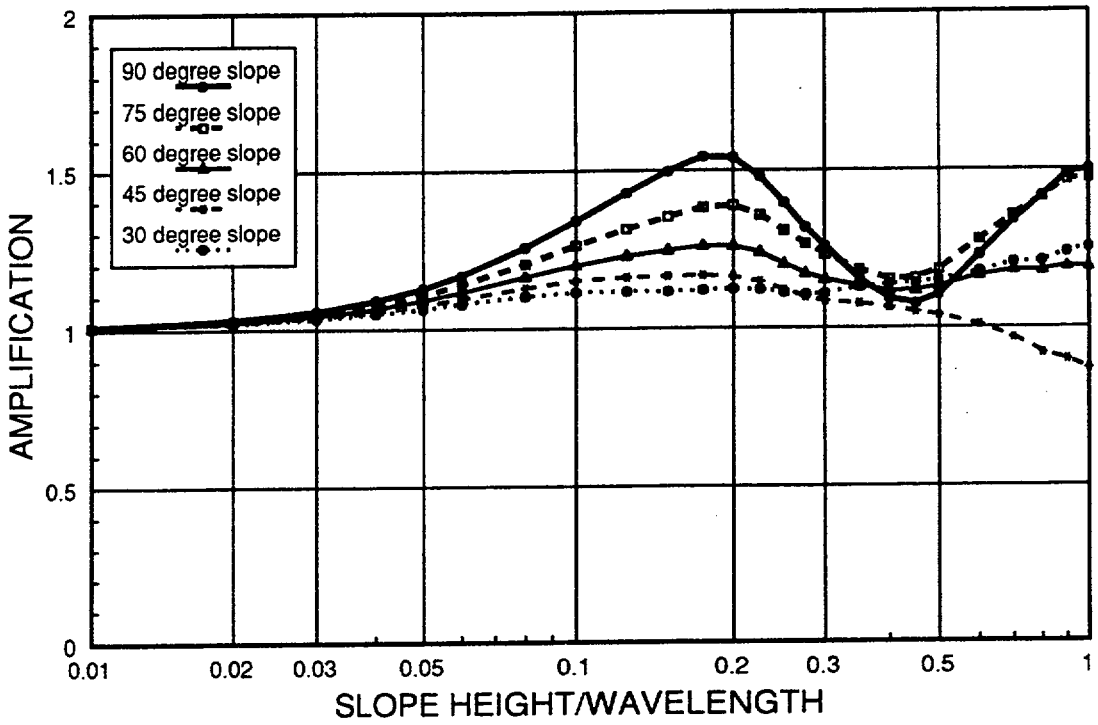

Figure 5.17: Horizontal amplification at the crest for a vertically incident SV-wave on an inclined slope, β = 1%.

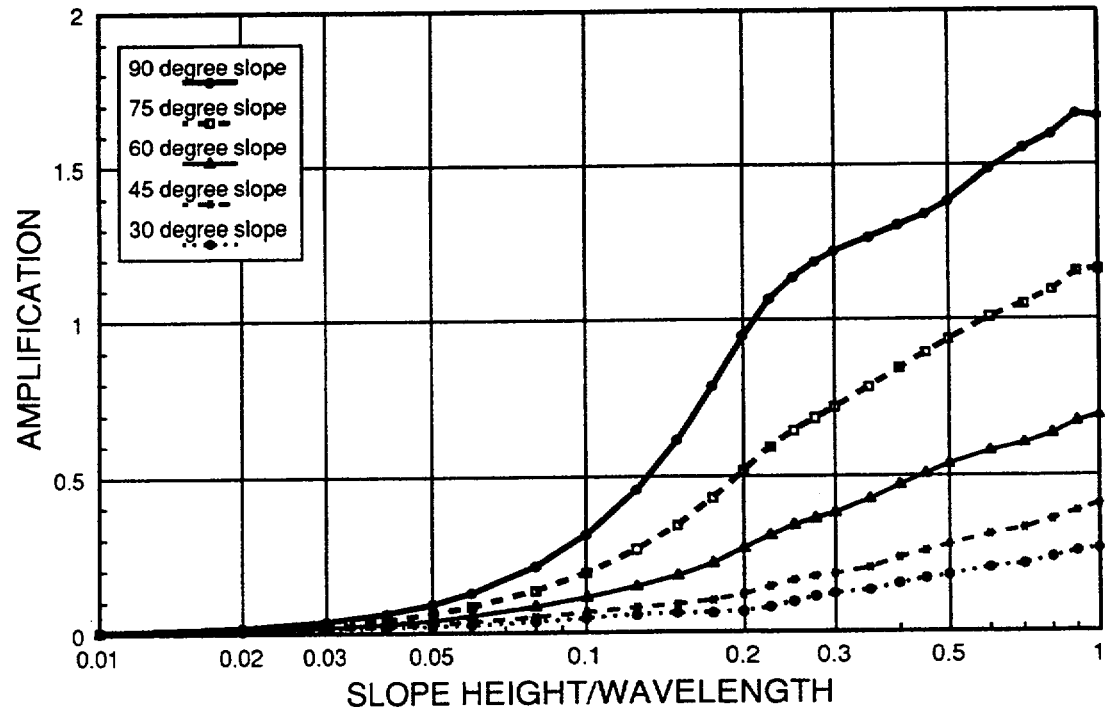

Figure 5.18: Vertical amplification at the crest for a vertically incident SV-wave on an inclined slope, β = 1%.

of an actual slope is questionable, the purpose of the analyses presented herein is to determine if the incident angle is, in fact, important to the response.

The angle of incidence, F, is measured clockwise from the z-axis (Figure 5.19). Waves with positive incident angles will be referred to as travelling away from the slope, and those with negative incident angles are referred to as travelling into the slope. The model characteristics are the same as previously analyzed, with damping equal to 1 percent, and the angle of incidence ranging from +30 to -30 degrees.

The response to SH-waves is presented in Figures 5.20 through 5.23. In each case, the response due to the wave traveling into the slope is greater than for the wave angle traveling away from the slope. For all angles considered, waves traveling into the slope result in greater amplification than for vertically propagating waves, and this effect increases with increasing frequency. The opposite is true for waves traveling away from the slope. The motion is attenuated with increasing incident angle, and the attenuation increases with frequency.

Similar results are obtained for the horizontal component of the SV-wave response, presented in Figures 5.24 through 5.27. However, in contrast, the direction of wave propagation appears to make little difference in the vertical response to SV-waves. Although, there is a notable increase in the vertical response due to SV-waves at low frequencies, which increases with incident angle independent of the direction of propagation due to wave splitting on the free surface. An SV-wave of amplitude 0.5 incident on a free surface will result in both horizontal and vertical motions, depending on Poisson's ratio, as shown in Figure 4.6. For material with a Poisson's

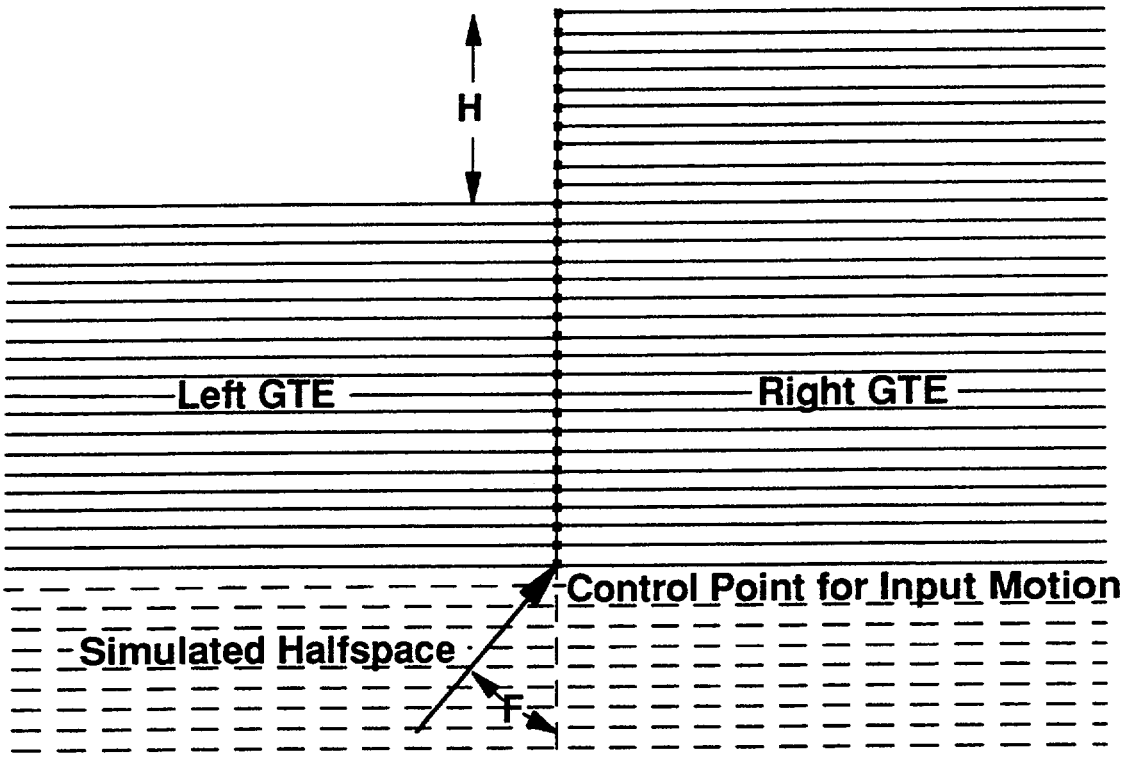

Figure 5.19: Stepped halfspace model for inclined wave incident on a vertical slope.

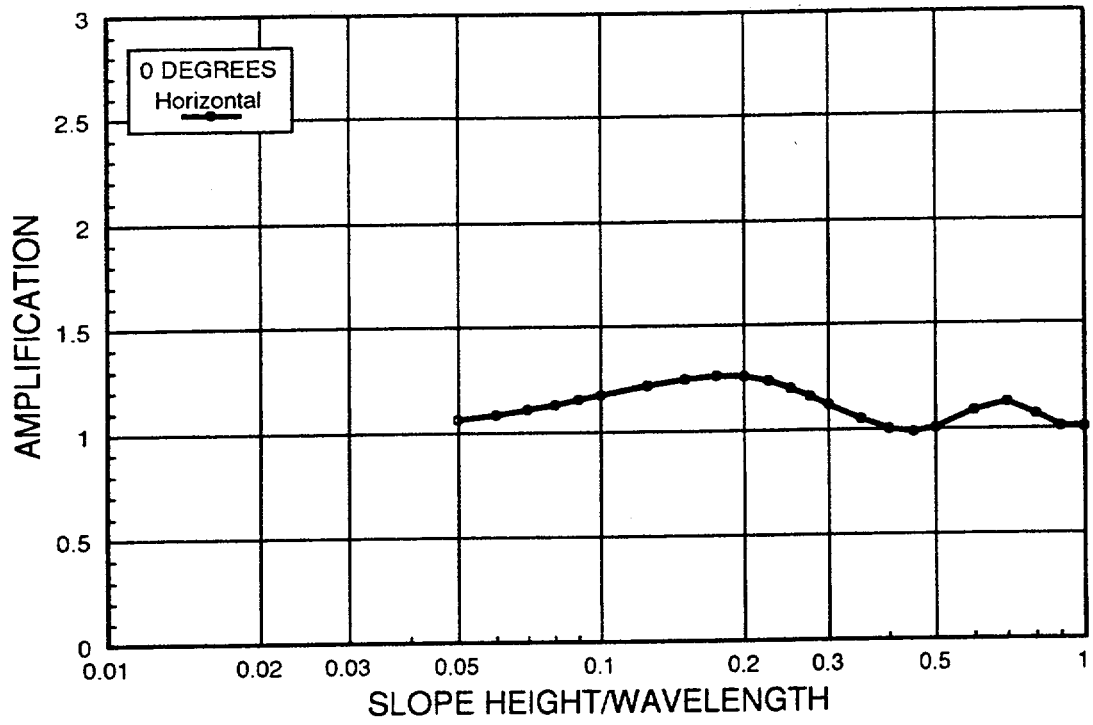

Figure 5.20: Amplifications at the crest for inclined SH-wave incident on a vertical slope, F = 0°, β = 1%.

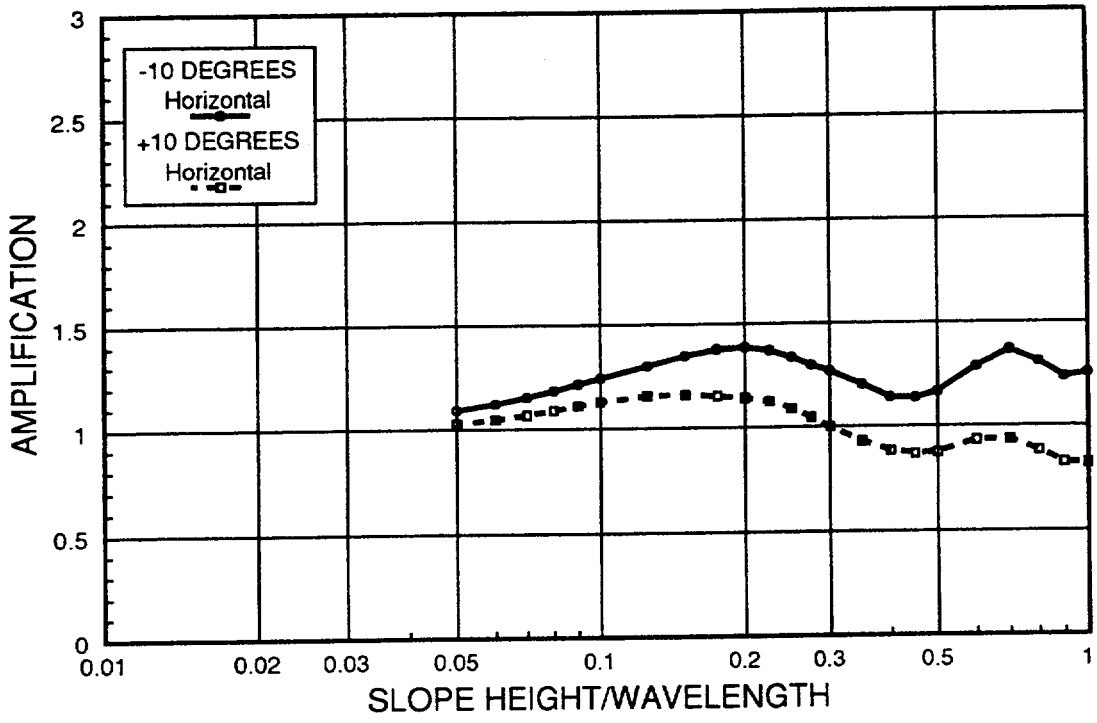

Figure 5.21: Amplifications at the crest for inclined SH-wave incident on a vertical slope, F = -10° and +10°, β = 1%.

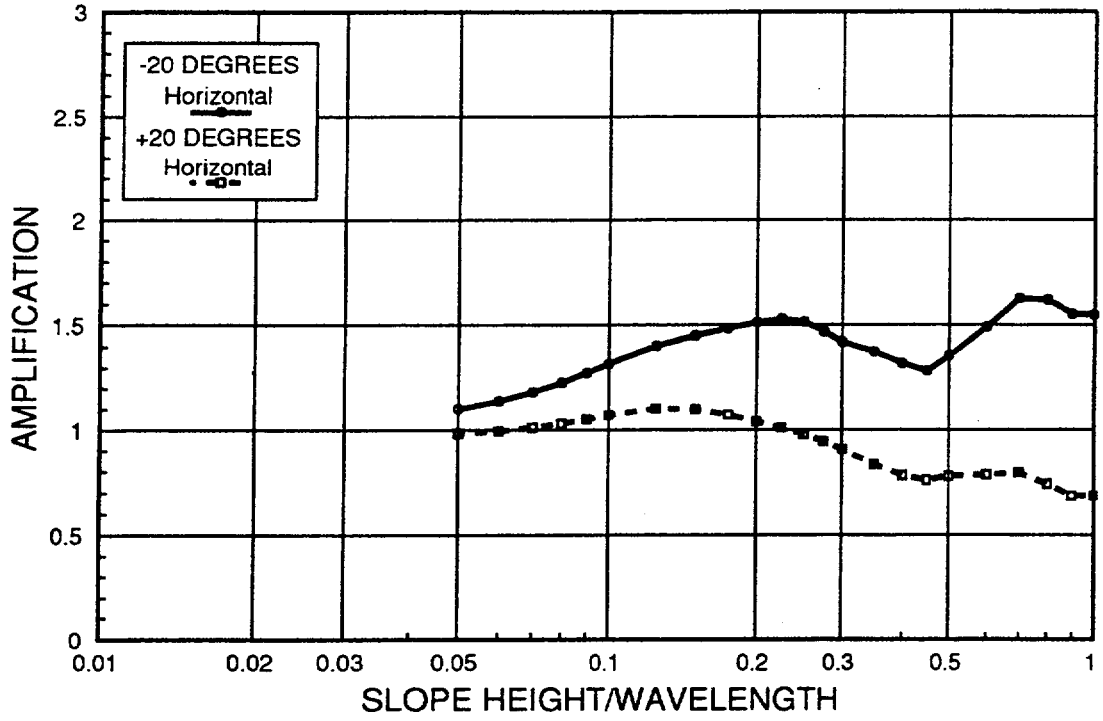

Figure 5.22: Amplifications at the crest for inclined SH-wave incident on a vertical slope, F = -20° and +20°, β = 1%.

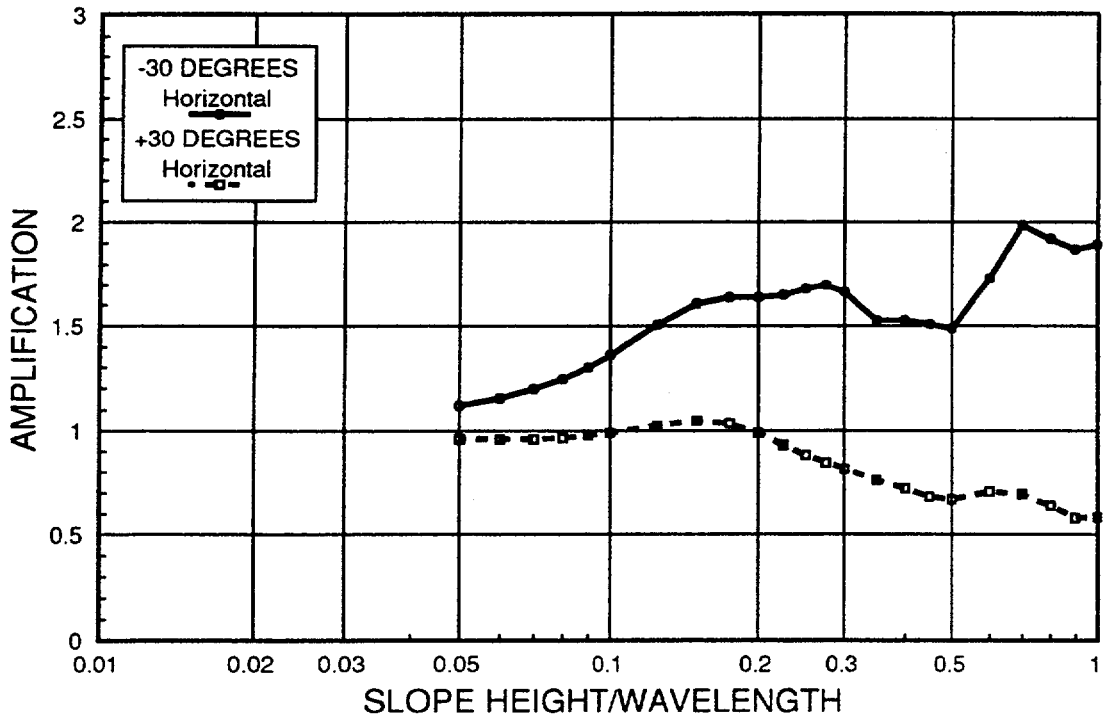

Figure 5.23: Amplifications at the crest for inclined SH-wave incident on a vertical slope, F = -30° and +30°, β = 1%.

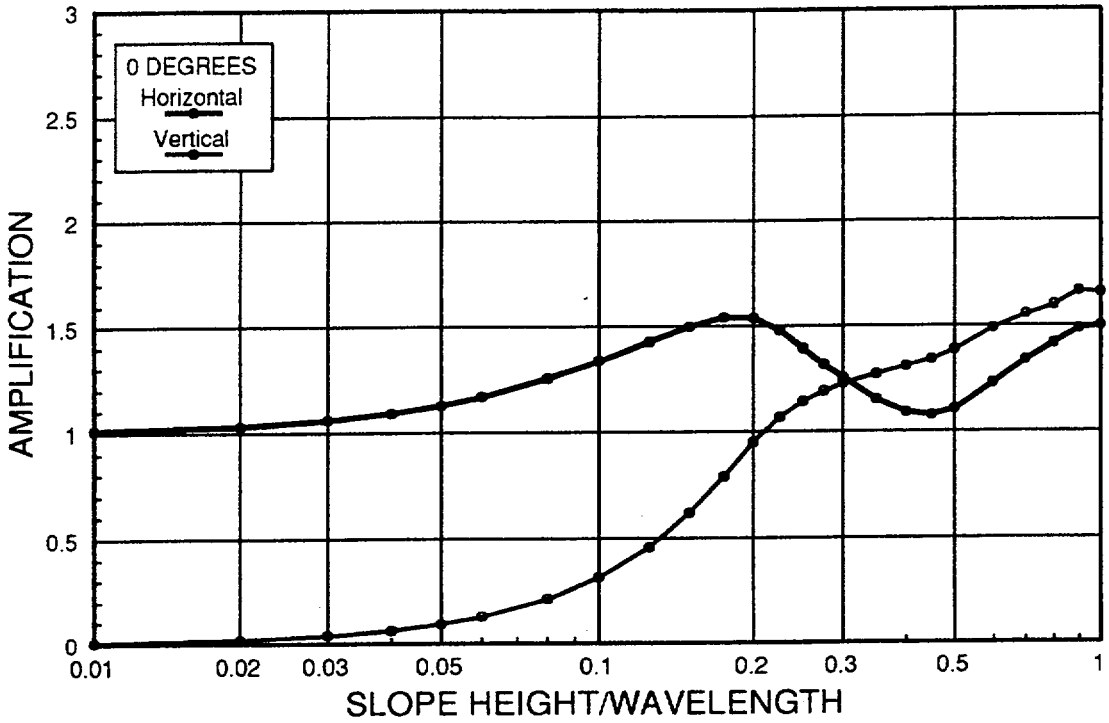

Figure 5.24: Amplifications at the crest for inclined SV-wave incident on a vertical slope, F = 0°, β = 1%.

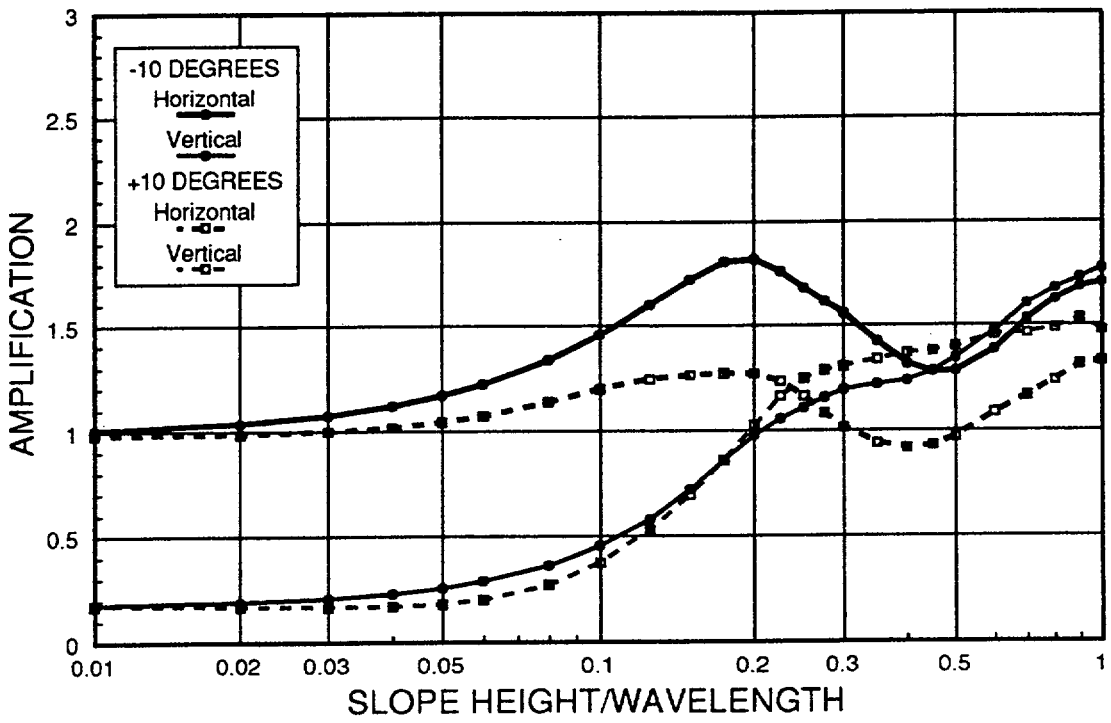

Figure 5.25: Amplifications at the crest for inclined SV-wave incident on a vertical slope, F = -10° and +10°, β = 1%.

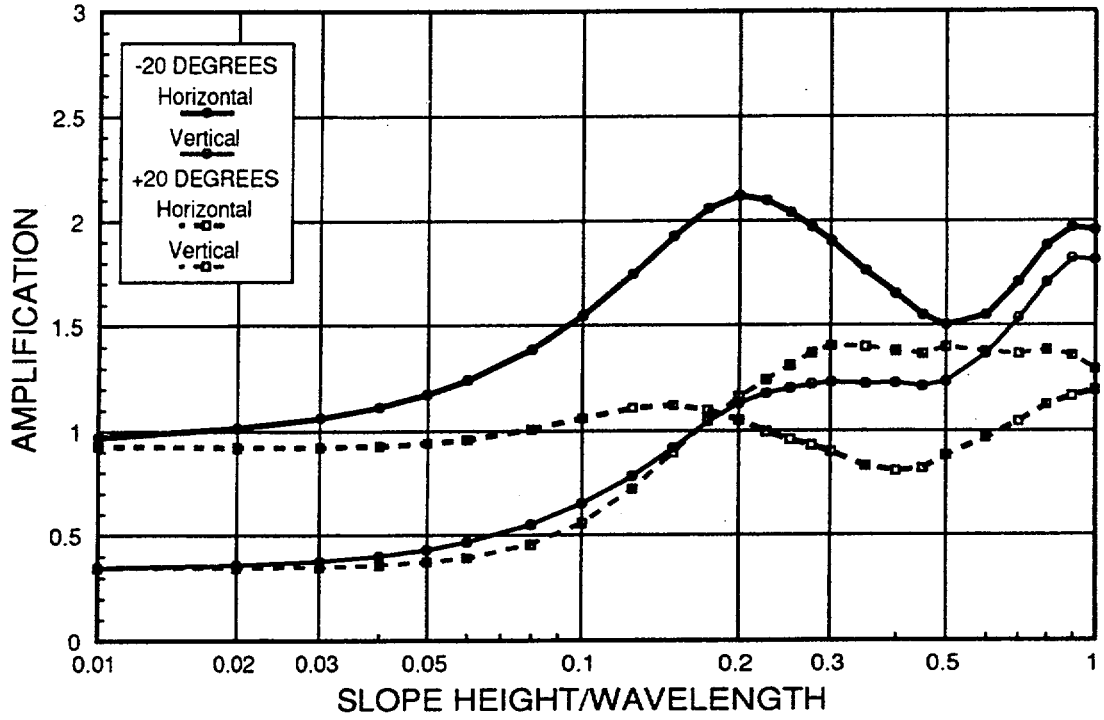

Figure 5.26: Amplifications at the crest for inclined SH-wave incident on a vertical slope, F = -20° and +20°, β = 1%.

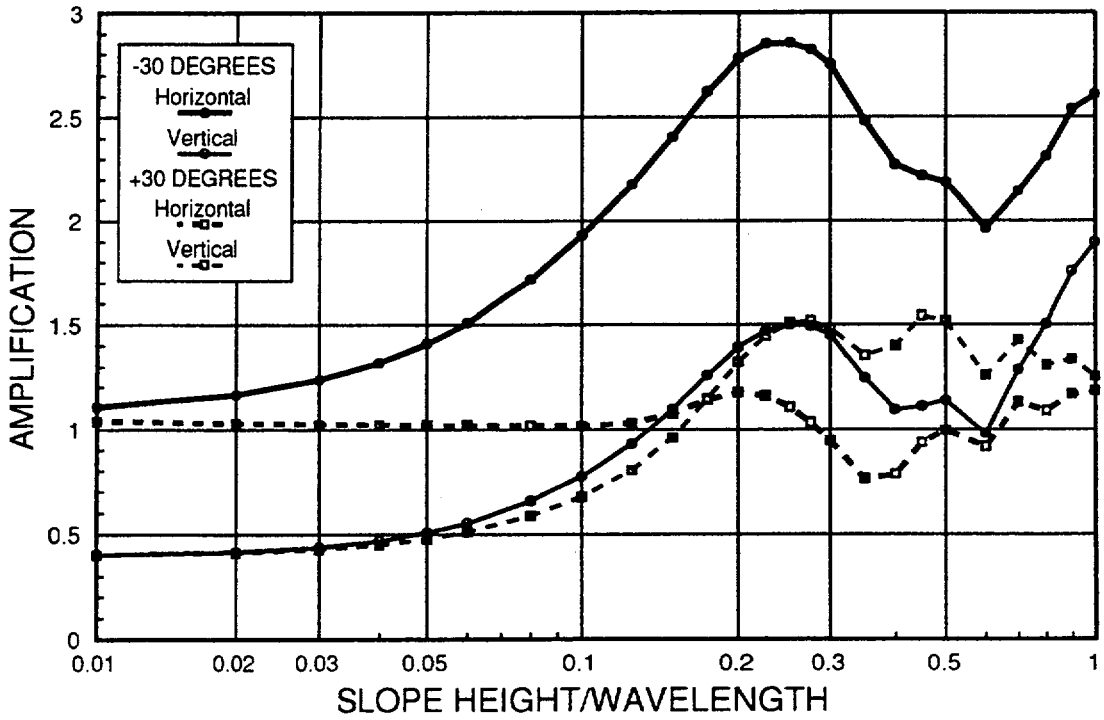

Figure 5.27: Amplifications at the crest for inclined SV-wave incident on a vertical slope, F = -30° and +30°, β = 1%.

Ratio = 0.3, the effect is relatively minor on horizontal motion, but is pronounced on the vertical response for the angles of incidence considered in this study.

Overall, the amplification of inclined SV-waves traveling into the slope may partially explain field observations of failures on slopes facing in a particular direction, while slopes in the same material, but of different orientation, showed no distress. Consequently, these analytical results suggest the need to account for wave orientation in relation to the slope in performing stability analyses.

5.3 ANALYSIS OF A STEPPED LAYER OVER A HALFSPACE

The preceding parametric study of the stepped halfspace provides a fundamental understanding of the topographic effect. The next step is to evaluate the relationship between the natural frequency of the site and the topographic amplification effect. To this end, the analysis of a stepped layer over a halfspace is presented.

A vertically stepped layer over a halfspace was used, as shown in Figure 5.28. The layer has the same material properties as used in the halfspace study discussed previously, while the underlying halfspace has properties as shown in the figure, resulting in an impedance between the layer and the halfspace of 3. The natural frequency of the model behind the crest of the step is varied by changing the thickness of the layer, Z, from H to 5H. The thickness Z is varied because the topographic effect is normalized as a function of H/λ which is dependent on V_S.

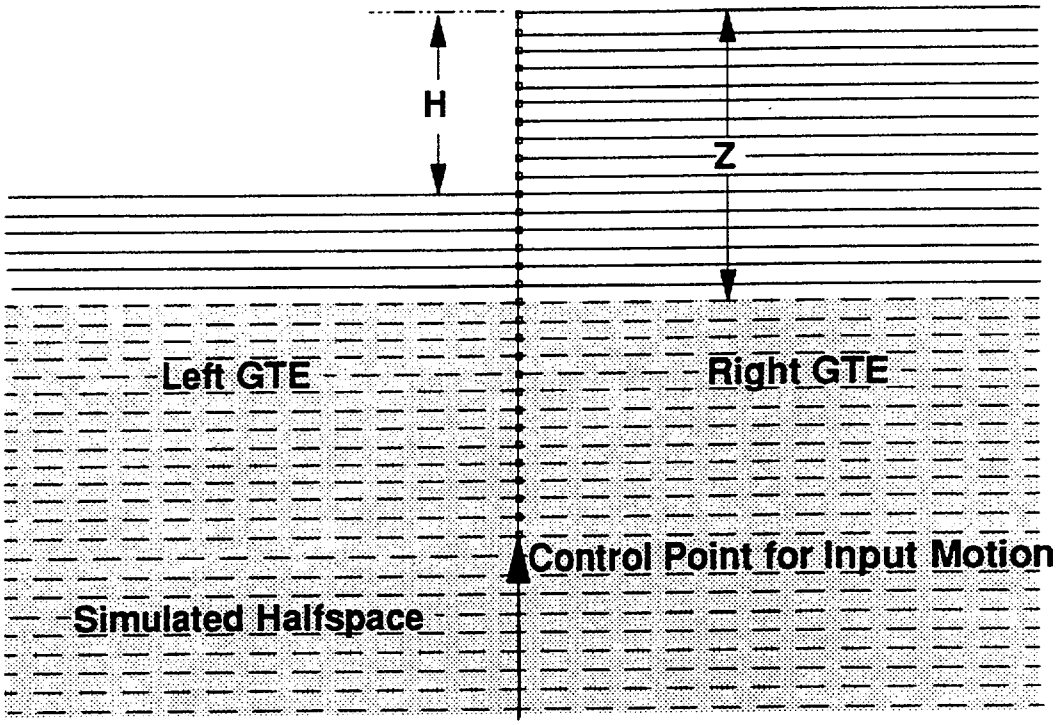

Figure 5.28: Model for vertically stepped layer over a halfspace.

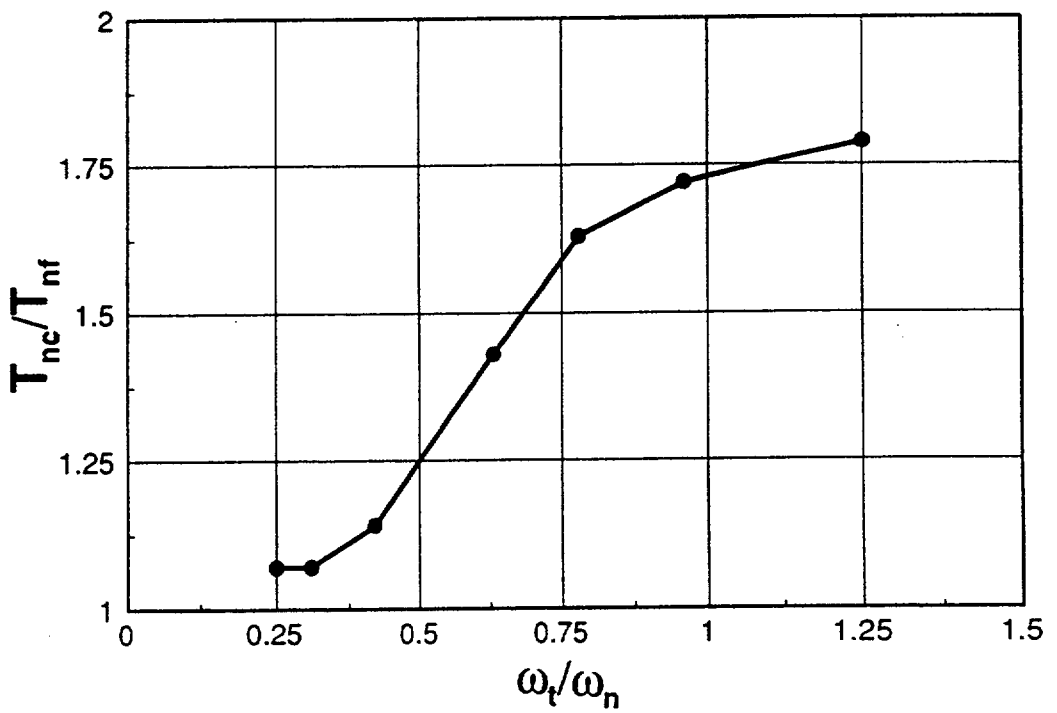

Figure 5.29: Comparison of transfer function ratio, T_{nc}/T_{nf}, as a function of frequency ratio, ω_t/ω_n.

Changing V_S, of the layer, therefore, would not have allowed for the separation of the topographic effect and the resonance at the natural frequency.

The results are presented in Table 5.1 in the form of the horizontal transfer functions for the free field behind the crest and at the crest of the slope. The transfer functions shown are those at the natural frequency of the free field behind the crest, ω_n, defined as

$$\omega_n = \frac{V_s}{4Z} \tag{5.1}$$

and at the topographic frequency, ω_t, defined as

$$\omega_t = \frac{V_s}{5H} \tag{5.2}$$

since the peak effect of topography occurs at about $H/\lambda = 0.2$. A review of the transfer functions for the response at the crest shows that the transfer function at the topographic frequency, T_{tc}, is never greater than the transfer function at the natural frequency of the site, T_{nc}. The results also show that, in the free field, T_{nf} remains relatively constant for all values of ω_n. However, at the crest, T_{nc} increases as ω_n approaches ω_t (i.e. as Z/H approaches 1.00). This trend is clearly shown in Figure 5.29, in which the ratio of the transfer functions, T_{nc}/T_{nf}, is plotted versus the ratio of the frequencies, ω_n/ω_t. At low values of ω_n/ω_t, where slope height is small compared to the wavelength at the natural frequency, the transfer function at the crest, T_{nc}, is approximately equal to the free field transfer function, T_{nf}. However, when the natural frequency of the site occurs near the topographic frequency, the free field motion is amplified by over 50 percent. This amount of amplification is

similar to the amount observed at the topography frequency of the stepped halfspace. It would seem, therefore, that the effects of the natural frequency and those of topography may work independently.

Table 5.1 Transfer Functions for Stepped Layer over Halfspace

Z/H	ω_n	ω_t	CREST		FREE FIELD	
			T_{nc}	T_{tc}	T_{nf}	T_{tf}
1.00	2.0	2.5	5.2	4.3	2.9	2.2
1.30	2.0	1.92	5.0	4.8	2.9	2.8
1.60	2.0	1.56	4.9	3.0	3.0	1.9
2.00	2.0	1.25	4.3	2.6	3.0	1.2
3.00	2.0	0.83	3.3	1.6	2.9	1.2
4.00	2.0	0.62	3.0	2.1	2.8	2.1
5.00	2.0	0.5	3.0	2.3	2.8	1.0

In general, the results of the frequency domain analysis of a stepped layer over a halfspace indicate two important points. First, the natural frequency of the site has a greater effect on surface amplification than does the effect of topography. Second, it appears that the topographic amplification can be added onto the amplification caused by the natural frequency, as is indicated in Figure 5.29. This concept of separating the amplification caused by topography from that caused by the natural frequency is advantageous to the development of a simplified method to estimate topographic effects.

5.4 CONCLUSIONS

The parametric study of the seismic response of a stepped halfspace and a stepped layer over a halfspace shows that the topographic effect of a steep slope on the seismic response of that slope can be normalized as a function of the ratio of the slope height (H) and the wavelength of the motion (λ). Such relationship between slope height and wavelength was also noted by May (1980) for horizontally propagating SH-waves incident on a vertical scarp, and similar relationships were observed between structure dimension and wavelength by others (e.g. Boore, 1972; Geli et al., 1988; Dakoulas, 1993).

For both out-of-plane (SH) waves and in-plane (SV) waves, the magnitude of the response at the crest of the slope is significantly reduced by increased damping, particularly at higher frequencies. However, the amplification of the motion at the crest over that in the free field behind the crest is relatively unaffected by damping. The fact that amplification is relatively unaffected by damping in a homogeneous system was also observed by Boore (1972).

The peak topographic effect occurs at a $H/\lambda \approx 0.2$. This amplification is on the order of 25% for SH-waves, and 50% for SV-waves. The peak at $H/\lambda \approx 0.2$ approximately corresponds to the first mode of vibration of a soil column of thickness H ($H/\lambda = 0.25$), which is the frequency at which Boore (1972) and Geli et al. (1988) observed the peak response in their studies of ridges. Secondary peaks occur near $H/\lambda \approx 0.7$ for SH-waves and $H/\lambda \approx 1.0$ for SV-waves. The vertical component of the topographic effect occurs independently of the natural frequency of the site.

The topographic effect is most apparent for slopes steeper than 60 degrees, and is greater for inclined waves travelling into the slope than away from the slope. For a stepped layer over a halfspace, the natural frequency of the site behind the crest dominates the response, which agrees with observations by Sitar and Clough (1983). If the natural frequency of the site is approximately equal to the topographic frequency, i.e. $\omega_n \approx \omega_t$ then that response is amplified. In no case is the topographic effect greater than the response at the natural frequency.